Analysis and manipulation of atomic and molecular collisions using laser light

Von der

Fakultät für Mathematik und Physik

der

Gottfried Wilhelm Leibniz

Universität Hannover

zur Erlangung des Grades

Doktor der Naturwissenschaften

Dr. rer. nat.

genehmigte Dissertation

von

Dipl.-Phys. André Grimpe

geboren am 27.09.1968 in Stolzenau

2006

Referent: Prof. Dr. Joachim Großer
Coreferent: Prof. Dr. Manfred Kock
Tag der Promotion: 18.07.2006

Abstract

Optical collisions in a crossed beam experiment are examined for the atomic collision pairs LiHe, LiNe, NaNe. Differential cross sections are measured in order to probe the quallity of quantum chemical calculated and spectroscopical determined molecular potentials. The linear polarization of the excitation laser is used to manipulate the contrast of the differential cross sections for NaNe. Using elliptical polarized light total control over the angular position and the contrast of the interference pattern is demonstrated. Differential cross sections for the collision pairs LiH_2 and LiD_2 show a pronounced oscillatory structure, which for the first time is observed for atom-molecule optical collisions.

Key words: optical collisions, molecular potentials, control of atomic collisions

Optische Stöße der atomare Stoßpaare LiHe, LiNe, NaNe werden in einem Experiment mit gekreuzten Teilchenstrahlen untersucht. Differentielle Wirkungsquerschnitte werden gemessen um die Qualität von quantenchemisch berechneten und spetroskopisch bestimmten Molekülpotentialen zu testen. Die lineare Polarisation des Anregungslasers wird dazu benutzt den Kontrast der differentiellen Wirkungsquerschnitte von NaNe zu manipulieren. Die totale Kontrolle über die Winkelposition und den Kontrast der Interferenzstruktur wird durch die Benutzung von elliptisch polarisiertem Laserlicht demonstriert. Differentielle Wirkungsquerschnitte der Stoßpaare LiH_2 and LiD_2 zeigen eine deutliche Oszillationsstruktur, welche das erste Mal für Atom-Molekül Stöße beobachtet wird.

Schlagworte: optische Stöße, Molekülpotentiale, Kontrolle atomarer Stöße

Table of contents

Introduction

The perceptions about the structure and inner nature of matter have changed through the history of philosophy and science. The idea of undestroyable particles called atoms first appeared in Greece in the fifth century B.C. by the philosopher Demokrit. First empirical and theoretical research during the 19th and the beginning of the 20th century by Dalton, Bolzmann, Einstein and Rutherford have confirmed the existence of the atoms and molecules. Over the years the atomic and molecular models have been more and more refined by a wide spread of experimental and theoretical methods. Collisions between atoms, molecules, electrons and ions determine the characteristics of many parts of the environment and experimental physical systems, e.g. chemical reactions, plasmas, like in the outer atmosphere of the earth and of stars, fusion experiments, laser media, combustions and the formation of a Bose Einstein condensate. Since Rutherfords experiment the study and analysis of collisions by scattering experiments is an often used approach to understand the features of atoms and molecules and their interactions. In conventional crossed beams scattering experiments with differential detection the collisional particles are prepared in well known quantum mechanical states and detected state-selective. But the final analysis after the collisional process delivers only indirect information about the collision. The process itself remains uncontrolled and unobserved. The examination of the impact broadening of spectral lines is another widespread used tool to investigate the properties of atomic and molecular interactions. The inherent process of broadening relies on optical transitions during collisions [1, 2, 3]. Accordingly it is possible to intervene directly in the collision process by an optical excitation:

$$A + B + h\nu_e \longrightarrow (AB) + h\nu_e \longrightarrow (AB)^* \longrightarrow \mathrm{A}^* + \mathrm{B} \tag{1}$$
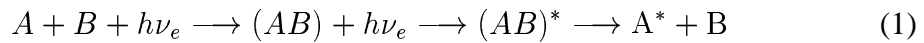
A is a projectile and B a target of an atom-atom or atom-molecule collision. The excitation photon $h\nu_e$ is detuned from the resonance of the free projectile atom. Thus, an optical excitation can only occur during the collision. The described collisions with optical excitation are called optical collisions. Optical collision experiments are done predominantly in gas cells [4, 5, 6, 7] . The results of the measurements just refer to a statistic ensemble of the collision particles. The signal is averaged over the scattering angles and the whole distribution of collision energies. The averaging again yields on-

ly indirect information about the collision process.

The presented experiments are a combination of both methods. Optical collisions are investigated in a crossed beams experiment with a differential detection scheme. This creates the possibility to observe and manipulate collisional particles in prepared quantum states by optical transitions. The first successful experimental realization was reached in 1994 [8]. The following intensive studies of Na-rare gas and Na-molecule optical collisions lead to new perceptions about the collision processes [9, 10, 11, 12]. The enhancement to other collisional systems like KAr and CaAr was very fertile [13, 14].

Differential cross section of atom-atom optical collisions have a oscillatory structure. These Stueckelberg oscillations [15] result from a coherent superposition of quantum-mechanical undistinguishable pathways. The analysis and comparison of experimental and theoretical determined differential cross sections opens the chance to probe and improve interatomic potentials [13]. The knowledge of molecular potentials is crucial for many applications. The accuracy of quantum chemical determined potentials is in the range of 10 cm^{-1} to 100 cm^{-1}. Spectroscopic examinations [16, 17] allow to determine attractive parts of potential curves with a uncertainty up to 0.03 cm^{-1} but are relatively insensitive for repulsive curves.

The optical collisions of the following collisional systems:

$$\mathrm{Li(2s)} + \mathrm{X} + \mathrm{h}\nu_\mathrm{e} \quad \longrightarrow \quad \mathrm{Li(2p)} + \mathrm{X}$$

$$\mathrm{Na(3s)} + \mathrm{Ne} + \mathrm{h}\nu_\mathrm{e} \quad \longrightarrow \quad \mathrm{Na(3p)} + \mathrm{Ne}$$

(2)
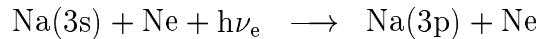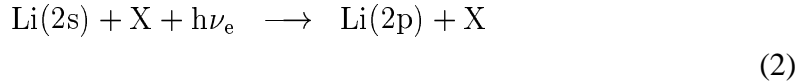
with X = Ne, He, H$_2$, D$_2$ are studied in this work.

By comparing experimental and theoretical determined differential cross sections of LiHe and LiNe the accuracies of calculated theoretical potentials by Staemmler [18], Czuchaj [19] (both LiHe) and Kerner [20] (LiNe) are probed.

The differential cross sections of atom-molecule collisions usually show no oscillations. The thermal molecules are in a widespread variety of vibrational and rotational states. This averages out the oscillatory structure. Differential cross sections of LiH$_2$ and LiD$_2$ are measured and compared with theoretical determined ones. The idea is to use H$_2$ and D$_2$ as molecular targets hoping that because of their huge rotational quantums the main fraction of both is in their rotational ground state causing a visible oscillatory structure of their differential cross section.

The attractive part of an ab intio calculated theoretical A$^2\Pi$ potential [20] is probed for the NaNe system using negative detuned excitation light with various polarizations. The results are compared with a spectroscopical determined potential [21].

The oscillatory structure of differential cross sections of optical collisions depend on the polarization of the excitation laser. The control of atomic and molecular processes by laser light is an active field of research. Experiments concerning coherent control [22, 23] highlight the importance of the relative phase of the spectral components. The control of chemical processes with complex molecules by pulse shaping techniques

with one in respect to the phase and amplitude by learning algorithm [24] optimized electric field is impressively demonstrated [25, 26]. Control schemes involving collisions in caging reactions [27, 28], ultracold gases [29, 30], and bimolecular processes [31, 32, 33] show the high potential of the method. Laser polarization as control tool [34] for physical processes is gaining increased attention [25, 35]. Recent experiments [36, 34] have demonstrated the possibility to manipulate and observe the collisional complex using laser light. In this work this is extended to the total control over the amplitude and phases of the interfering waves. The experiments are done for NaNe collision pairs using positive detuned elliptical polarized excitation light.

Chapter 1

Theoretical introduction

1.1 Differential cross sections

1.1.1 Potentials and optical transitions

Molecular interaction potentials are important to understand atomic and molecular collision processes and chemical reactions in all energy regimes. They can be determined by spectroscopic techniques and ab initio calculations. The time-independent Schrödinger equation of electrons moving in the field of nuclei is solved for fixed internuclear distances r (Born-Oppenheimer approximation [37, 38]). All electrostatic interactions are taken into account. The spin is disregarded. The computed potentials energies $V_i(r)$ for each electronic state depend on r. At infinite internuclear distances the potential energies are the sum of the eigenenergies of the unperturbed collision partners. An example for the LiNe potential energy curves is shown in figure 1.1. The numerical calculation of potentials using additional approximations is very elaborate. The accuracy of the potentials depend on the internuclear distance (repulsive part, well, asymptotic region) and the method which is used. The LiNe and NaNe potentials were calculated with a CPP (core polarization potential) approach reaching an accuracy of $10\,\mathrm{cm}^{-1}$ in the relevant region (see [20]). Different CEPA (coupled electronic-pair approximation) methods were applied for LiHe [18] (CEPA-2CI [4]) and (CEPA-0 [39]) for LiH_2 [40], their accuracy is between 15 and $50\,\mathrm{cm}^{-1}$. The potentials are shown in figures 3.5, 3.10 and 3.13.

In order to describe potentials in the presence of light fields the dressed collision pair approach is used [41, 42] . Without light matter interaction the photon energy hν sums up with the potential energy $V_g(r)$ of the $X^2\Sigma_{1/2}$ ground state. The resulting energy curve intersects with the curve $V_e(r)$ of one of the excited states (see figure 1.2). The internuclear distance r_c where the intersection is placed, is called Condon radius r_c. The resonance condition
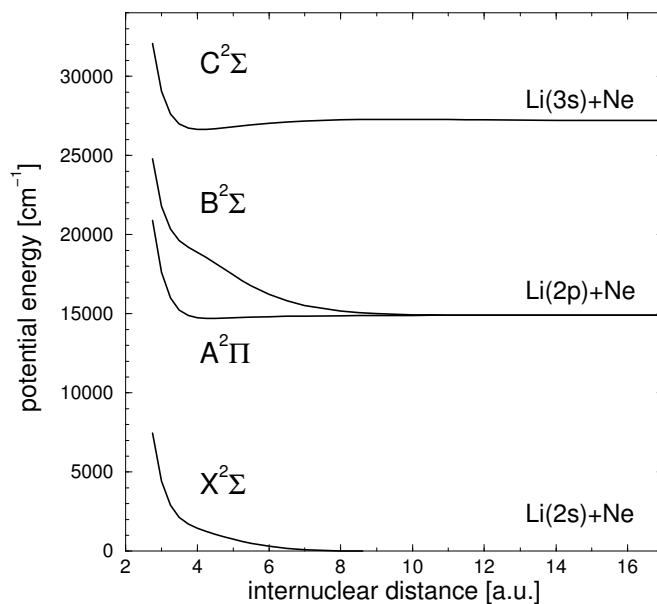
Figure 1.1: *LiNe molecular potentials [20]: The potential energy curve of the $X^2\Sigma$ ground state with the potential curves of the first three excited $A^2\Pi$, $B^2\Sigma$ and $C^2\Sigma$ states.*

Figure 1.2: *Dressed states approach: The LiNe potential energy curve of the $X^2\Sigma$ ground state shifted by the energy of the exciting photon and of the $B^2\Sigma$ state. The energy of the asymptote of the shifted $X^2\Sigma$ state curve is defined as zero. In the case of using resonant photons the asymptote of both states would have the same value. The place of intersection is marked as the Condon radius r_c.*

12

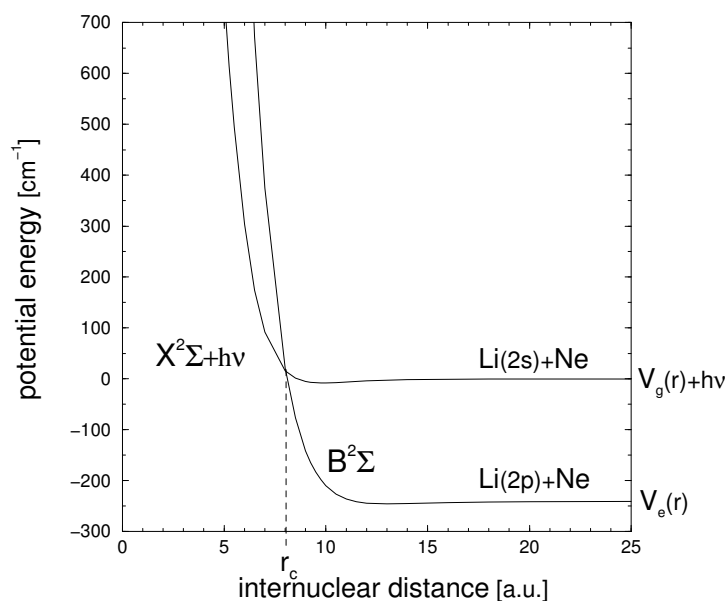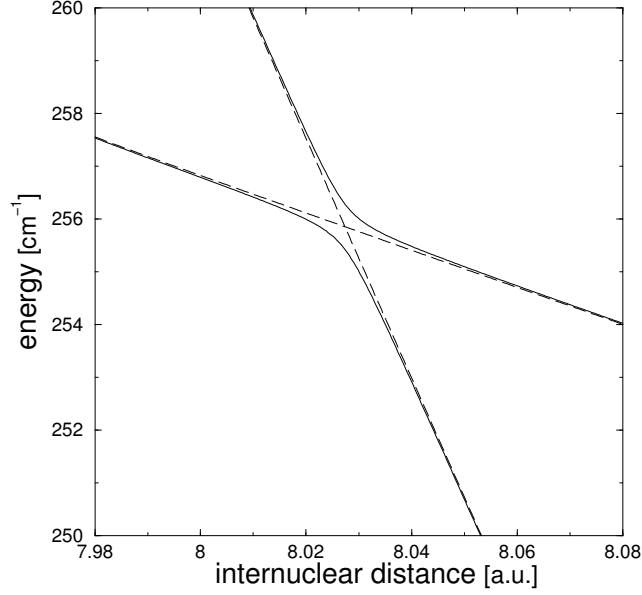Figure 1.3: *The LiNe potential energy curves of the shifted $X^2\Sigma$ ground state and the $B^2\Sigma$ state modified by light. Dashed lines: without light matter interaction (enlarged figure 1.2) solid lines: light matter interaction included.*

$$V_g(r_c) + h\nu = V_e(r_c) \tag{1.1}$$

is fulfilled [43]. The optical transitions are localized at the Condon radius. The difference of the photon energy hν and the energy of the free alkali(s) to alkali(p) transition is denoted as detuning. By changing the detuning it is possible to vary the Condon radius. If light matter interaction is included, the potential curves are disturbed and undergo a modification in presence of the light field. The crossing becomes an avoided crossing and transitions could happen in the whole crossing region. For the applied experimental conditions (chapter 2), especially low laser intensities, the size of this region is in the order of 0.03 a.u. (figure 1.3) and the change of the potential energies less than 0.5 cm^{-1}. Therefore it can be assumed, that the optical transitions are well localized and that the potential curves are uneffected by the interaction with the light field.

The optical transition probability p from one electronic state $\mid \psi_g \rangle$ to another $\mid \psi_e \rangle$ can be calculated using the Landau-Zehner model [44]. For a sudden (diabatic) approach of the colliding particles, the system will remain in its initial state $\mid \psi_g \rangle$ after passing the crossing region. The transition probability p$_{dia}$ reads:

$$\mathrm{p_{dia}} = 1 - \mathrm{e}^{-\pi\gamma} \tag{1.2}$$

13

with the Massey parameter

$$\gamma = \frac{2\,\pi\,\hbar\,\Omega^2}{v\,|\Delta V'|}$$

Ω : Rabi frequency $\Omega = \frac{1}{\hbar}\mathbf{E}\cdot\mathbf{d}$

$\mathbf{E}$: electric field vector of the exciting light

$\mathbf{d}$: transition dipole moment $\mathbf{d} = \langle\psi_e\mid e\cdot\sum_j \mathbf{r}_j\mid\psi_g\rangle$

ψ_e, ψ_g: electronic wave functions of the transition,

$\mathbf{r}_j$: position vectors of the electrons and

e: charge of the electron

$v(r_c)$: radial component of the relative velocity at r_c

$\Delta V'$: slope of the difference of the two potentials at r_c

$$\Delta V'(r_c) = \frac{d(V_e(r_c) - V_g(r_c)))}{dr}$$

In the adiabatic case the particles encounter slowly leading to a change of the electronic state of the collisional system. $p_{adia} = 1 - p_{dia}$ is the resulting transition probability. The crossing region is passed twice. The total probability to change from state $\mid\psi_g\rangle$ to $\mid\psi_e\rangle$ is

$$p = p_{\mathrm{dia}}(1 - p_{\mathrm{dia}}) \ . \tag{1.3}$$

For low light intensities is $\gamma \ll 1$. The equation 1.2 can be expanded to:

$$p = \frac{2\,\pi\,\hbar\,\Omega^2}{v(r_c)\,|\Delta V'|} \ . \tag{1.4}$$

The transition probability depends on the electric field:

$$p \sim (\mathbf{E}\cdot\mathbf{d})^2 \ . \tag{1.5}$$

$\mathbf{d}$ is parallel to the internuclear axis for a $\Sigma - \Sigma$ transition and perpendicular for a $\Sigma - \Pi$ transition [45]. It has to keep in mind that not only the amplitude of $\mathbf{E}$ has an influence, it is also possible to change the transition probability and to manipulate the collisional system by varying the polarization.

1.1.2 Calculation of cross sections

In order to compare experimental results with the theory it is necessary to calculate the differential cross sections from the molecular interaction potentials. A detailed representation of the calculation procedure is described in [46]. The form of the Schrödinger equation is a set of coupled-channel equations. The number of electronic basis states underlying the numerical determination is limited. Only the ground state and the relevant excited states are used as a basis for the calculation. Higher excited states are
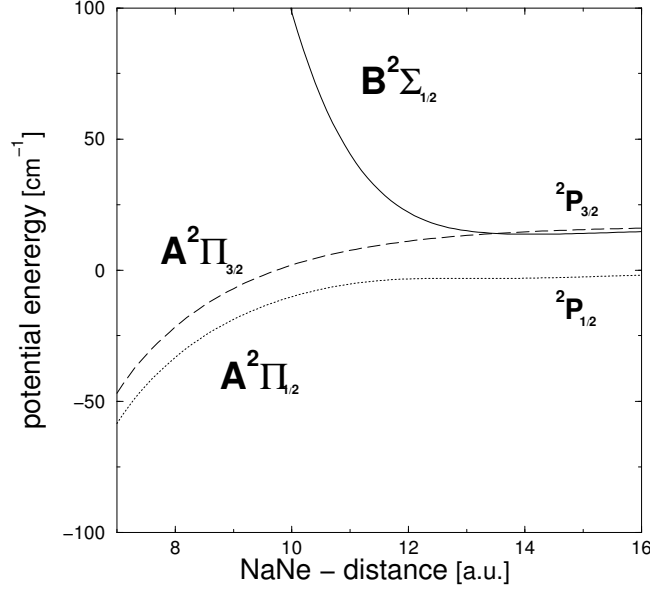
Figure 1.4: *The NaNe potential energy curves of the two $A^2\Pi_{1/2,3/2}$ states and the $B^2\Sigma_{1/2}$ state.*

disregarded. The differential cross sections are computed by partial wave summation. The hyperfine structure is neglected. All calculations are done in the limit of zero laser intensity. The low light intensity causes a non zero γ which introduce an additional phase 2γ [47] leading to a shift in the interference pattern of the differential cross section of less than $0.1°$ for the present experimental conditions [12, 48]. The spin-orbit interaction is assumed to be independent of the internuclear distance and contributes to the Hamilton operator. Nonadiabatic couplings because of spin-orbit and rotational interactions are taken into account completely. The coupling between the $B^2\Sigma_{1/2}$ state and the two $A^2\Pi_{1/2,3/2}$ states leads to a population of both alkali fine structure states $^2P_{1/2}$ and $^2P_{3/2}$ [11] (figure: 1.4). The conclusion is that the results of the calculations can be assumed as exact for precisely known potentials.

1.1.3   Convolution

The experimental differential cross section σ_{exp} for a fixed detuning is measured in dependency of the scattering angle in the laboratory-frame θ_{lab}, the electric field vector $\mathbf{E}$ and the velocity of the projectile beam after the collision v_{ac}:

$$\sigma_{\mathrm{exp}} = \sigma_{\mathrm{exp}}(\theta_{\mathrm{lab}}, \mathbf{E}, \mathrm{v}_{\mathrm{ac}}). \tag{1.6}$$

The calculated differential cross section σ_{th} in the center-of-mass frame is:

$$\sigma_{\mathrm{th}} = \sigma_{\mathrm{th}}(\theta_{\mathrm{cm}}, \alpha_{\mathrm{pol}}^{\mathrm{cm}}, \mathrm{W_k}) \tag{1.7}$$

15

where W_k is the relative energy before the collision, θ_{cm} the scattering angle in the center-of-mass system and α_{pol}^{cm} the angle between the polarization of the excitation laser and the relative velocity before the collision. In order to compare σ_{exp} with σ_{th} it is necessary to convert the theoretical data from the center-of-mass-frame to the laboratory-frame coordinates. The relevant factors influencing the finite experimental resolution are: the detuning, the polarization, the scattering angle, the particle masses, the times-of-flight of the ions in the detector, geometrical distances, the velocity distributions of the particle beams before the collision, the number and width of the alkali velocity classes after the collision, the particle density distributions in the scattering volume, the size of the scattering volume and the dimension of the aperture of the detector. They have to be taken into account to calculate an apparatus function f_{app}. The appropriate experimental error margins are quoted in table 2.10. f_{app} is calculated for one θ_{lab}, a fixed electric field vector $\mathbf{E}$ and a given detuning W_{det}:

$$f_{app} = f_{app}(\theta_{lab}, \mathbf{E}, v_{ac}, W_k, \theta_{cm}, \alpha_{pol}^{cm}) \tag{1.8}$$

The expected intensity I of the signal is calculated by a procedure similar to a convolution. It is determined by a numerical integration over the product of the theoretical differential cross section and the apparatus function:

$$I(\theta_{lab}, \mathbf{E}, v_{ac}) = \int (f_{app} \cdot \sigma_{th}) \; dW_k \; d\theta_{cm} \; d\alpha_{pol}^{cm} \tag{1.9}$$

For a more detailed insight into the specific calculations and how the experimental resolutions are implemented see [49, 50].

1.2 Semiclassical description

1.2.1 Semiclassical picture

The quantum mechanical approach describes the optical collisions quantitatively accurate. However, the deviations between the quantum mechanical picture and a semiclassical description using classical trajectories, localized transitions and interference are small enough to justify the usage of the semiclassical description to get a more intuitive comprehension and to make qualitative predictions of the process [51]. An example of differential cross sections for NaKr calculated with both pictures is shown in figure 1.5.

Figure 1.6 is a geometric illustration of a atom-atom collision in the center of mass system. The vector $\mathbf{r}$ is pointing from the target atom to the projectile particle. It undergoes a rapid rotation during the collision. The trajectory $\mathbf{r}(t)$ of the projectile particle in the potential V(r) is described in the polar coordinates r(t) and ϕ(t). b is the impact parameter, χ the deflection angle and $\mathbf{v}$, $\mathbf{v}'$ are the relative velocity vectors before and after the collision. The energy E and the orientation of the angular momentum in
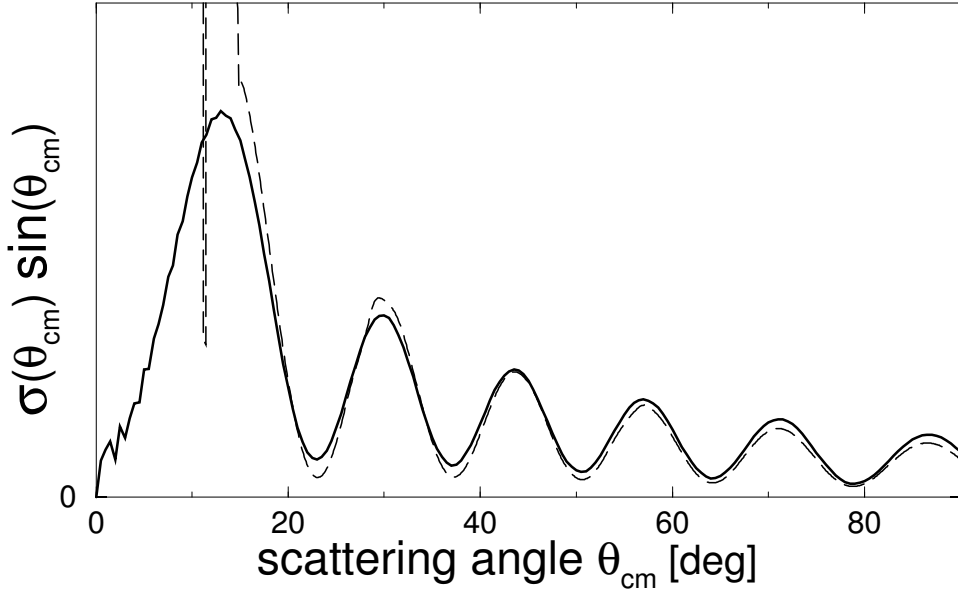
Figure 1.5: *Differential cross sections: quantum mechanical (black line) + semiclassical (dashed line). NaKr, detuning: 137 cm⁻¹, W_{kin}: 100 meV, fixed polarization [50]. The qualitative and the quantitative deviations are slight for scattering angles bigger than 20°. At small scattering angles the deviation gets large and the semiclassical cross section disappears.*

respect to the scattering plane is conserved for atom-atom collisions [47]. The relevant potentials for an optical collision are the potential curves of the $V_g + h\nu$ and V_e states. V(r) is constructed taken into account the changeover between both states at the Condon radius during the incoming ($\dot{r} > 0$) or the outgoing ($\dot{r} < 0$) part of the collision. The influence of two different potentials V_1 and V_2 (figure 1.7) leads to two different trajectories. The equation for the classical deflection function is derived from the equations of motion:

$$\chi(\mathrm{v}, \mathrm{b}) = \pi - \int_{\mathrm{r_0}}^{\mathrm{R}} \frac{\mathrm{b}}{\mathrm{r^2}} \left(\frac{1}{\sqrt{1 - \frac{\mathrm{V_{app}(r)}}{\mathrm{E}} - \frac{\mathrm{b^2}}{\mathrm{r^2}}}} + \frac{1}{\sqrt{1 - \frac{\mathrm{V_{div}(r)}}{\mathrm{E}} - \frac{\mathrm{b^2}}{\mathrm{r^2}}}} \right) \mathrm{dr}, \qquad (1.10)$$

with the initial collision energy $\mathrm{E} = \frac{1}{2}\mathrm{mv^2}$, where v is the absolute value of the initial relative velocity and m the reduced mass of the collisional particles. $V_{app}(r)$ is the potential for the approaching and $V_{div}(r)$ for the diverging particles. The deflection function allows to determine the deflection angle of the projectile for different impact parameters and a given collision energy. In the experiment only the absolute value of the deflection angle labeled as the scattering angle θ ($\theta = |(\chi + \pi)mod(2\pi) - \pi|$) is detectable. The deflection functions have to be calculated for both potentials V_1 and V_2. Figure 1.8 shows an example of a deflection function for V_2. The minimal value of χ is denoted as θ_r, with the appropriate impact parameter b_r. In figure 1.5 it can be
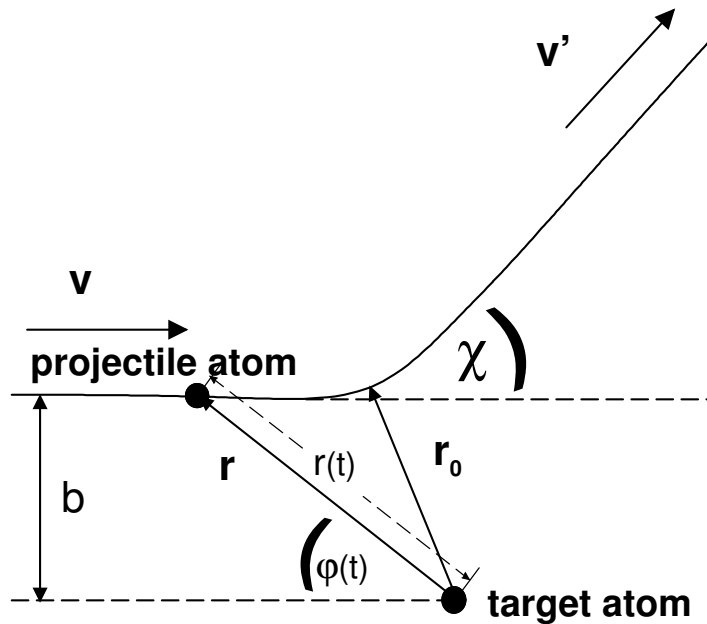
Figure 1.6: *A classical trajectory $r(t)$: $r(t)$ and $\varphi(t)$ are the coordinates. b is the impact parameter, χ the deflection angle and r_0 the classical turning point. v and v' are the relative velocities before and after the collision.*
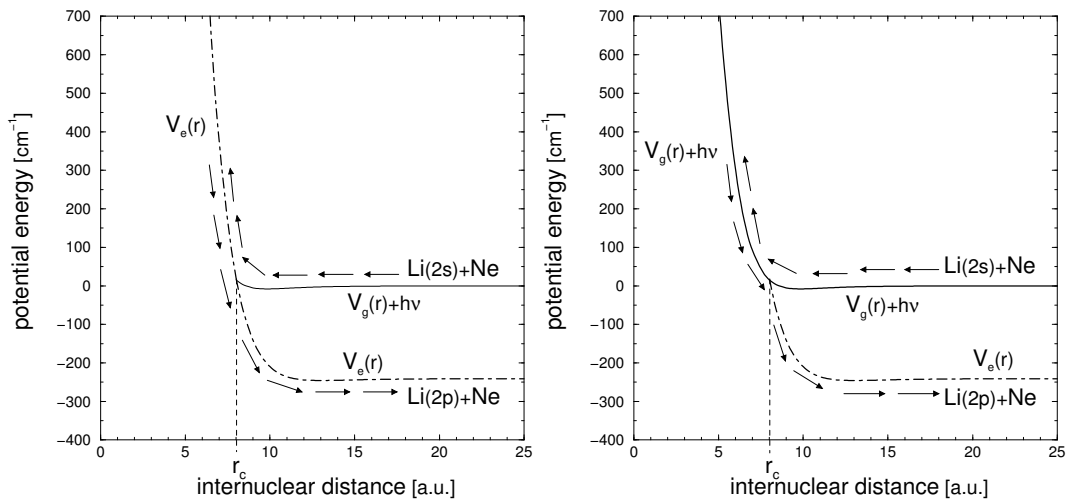
Figure 1.7: *Potentials V_1 and V_2 for LiNe including the energy of the excitation photon. Left side V_1: The approaching particles follow the $V_g + h\nu$ potential curve, are excited during the first passage of r_c, reach the classical turning point and diverge under the influence of the V_e potential curve. Right side V_2: The particles converge, reach the classical turning point and separate influenced by the $V_g + h\nu$ potential curve, while the second passage of r_c the excitation occurs and the particles follow the V_e potential curve.*

18

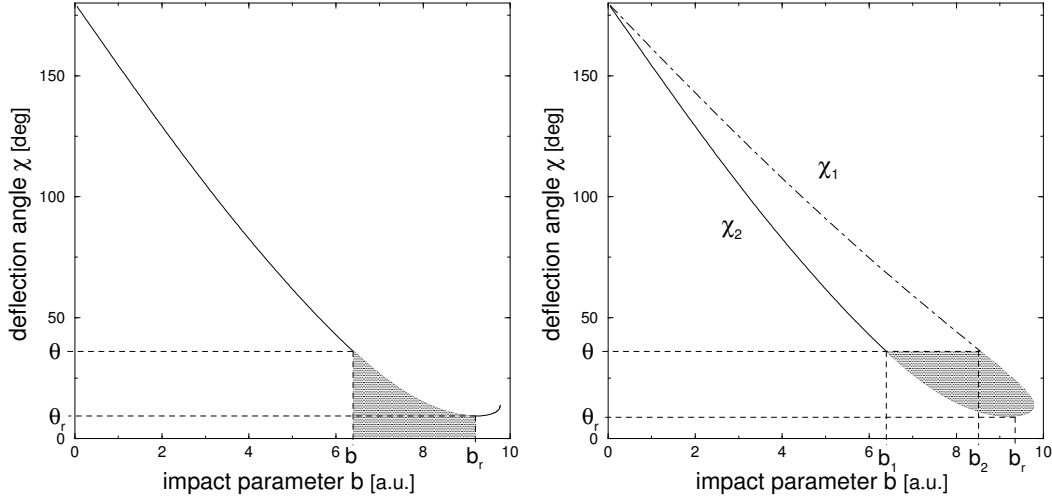Figure 1.8: *Deflection functions and phases. NaNe positive detuning. Left side: deflection function $\chi_2(v,b)$ for an optical transition in the outgoing part of the collision. Disregarding the constant addends of equation 1.12 the shaded area is proportional to the phase of the corresponding trajectory. Right side: deflection functions $\chi_1(v,b)$ (dot-dashed) and $\chi_2(v,b)$ (solid) for both possibilities of excitation. The shaded area is proportional to the phase difference $\Delta\phi$.*

seen that there is no classical signal for small deflection angles. The largest possible classical impact parameter of an optical collision equals the Condon radius. In the region of $b > r_c$ and $\theta < \theta_r$ the boundaries of the semiclassical model are reached.

The semiclassical phase of a trajectory after the collision can be calculated as an integral over the wavenumber $k(\mathbf{r}) = \frac{m\dot{r}}{\hbar}$:

$$\phi(\mathbf{r}) = \int_R^r k(\mathbf{r})ds \tag{1.11}$$

elementary transformations which are described in detail in [49] lead to the following expression:

$$\phi(v, b) = -k \int_b^{b_r} \chi(b')db' - kb\chi + C' \tag{1.12}$$

The phase is proportional to the shaded area in the left graph of figure 1.8 disregarding the constant addends $kb\chi + C$. In the right graph the deflection functions $\chi_1(v,b)$ and $\chi_2(v,b)$ for both possibilities of excitation are shown. For a given scattering angle trajectories belonging to two impact parameters cause two different phase contributions. In order to include interference of the undistinguishable pathways, the resulting phase difference $\Delta\phi$ of the different trajectories has to be introduced:

$$\Delta\phi(\theta) = k \int_\theta^{\theta_r} (b_1(\theta') - b_2(\theta')) \, d\theta'. \tag{1.13}$$
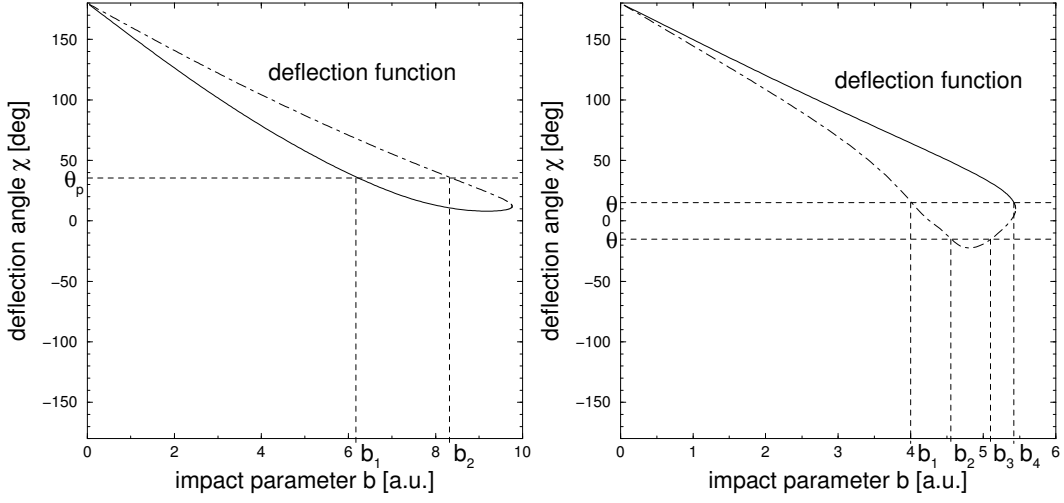
19

Figure 1.9: *Deflection functions $\chi_1(v,b)$ (dot-dashed) and $\chi_2(v,b)$ (solid) for NaNe collision pairs. Left side: positive detuning of 120 cm^{-1}, relative energy E = 717.4 cm^{-1}, scattering angle $\theta_p = 35.5°$. Right side negative detuning of -299.7 cm^{-1}, relative energy E = 746.1 cm^{-1}, scattering angle $\theta_n = 15.1°$.*

$b_1(\theta)$ and $b_2(\theta)$ are the two impact parameters. The phase difference is proportional to the shaded area in the right part of figure 1.8. Its variation with the scattering angle is responsible for the interference structure in the differential cross section (figure 1.5). Deflection functions of NaNe for positive (left) and negative detuning (right) are shown in figure 1.9. The two possible impact parameters for positive detuning and a fixed deflection angle lead to two trajectories. Negative detuning allows the excitation of the $A^2\Pi$ state. The appropriate potential has an attractive part which can cause negative values of χ. Up to four impact parameters b_1 - b_4 with the resulting trajectories are possible. In figure 1.10 the classical geometries of the optical collisions corresponding to the marked scattering angles θ_p and θ_n of figure 1.9 (left side: positive detuning; right side: negative detuning) are illustrated. The curves are the trajectories of the alkali atom viewed by the target particle. The large circle has the radius r_c. $\mathbf{r}_i$ are denoted as the Condon vectors. They are pointing from the target atom to the projectile particle in the moment of excitation. For positive detuning the two trajectories bend away from the target, because the $B^2\Sigma$ state is excited, the particles basically feel repulsive forces. In the case of negative detuning (right) there are up to four Condon vectors. Two of the trajectories are also mainly repulsive. The other two trajectories are mainly attractive and bend towards the target. Strongly attractive trajectories as shown in this graph only occur at adequately low relative velocity. For high relative velocity simply two repulsive trajectories remain. The different pathways contribute different to the signal. The appropriate relative weights are indicated by the diameters of the small circles. The vector $\mathbf{E}$ denotes the amplitude of the electric field vector in the collision plane.
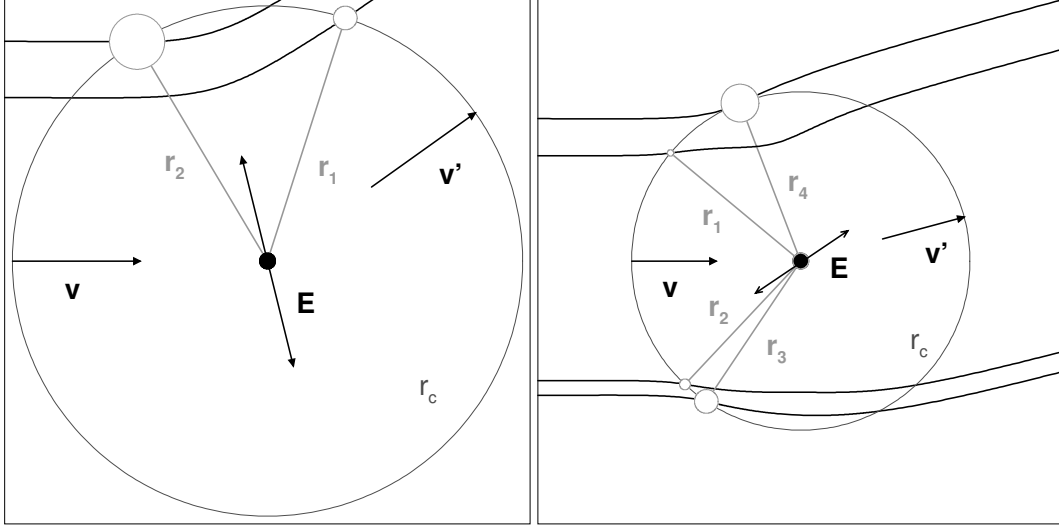
Figure 1.10: *Optical excitation during an atom-atom collision. The dark curves are the trajectories for the relative motion of the two atoms. **v** and **v'** are the relative velocity vectors before and after the collision. The $\mathbf{r}_j$ are the Condon vectors. The centers of the small circles on the trajectories denote the transition points where the photon is absorbed, their sizes indicate the relative weights of the signal contributions. **E** denotes the amplitude of the electric field vector. The size of the diagrammed area in both graphs is 20 a.u. × 20 a.u.. The experimental conditions are as in figure 1.9 (left side: positive detuning, $\Sigma - \Sigma$ transition; right side: negative detuning, $\Sigma - \Pi$ transition).*

The semiclassical expression for the differential cross section is

$$\frac{\mathrm{d}\sigma}{\mathrm{d}\Omega} = \frac{1}{\sin(\chi)} \left| \sum_{j} \sqrt{\frac{\mathrm{p_j} \cdot \mathrm{b_j}}{|\mathrm{d}\chi/\mathrm{db_j}|}} \cdot \mathrm{e}^{\mathrm{i}\phi_j} \right|^2 .$$ (1.14)

The summation is done over all contributions of the different trajectories to one scattering angle θ_{CM} in the center of mass system. The $\mathrm{b_j}$ are the impact parameters and ϕ_j is the collision induced scattering phase. The p_j are the transition probabilities described in equation 1.4. Singularities, where the semiclassical value goes to infinity are denoted as rainbow or glory structures. Rainbow structures appear e.g. as described before at the smallest possible deflection angle θ_r ($\mathrm{d}\chi/\mathrm{db}_j = 0$). In the case of attractive potentials and χ equaling zero glory structures can be observed.

1.2.2 Polarization dependence

The transition probability p_j is proportional to the scalar product of the electric field **E** and the transition dipole moment **d** ($\mathrm{p} \sim (\mathbf{E} \cdot \mathbf{d})^2$ as described in equation 1.5. The
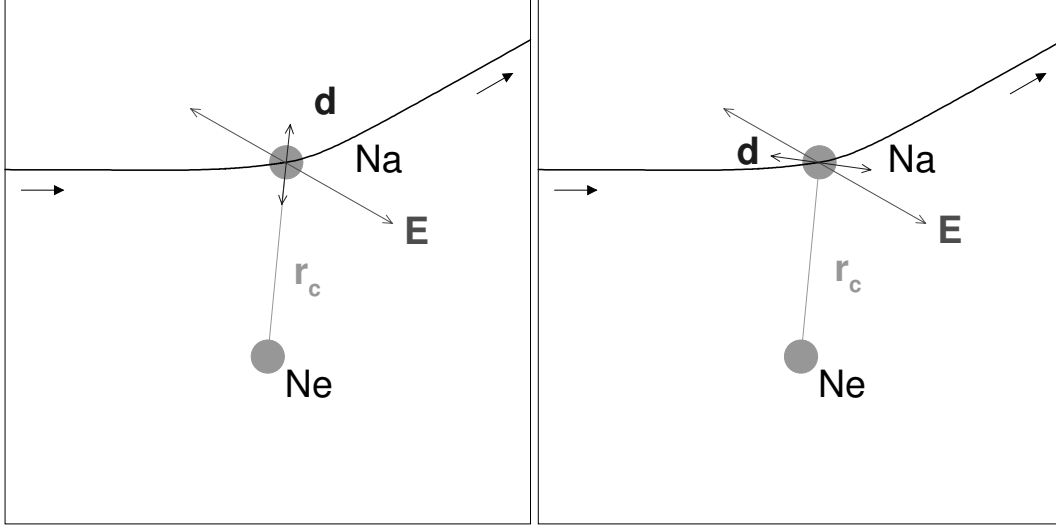
Figure 1.11: *Direction of the transition dipole moment **d**. One classical trajectory + Condon vector. Left figure: positive detuning, $\Sigma - \Sigma$ transition, **d** $\parallel$ **r**$_c$. Right figure: negative detuning, $\Sigma - \Pi$ transition, **d** $\perp$ **r**$_c$.*

semiclassical differential cross section of equation 1.14 can be written as:

$$\sigma(\theta_{\mathrm{cm}}) \sim \left| \sum_j \mathrm{q_j} \; \mathbf{d_j} \cdot \mathbf{E} \; \exp(\mathrm{i}\phi_j) \right|^2 , \qquad (1.15)$$

with the phases ϕ_j of the separate trajectories, the relative weights of the signal contributions q_j

$$\mathrm{q_j} = \sqrt{\frac{2\pi \mathrm{b_j}}{|\mathrm{d}\chi/\mathrm{db_j}| \, \hbar \mathrm{v} \, |\Delta \mathrm{V'}|}} \qquad (1.16)$$

and the transition dipole moments $\mathbf{d}_j$. Equation 1.15 holds for linear as well as elliptic polarization. The contribution of each trajectory can be switched off by varying the linear polarization of the electric field in such a way that the scalar product $\mathbf{d}_j \cdot \mathbf{E}$ vanishes. Due to the fact that for positive detuning $\mathbf{d}_j$ is parallel to $\mathbf{r}_j$, the interference structure vanishes if $\mathbf{E}$ is perpendicular to one of the $\mathbf{r}_j$. The maximal values of σ are expected for a $\mathbf{E}$ positioned in between the two Condon vectors (left graph of figure 1.10). For negative detuning $\mathbf{d}_j$ is perpendicular to $\mathbf{r}_j$, the contribution of one trajectory is deactivated, if one of the $\mathbf{r}_j$ is parallel to $\mathbf{E}$. The polarization of $\mathbf{E}$ which lead to maximal signal in this case depends on up to four relative weights, an instance is denoted in the right graph of figure 1.10. The described theory refers to the possibility to use the polarization of the exciting light as a tool to investigate and manipulate atomic collisions.

For two trajectories and a $\Sigma - \Sigma$ transition ($\mathbf{d}_j \parallel \mathbf{r}_j$) equation 1.15 can be converted:

$$\sigma(\theta_{\mathrm{cm}}) \sim |\mathbf{r}_1 \cdot \mathbf{E} + \mathrm{q} \; \mathbf{r}_2 \cdot \mathbf{E} \; \exp(\mathrm{i}\Delta\Phi)|^2 \quad \text{with:} \quad \mathrm{q} = \frac{\mathrm{q_2}}{\mathrm{q_1}} \qquad (1.17)$$

$\Delta\Phi$ is the phase difference and q the relative weight. In general the electric field vector **E** is complex:

$$\mathbf{E(t)} = \mathbf{E} \, \exp(\mathrm{i}\omega\mathrm{t}) \tag{1.18}$$

ω is the radial frequency of the exciting light. This shape of **E** is realized for elliptical polarized light. The amplitude vector **E** of the electric field can be expressed as

$$\mathbf{E} = (\epsilon_1\mathbf{p}_1 + \epsilon_2\mathbf{p}_2) \tag{1.19}$$

with the linear independent vectors $\mathbf{p}_i$ and the complex expansion coefficients ϵ_i. Including this expansion leads to:

$$\sigma(\theta_{\mathrm{cm}}) \sim |\mathbf{r}_1 \cdot (\epsilon_1\mathbf{p}_1 + \epsilon_2\mathbf{p}_2) + \mathrm{q}\mathbf{r}_2 \cdot (\epsilon_1\mathbf{p}_1 + \epsilon_2\mathbf{p}_2)\exp(\mathrm{i}\Delta\Phi)|^2 \tag{1.20}$$

The vectors $\mathbf{p}_j$ are introduced reciprocal to the Condon vectors $\mathbf{r}_j$ such that

$$\mathbf{p}_1 \cdot \mathbf{r}_1 = 1 \quad , \quad \mathbf{p}_2 \cdot \mathbf{r}_1 = 0$$

$$\mathbf{p}_1 \cdot (\mathrm{q} \cdot \mathbf{r}_2) = 0 \quad , \quad \mathbf{p}_2 \cdot (\mathrm{q} \cdot \mathbf{r}_2) = 1$$

The formula for the differential cross section then simplifies to:

$$\sigma(\theta_{\mathrm{cm}}) \sim |\epsilon_1 + \epsilon_2 \exp(\mathrm{i}\Delta\Phi)|^2 \tag{1.21}$$

calculating the square of the absolute value:

$$\sigma(\theta_{\mathrm{cm}}) \sim 1 + 2 \cdot \left|\frac{\epsilon_2}{\epsilon_1}\right| \cdot \cos(\Delta\Phi + \delta) + \left|\frac{\epsilon_2}{\epsilon_1}\right|^2 .$$

$$\text{with the real control parameter } \delta : \tag{1.22}$$

$$\delta = \arg\left(\frac{\epsilon_2}{\epsilon_1}\right), \quad \delta \in [0, 2\pi[$$

The value of the differential cross section for a given scattering angle θ_{cm} is determined by the phase difference $\Delta\phi$ of the two trajectories. The additional phase, which is introduced by the control parameter δ, opens up the possibility not only to manipulate but also to have total control over the interference pattern. δ can be shifted to any desired value by the choice of the complex expansion coefficients ϵ_i. Arbitrary values of the ϵ_i can be realized by choosing the corresponding elliptical polarization of the exciting light.

Chapter 2

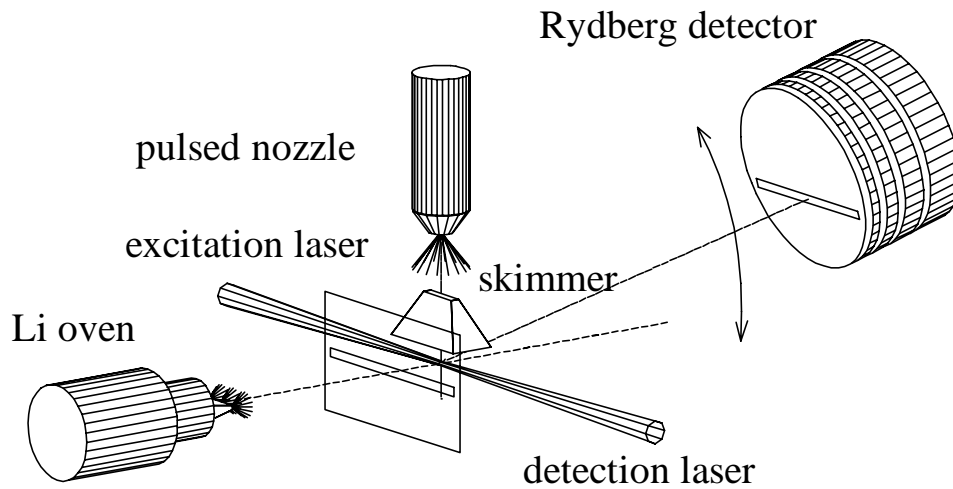# Experimental set-up

2.1 Principle components

Figure 2.1: *General scheme of the experiment: The alkali beam and the target gas beam are intersecting in the scattering volume. The counterpropagating excitation and detection lasers are aligned perpendicular to the collision plane. The rotatable Rydberg detector gauges the scattered and excited alkali atoms angle and time resolved.*

The principle components of the set-up can be seen in figure 2.1. Four beams intersect each other in the scattering volume: the alkali atomic beam produced by a two chamber oven (subsection 2.4), the supersonic rare gas or molecular beam operated with a pulsed nozzle (subsection 2.5), the excitation and the detection laser beam (subsection

The experimental apparatus	
angles between the target and the projectile beam	$90.4° - 92.3°$
angle between the laser and the particle beams	$90°$
dimensions of the scattering volume	ø 1 mm, length 10 mm
accessible laboratory scattering angle	$-18° - 92.3°$
distance scattering volume to detector	70 mm
laser pulse duration	12 - 20 ns

Table 2.1: General quantities of the experimental set-up.

2.2). In order to avoid significant losses due to scattering with the background gas it is necessary that the following collision experiments all take place in a high vacuum recipient. The vacuum recipient is made of two main chambers, which are differentially pumped. The scattering chamber, which consists of the scattering volume, the alkali beam source and the detector, is actively pumped by an oil diffusion pump. A liquid nitrogen filled cooling trap is used to decrease the resulting pressure additionally. The pressure obtains values around 10^{-6}-10^{-7} mbar without operating beams and 10^{-5}-10^{-6} mbar with beams in operation. The second chamber with the pulsed nozzle is pumped by a turbo molecular pump reaching pressures in the range of 10^{-7} mbar if the target beam source is switched off. For typical working conditions (reservoir pressure of 100 mbar, nozzle opening time around $250\,\mu$s, repetition rate of 80 Hz) the pressure increases to values of 10^{-4}-10^{-3} mbar. The two particle beams cross each other under an angle of roughly 90 degrees defining the scattering plane. The counterpropagating excitation and detection laser beams shine in perpendicular to the plane. The sizes of the beams are limited: the supersonic target beam by a skimmer, the alkali beam by an aperture in front of the oven and the laser beams by a system of blinds inside and iris diaphragms outside the vacuum chamber. The resulting shape of the scattering volume is a cylinder with ten mm length and a diameter of one mm. The scattered excited alkali atoms are detected after being transferred in a longer living Rydberg state. The target particles leave the scattering volume in their electronic ground states. The detection is done by a Rydberg detector, which is rotatable in the scattering plane and around the scattering volume (subsection 2.6). General quantities of the set-up are listed in table 2.1.

The directions of the particles before and of the projectile atoms after the collision are determined by the apertures. The velocity of the alkali particles after the collision is measured by a time of flight analysis. The velocity of the target beam before the collision can be calculated and determined indirectly (subsection 2.5). In conclusion, the internal states and all relevant velocity vectors before and after the collision are known. The collision is completely characterized.

projectile	excitation laser dye	tuning range	detection laser dye	tuning range
Li	DCM	605 - 698 nm	DMQ	342 - 385 nm
			RDC 360-NEU	338 - 365 nm
Na	Rhodamine 6G	570 - 610 nm	DPS	395 - 420 nm

Table 2.2: List of the dyes used for experiments with different projectile atoms and the appendant tuning ranges of the wavelengths (quoted from [52]).

2.2 Laser system and optical set-up

The excitation and detection photons are generated by two dye lasers (FL3002 Lambda Physik) [53] pumped by a pulsed excimer laser emitting at a wavelength of 308 nm (EMG 201 MSC Lambda Physik) [54]. Experiments with different alkali metals require dyes which match with regard to their wavelengths conditions (see tables 2.2 and 2.3).
The system allows repetition rates up to 80 Hz. The pulse-lengths of the dye lasers are among 20 and 24 ns with a maximum energy of 6 mJ. The spectral width is 0.2 cm^{-1} [53]. The typical energies of the excitation laser in the scattering volume are within the limits of 0.2 - 0.6 mJ. The detection laser is used with energies between 0.1 and 0.2 mJ.
 The optical path of the lasers and the optical set-up is shown in figure 2.2. The beam of the excimer laser is divided 1:1 by a beamsplitter and pumps the excitation and detection laser simultaneously. The telescopes enlarge the dye laser beams to a diameter of 10-20 mm.
The dye lasers not only produce a peak at the selected wavelength, they also produce a broad amplified spontaneous emision (ASE) over the wavelength range of the used dye. The intensity of the ASE is more than 10^3 smaller than the peak intensity. The fraction of the ASE which is resonant to the alkali(s $\rightarrow$ p) transition can cause background signal. The suppression of this background signal is done by a prism set-up

List of wavelength				
projectile	λ excitation laser	detuning	λ detection laser	transition
Li	660.288 nm	241.2 cm^{-1}	351.352 nm	$2p_{1/2} \longrightarrow 30d$
	660.288 nm	241.2 cm^{-1}	351.355 nm	$2p_{3/2} \longrightarrow 30d$
Na	600,368 nm	-299.7 cm^{-1}	410,155 nm	$3p_{3/2} \longrightarrow 34d$
	585,611 nm	120 cm^{-1}	410,155 nm	$3p_{3/2} \longrightarrow 34d$
	577,494 nm	360 cm^{-1}	410,155 nm	$3p_{3/2} \longrightarrow 34d$

Table 2.3: Laser wavelengths λ, detunings and detection transitions of the experiments described in this work.
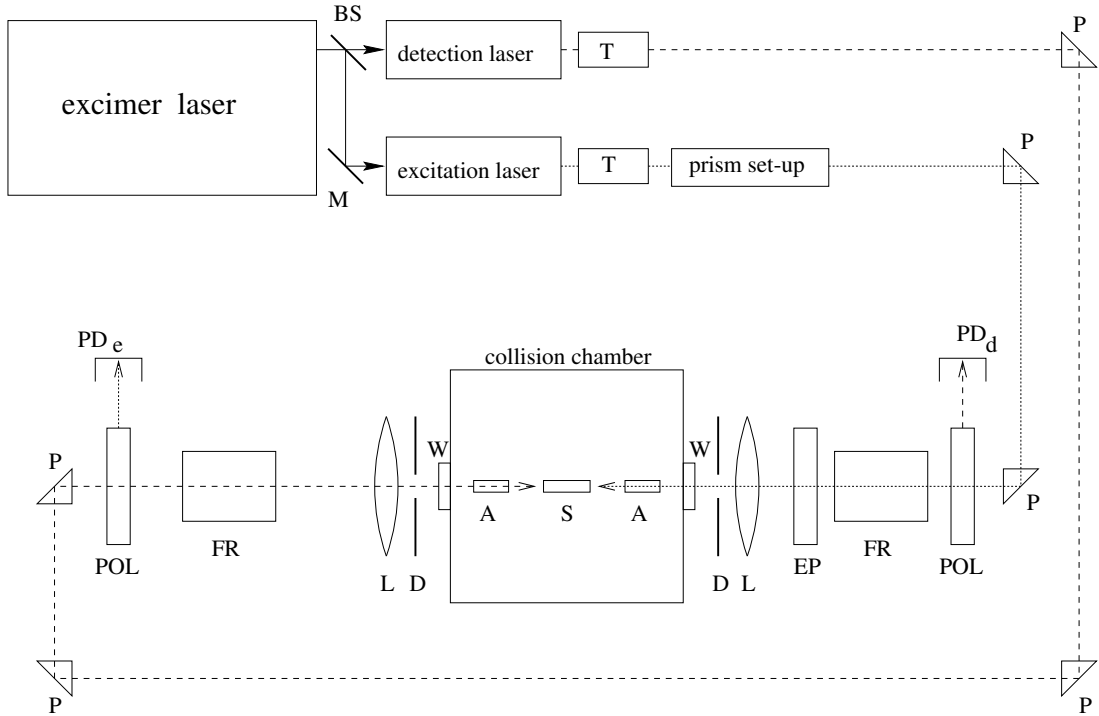
Figure 2.2: *The optical system: BS: beamsplitter, M: mirrow, T: telescope, P: prism, POL: polarization prism, FR: Fresnel rhomb, EP: λ/4 plate, L: lens, D: iris diaphragm, A: aperture, W: antireflective window, S: scattering volume, PD_e, PD_d: photodiodes for the excitation and the detection laser.*

which is described in figure 2.3. The beam of the excitation laser passes two SF 10 dispersion prisms two times, which leads to a dispersion of 10^{-3} rad/nm. By the use of two apertures in combination with the long pathway (> 10 m) of the laser beam it possible to filter the resonant fraction of the ASE.

The polarizers and the Fresnel rhombs are applied to manipulate the plane of polarization of the laser light (subsection 3.3.1). The direction of the linear polarization is adjustable within $\pm 0.9°$. The degree of linear polarization is measured to be better than 99%. In the experiments with elliptic polarized light (subsection 3.3.2) an additional $\lambda/4$ plate is added to generate the necessary elliptic polarization. The position of the main axis of the plate is adjustable within $\pm 1°$ [55]. In order to avoid unnecessary light intensity losses, coated optical components (e.g.: prisms, lenses, windows) are applied for different alkali metals.

An optimal overlap of the lasers, the target and the projectile beam leads to a well defined scattering volume. Two iris diaphragms and two adjustable lenses outside and four appertures inside the collision chamber allow to align the size and position of the scattering volume within ± 0.1 mm. The focussing of the lasers on the appertures which are behind the scattering volume relative to the laser beam direction reduce the amount of error signal by stray light. In order to evaluate the quality of the measure-
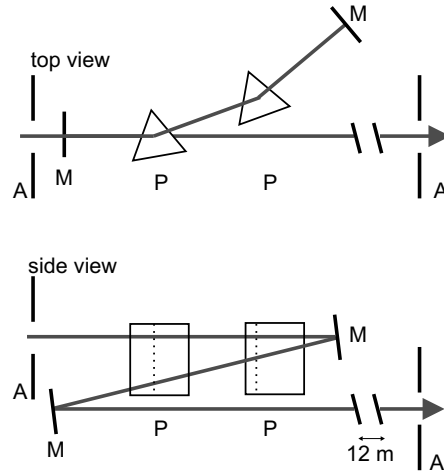
Figure 2.3: *The schematic diagram of the prism set-up is shown as top and side view in order to illustrate the three dimensional guidance of the beam. The beam of the excitation laser passes through a aperture A into the prism set-up. After passing two prisms P it is back reflected by the first mirrow (M) through the prisms again. A second mirrow (M) which is below of the plane of the prisms directs the beam through a second aperture A.*

ment it is necessary to control and monitor the laser intensities. The relative intensities of the lasers are measured by the photodiodes PD_e and PD_d after passing the collision chamber.

2.3 Calibration of the laser wavelength

The detection laser is calibrated in two steps. First the electron energy levels $T_{n,l}$ for the atomic Rydberg states are calculated by using a modified Rydberg-Ritz formula

calibration of the detection laser						
projectile	$\Delta\lambda$		quantum defect δ_t		accuracy	
	[nm]	[cm^{-1}]	[nm]	[cm^{-1}]	[nm]	[cm^{-1}]
Li	0.002	0.16	0.0005	0.04	0.0021	0.17
Na	0.002	0.12	0.0015	0.09	0.0025	0.15

Table 2.4: Uncertainties of the wavelength position $\Delta\lambda$ of the measured spectral lines relative to the calculated ones, of the calculated spectral lines due to the inaccuracy of the quantum defect δ_t and the resulting accuracy of the calibration of the detection laser in the wavelength and energy regime.
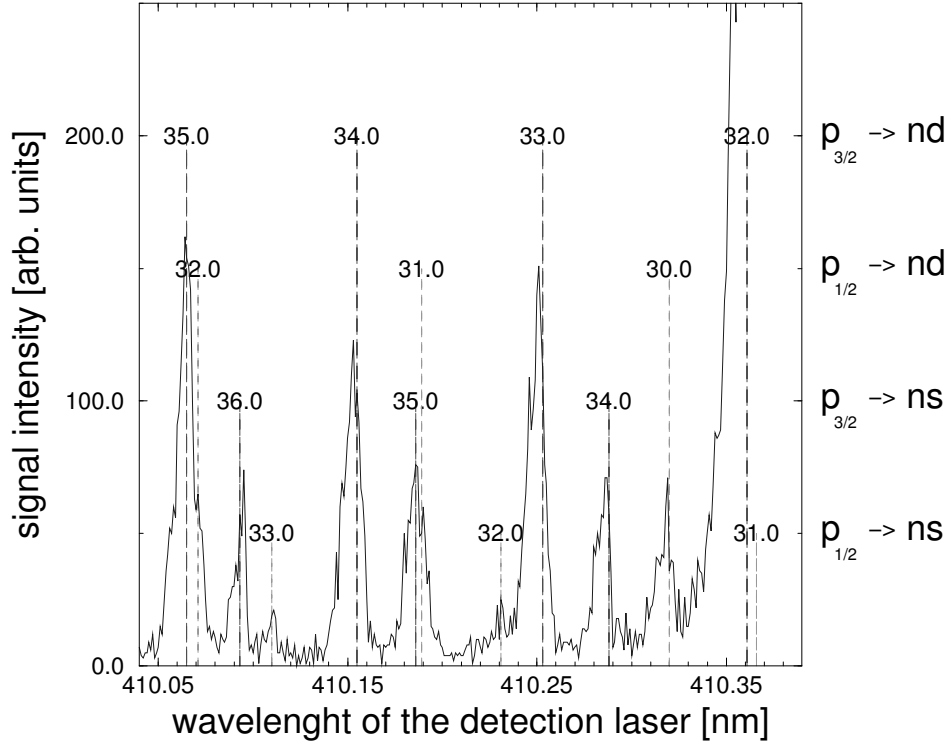
Figure 2.4: *NaNe: Spectrum of transitions from Na(3p) to different Rydberg states nl. The detuning of the excitation laser is fixed at 120 cm^{-1} and the wavelength of the detection laser is scanned. The vertical lines are the calculated positions of the transitions. The appropriate numbers are the principal quantum numbers n. The sizes of the calculated lines indicate the fine-structure of the excited state and the angular momentum l of the Rydberg state, as denoted on the right side of the graph. The strong signal on the right belongs to a two-photon line.*

[56]:

$$T_{n,l} = T_\infty - \frac{R_M}{(n - \delta_t)^2} \quad \text{with:} \quad R_M = \frac{R_\infty}{1 + \frac{m_e}{M}} \tag{2.1}$$

where T_∞ is the ionisation energy (taken from [57]) for a given electron configuration alkali(n,l) with the main quantum number n and the angular momentum quantum number l. δ_t is the corresponding quantum defect with an uncertainty of ± 1 %. It is quoted for Li and Na in [56]. R_M is the Rydberg constant of the given atom with the mass M. m_e is the electron mass and R_∞ the Rydberg constant. The result is compared with a Rydberg series measured by scanning the detection laser wavelength over ranges of 0.5 nm to 1.5 nm next to the later used detection wavelength. An example is shown in figure 2.4, significant signal only appears if the wavelength of the detection laser is resonant to a transition between the alkali(p) and a Rydberg state (nl):

$$Li(2p) \; + \; h\nu_d \longrightarrow \; Li(nl)$$

30
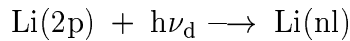
calibration of the excitation laser				
projectile	Δk [cm^{-1}]	quantum defect δ_t [cm^{-1}]	detection laser [cm^{-1}]	accuracy [cm^{-1}]
Li (I)	0.03	0.05	0.17	0.18
Na (I)	0.03	0.2	0.15	0.25
Na (II)	0.1	irrelevant	irrelevant	0.1

Table 2.5: Uncertainties of the energy position Δk of the measured spectral lines relative to the calculated ones, of the calculated spectral lines due to the inaccuracy of the quantum defect δ_t, of the calibration of the detection laser and the resulting accuracy of the calibration of the excitation laser. In the third row (II) the uncertainty in the determination of the resonance lines and the resulting accuracy of the resonance flourescence calibration are given.

$$\text{Na(3p)} + h\nu_\text{d} \longrightarrow \text{Na(nl)} \tag{2.2}$$
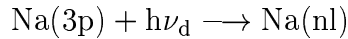
$h\nu_d$ is the energy of the detection photon. The excitation laser detuning is fixed. Due to the spectral resolution the determined calibration value $\Delta\lambda$ has an uncertainty of 0.002 nm. The accuracy of this calibration, due to the error of the given quantum defects and $\Delta\lambda$ adds up to ±0.17 cm^{-1} for lithium and ±0.15 cm^{-1} for sodium (table 2.4).
In order to calibrate the excitation laser the wavelength of the detection laser is varied over the range where two-photon excitation is expected:

$$\text{Li(2s)} \; + \; h\nu_\text{e} + h\nu_\text{d} \longrightarrow \; \text{Li(nl)}$$

$$\text{Na(3s)} + h\nu_\text{e} + h\nu_\text{d} \longrightarrow \text{Na(nl)} \tag{2.3}$$
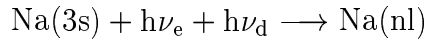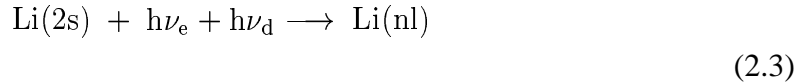
Figure 2.5 shows the dependence of the signal from the added energies of the excitation and the detection photon and the calculated positions for two-photon excitation in wavenumbers. The real excitation laser wavelength is determined from the energy difference of the calculated and detected lines. The accuracy of the calibration depends on the errors of the given quantum defects δ_t, the accuracy of the relative positioning Δk between the measured spectrum and the calculated line positions and the uncertainty of the calibration of the detection laser. The resulting accuracy is in the range of ±0.2 cm^{-1} for lithium and ±0.3 cm^{-1} for sodium (table 2.5).
A second possibility to calibrate the excitation laser is to tune it next to a resonant transition from the ground state to an excited state of the projectile. The laser wavelengths is varied slightly. At the resonance wavelength fluorescence appears and can be observed through a window in the vacuum chamber. The accuracy of this calibration (further called resonance fluorescence calibration) is about ±0.003 nm, which converts to ±0.1 cm^{-1} in wavenumbers for sodium (table 2.5). Although the resonance fluorescence calibration is more precise than comparing the calculated with the measured spectra, the
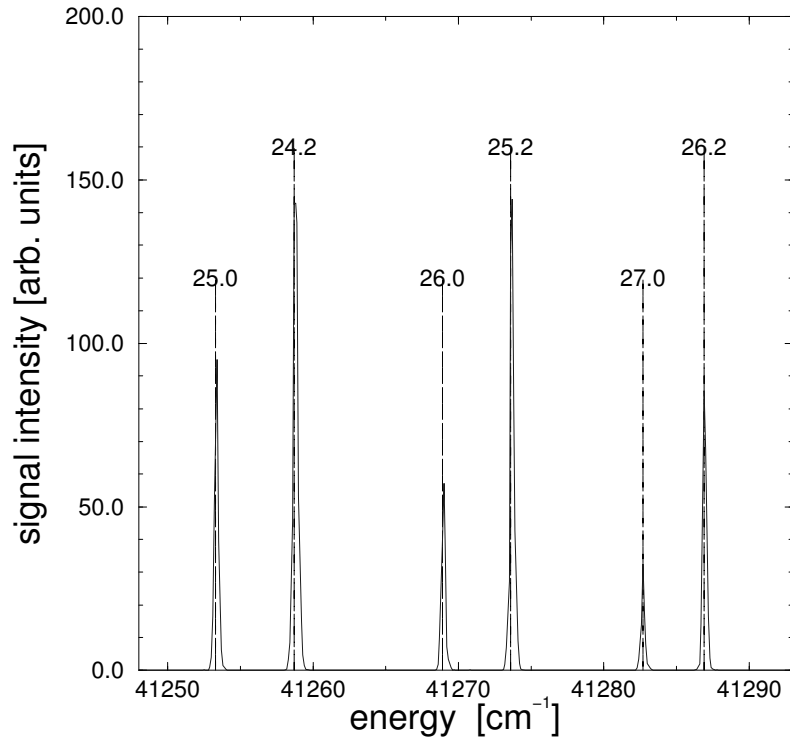
Figure 2.5: *Spectrum of 2-photon transitions from Na(3s) to different Rydberg states Na(nl) as a function of the added photon energies. The detuning of the excitation laser is fixed at -299.7 cm^{-1} and the wavelength of the detection laser is scanned. The dashed vertical lines are the calculated positions of the 2-photon transitions. The appropriate numbers are the principal quantum numbers n followed by the angular momentum l.*

method is not used for lithium because the fluorescence is in the red, where it is hard to be viewed with the naked eye.

A drift of the detection laser wavelengths during long term operation is observed but has no effect on the calibration because the excitation laser is calibrated directly after calibrating the detection laser. The detuning is not changed during a measuring period. The wavelength of the excitation laser remains fixed. The wavelength of the detection laser is more often varied, but before every measurements it is shifted to the maximum of the choosen detection transition.

2.4   Alkali beam

The alkali beam sources are illustrated in figure 2.6. The relevant geometric and physical quantities of the sources are quoted in table 2.6. Alkali dimers in the beam can

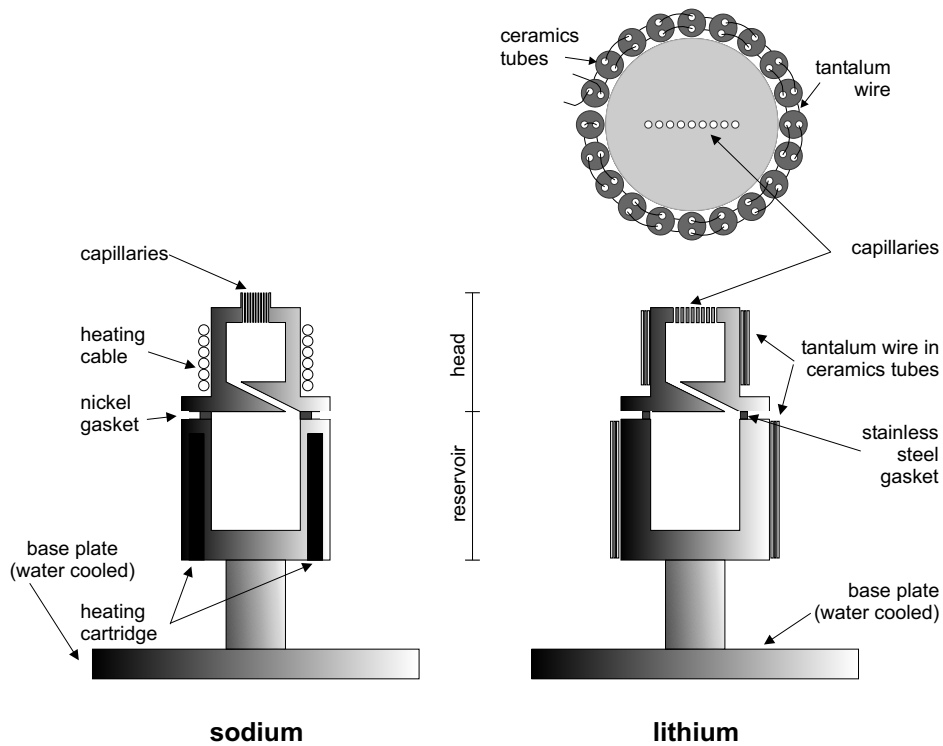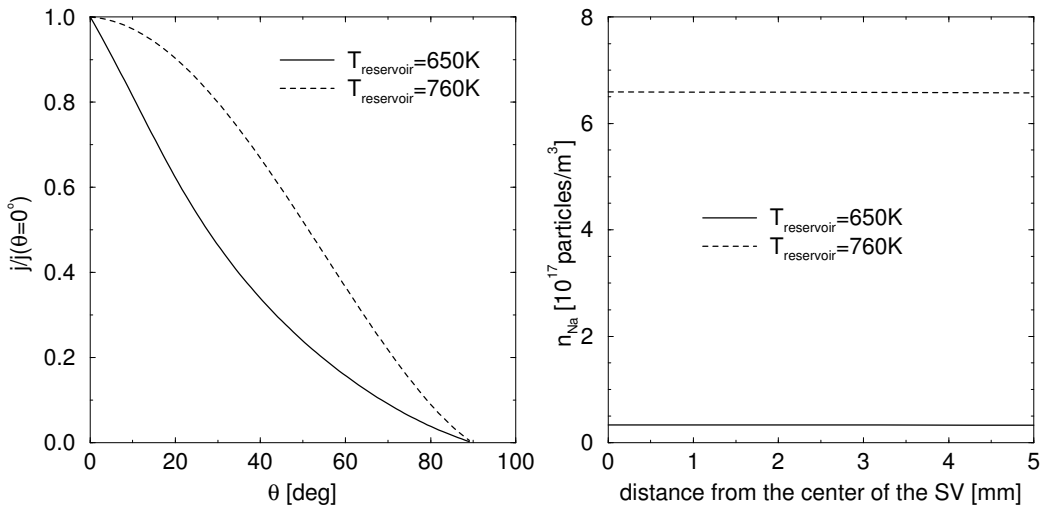Figure 2.6: *The alkali beam sources. Schematic view: Na oven on the left and Li oven on the right side.*

Figure 2.7: *left graph: Calculated angular distribution of the standardized sodium particle current density j for one capillary and two different oven reservoir temperatures. right graph: Variation of the sodium particle density over the axis of the scattering volume SV for different temperatures of the oven reservoir.*

	sodium	lithium
diameter and length of the capillaries	ø 0.8 mm, 8mm	ø 0.8 mm, 5mm
number of the capillaries	10 per 10.6-11.8 mm	9 per 10 mm
distance capillaries-scattering volume	71.2 mm	66.7 mm
aperture	1mm $\times$ 10mm	1mm $\times$ 10mm
distance aperture - scattering volume	7.2 mm	7.2 mm
temperature of the head	870-990 K	980-1020 K
temperature of the reservoir	610-650 K	830-920 K
particle density in the reservoir	0.9 - 2.9 * 10^{21}/m^3	0.2 - 1.6 * 10^{21}/m^3

Table 2.6: Relevant geometric and physical quantities of the projectile beam sources.

cause error signal. A two chamber design allows to reduce the fraction of the dimers in the beam. Both chambers are heated up to different temperatures. The first chamber (reservoir) is the source of the alkali atoms. Its temperature determines the vapor pressure of the alkali atoms and so the particle density in the whole oven and in the scattering volume. The reservoir is connected to the second chamber (oven head) by a tube. The oven head is hotter than the reservoir which increase the thermic dissociation of the dimers [58, 59]. The temperature differences between head and reservoir are chosen to values that the fraction of dimers is reduced to less than 0.15 % for lithium and 0.03 % for sodium [60, 61, 62].

The temperatures which are needed to reach sufficient lithium densities in the scattering volume are to high to use the same oven like for sodium. A new oven was developed (right picture in figure 2.6), the principle of a two chamber oven is still used, just the heating system is modified. The sodium oven works with commercial available heating cartridges [1] for the reservoir and a heating cable[2] for the head. In the lithium oven tantalium wires passing through ceramic tubes are used for both parts.

The alkali atoms leave the head through a line of capillaries. Their velocity distribution is determined by its temperature. The capillaries of the oven, a heatable aperture and the middle of the scattering volume are adjusted on one axis. Calculated angular distributions of sodium particles for one capillary and different temperatures are shown in the left graph of figure 2.7 [63]. The small angular distribution for 650 K is typical for an effusive beam [64], the more broader distribution for 760 K is an indication for a Knudsen flow [63, 65]. A Knudsen flow appears in the intermediate regime between the free molecular and gasdynamical flow [66]. The right graph of figure 2.7 illustrate the resulting sodium density in the scattering volume computed for all capillaries of the sodium oven. Only one half of the scattering volume is illustrated, because the beam is symmetrical. The particle density is almost constant over the whole volume, at both ends the density is 3 % lower than in the center.

---

[1]T+H HLP 0203, Türk+Hillinger GmbH, Tuttlingen
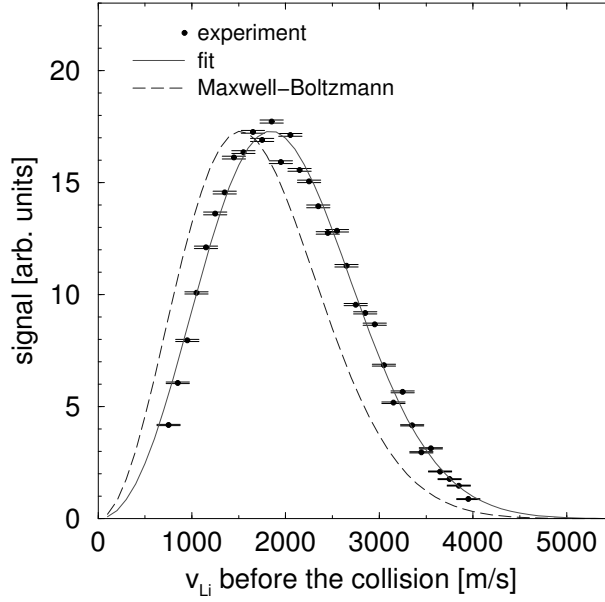[2]2ZE/15/25-44/Ti/CW2 15, Thermocoax, Stapelfeld

Figure 2.8: *The measured velocity distribution of the flux of the Lithium atoms without collisions. The dashed line is a fit on the experimental data (circles with error bars). The long-dashed line is the Maxwell-Boltzmann distribution for a temperature of the oven head of 972 K.*

The ovens are mounted on a copper plate which is part of a watercooled copper chamber. The atoms not leaving the chamber directly through the aperture, are deposited on the cold surface of the copper chamber, this leads to a reduction of the alkali background pressure in the scattering volume avoiding unintentional collisions with target or other projectile particles.

In the Knudsen regime the velocity distribution of the particles in the alkali beam is not a Maxwell-Boltzmann distribution [67] as can be seen for Li in figure 2.8 where a typical measurement of the velocity distribution is shown. The calculated Maxwell-Boltzmann distribution has a slower velocity than the experimental distribution. In order to compare experimental and theoretical results the experimental determination of the alkali velocity distribution is done regularly. The velocity of the projectile atoms is detected in $0°$ (forward) direction of the alkali beam by transferring the alkali atoms into a Rydberg state by a two photon process. The intensity of the measured velocity distribution I(v) is assumed to be proportional to the velocity distribution of the projectile density before the collision. The measured signal is fitted with the model function:

$$I(v) \sim v^2 e^{p(v)}, \tag{2.4}$$

the function p(v) is a polynom up to the second grade (for more details see [49]). The good agreement between experimental data and fit in figure 2.8 justifies the use of the model function p(v).
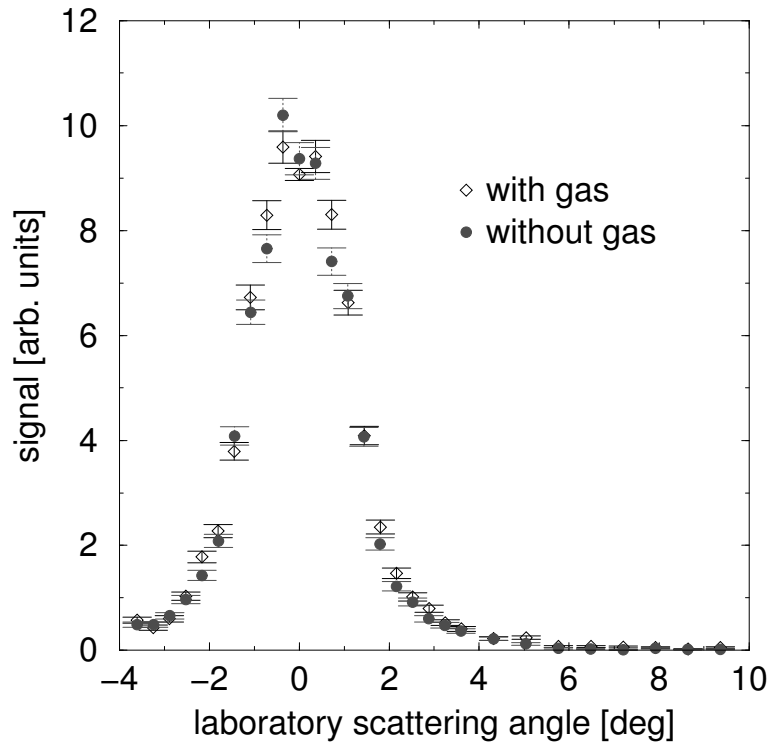
Figure 2.9: *Example of a sodium beam profile with (diamonds) and without (circles) target beam in operation. 0° is the forward direction of the beam.*

An example of a sodium beam profile is shown in figure 2.9. The measurement is done with a 3 mm aperture of the detector leading to a theoretical angular resolution of 2.5°. The full width at half maximum (fwhm) of the measured beam profile is 2.7°. The beam profile is measured by using a two photon process equivalent to the determination of the velocity distribution of the alkali atoms. This type of measurement is regularly done to determine the forward direction of the alkali beam. The accuracy of the determination of the forward direction is ± 0.3°.

2.5   Target beams

2.5.1   Atomic beams

The design of the target beam source with all geometric sizes was optimized in previous works [50, 68, 69]. It is shown in figure 2.10. The relevant quantities are given in table 2.7. The target beam is generated by a pulsed nozzle[3] driven by a pulse driver[4].

---

[3]series 9 high speed solenoid nozzle, General Valve, Fairfield
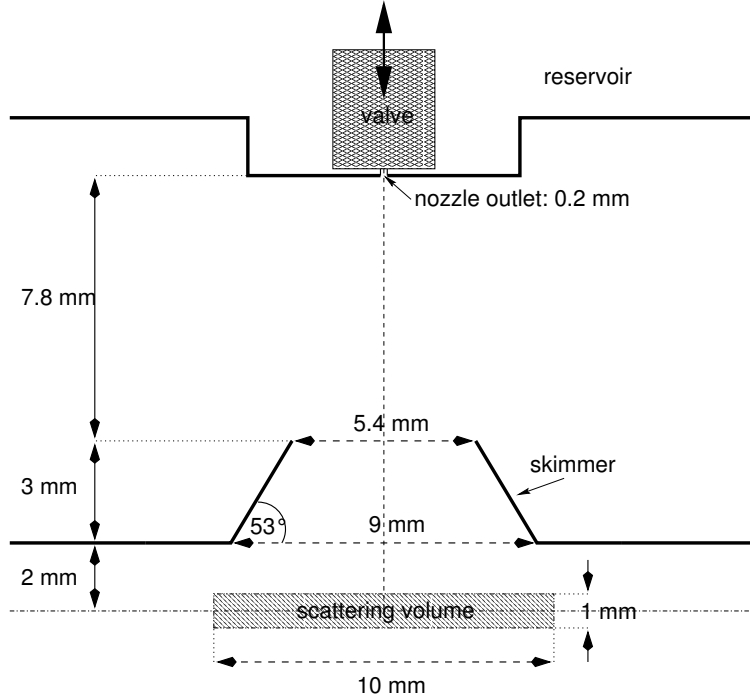[4]IOTA pulse driver, General Valve, Fairfield

Figure 2.10: *Schematic design of the target beam source with the appendant geometric dimensions.*

Before reaching the scattering volume the target beam passes a skimmer. The whole set-up leads to a supersonic expansion of the beam [65, 69]. In order to analyse the experimental data and compare the results with the theory (section 1.1.3) it is necessary to know the velocity and angular distributions of the target beam.

The velocity distribution p(v) of a supersonic beam can approximately be described by a Gaussian [70]:

$$p(v) \sim e^{-\frac{m(v-v_m)^2}{2k_B T_t}} \tag{2.5}$$

m is the atomic mass, k_B the Boltzmann constant and v_m the mean velocity. The translational temperature T_t determines the width of the distribution. v_m and T_t depend on the diameter of the nozzle orifice and the pressure in and the temperature of the gas reservoir. The velocity can be calculated with a modified gasdynamic approach for supersonic beams using a "quitting surface model" as explained in [70, 71, 72, 73]. The theoretical velocity values for the different rare gases which are used in this work are quoted in table 2.8. The error margins of the calculated velocities are determined by the accuracies in the determination of the gas temperature and of the pressure.

The velocity of neon is not directly measurable in the described set-up. The experimental verification of the theoretical values is very elaborate. The neon velocity can be determined indirectly by investigating the elastic scattering with sodium. The velocity distributions of the alkali beam before and after the collision are needed for the calculations and are presented in figure 2.11. The velocity of the sodium after the optical

The target beam source	
target gases	He, Ne, H_2, D_2
reservoir pressure	100 mbar
diameter of the nozzle outlet	0.2 mm
duration of the nozzle control pulse	Li:250 μs
	Na: 400 μs
pulse frequency	80 Hz
distance nozzle - scattering volume	variable
	Li: 12.8 mm
	Na: 12.8 mm
distance skimmer - scattering volume	5.02 mm
inclination of the skimmer	53°
aperture of the skimmer	5.38 mm × 0.76 mm

Table 2.7: Relevant geometrical and physical quantities of the target beam source.

collision is calculated taking into account the measured sodium velocity distribution, the calculated neon velocity distribution and the other relevant experimental resolutions as described in section 1.1.3. The result of this procedure is compared with the experimental data. Due to the fact that the Na velocity distribution is too broad to see significant effects of a varying neon velocity, a smaller distribution is needed. The experimental set-up is modified by inserting a chopping wheel into the projectile beam as described in detail in [63].

The measured velocity distribution of the unscattered sodium can be approximated by a Gaussian because it is narrowed by the chopping wheel. The maximum of the in figure 2.11 illustrated example is at (1366.6 ± 3) m/s and the full width at half maximum is $(2 * 138 \pm 3)$ m/s. The sodium velocity is reproduced within $\pm$ 3 m/s. The Neon velocity is determined to (743 ± 18.5) m/s by an iterative procedure. Taken into account the uncertainties of the other quantities used to calculate the theoretical data the total uncertainty in the experimental determination of neon sums up to ± 21 m/s. The theoretical value of 762 m/s is reproduced within the experimental error margins. Due to the fact that the theoretical velocity of neon and also argon [49] are experimentally reproduced within ± 3 %, the theory is assumed to describe the velocities of rare gases with an error margin of ± 3 %. The resulting velocity of helium is (1701 ± 50) m/s.

For one set of NaNe experiments using elliptical polarized light it was necessary to increase the reservoir pressure of Ne to a value of 300 mbar. In previous works [63, 49] a shift of the Ne and Ar velocities to lower values than the calculated ones was observed for reservoir pressures higher than 100 mbar. The rare gas velocity has a distribution somewhere between the a supersonic and a thermal distribution. The underlying process is not understood, yet. This effect leads to a higher uncertainty in the determination of the Ne velocity. However, a value of 769 m/s is used for the convolution procedure.
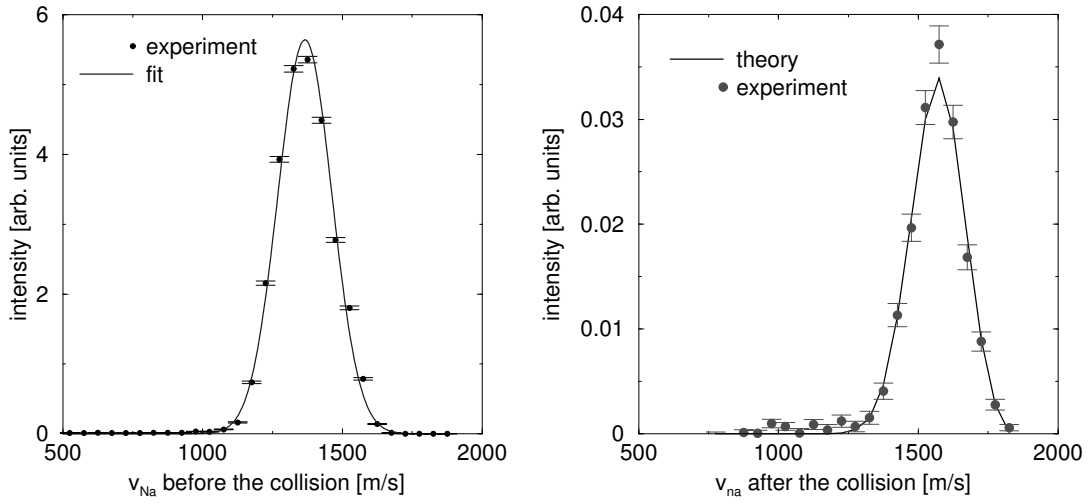
Figure 2.11: *Experimental test of the neon velocity. Left: Measured velocity distribution of the unscattered sodium (data points with error bars) and the corresponding Gaussian fit (line). Right: Calculated (line) and measured (data points with error bars) velocity distribution of the sodium after the collision (detuning: 360 cm^{-1}, θ_{lab}: 10.8°).*

The angular distribution I(Θ) of the target beam is given by:

$$I(\Theta) \sim \cos^2(1.15\Theta) \tag{2.6}$$

and illustrated on the left side of figure 2.12 [70]. The resulting calculated normalized density distribution of the target atoms in the scattering volume for the applied distance between nozzle and scattering volume is shown on the right side of figure 2.12. The density at both ends of the scattering volume is around 90% of the density in its center.

target	reservoir temperature	reservoir pressure	mean velocity	T_t
He	$(290 \pm 2.5)°$K	(100 ± 5) mbar	(1701 ± 7) m/s	$11(.3)°$
Ne$_{(1)}$	$(290 \pm 2.5)°$K	(100 ± 5) mbar	(762 ± 3) m/s	$8(.2)°$
Ne$_{(2)}$	$(290 \pm 2.5)°$K	(300 ± 5) mbar	(769 ± 3) m/s	$2(.7)°$
Ne$_{(3)}$	$(290 \pm 2.5)°$K	(100 ± 5) mbar	(762 ± 3) m/s	$8(.2)°$

Table 2.8: Left: The used temperatures and pressures of the gas reservoir for different target atoms and the appropriate experimental accuracies. The indices mark the appropriate experiment (1: NaNe; 2: NaNe, elliptical polarized light; 3: LiNe). Right: Resulting calculated mean velocities with the corresponding error margins and the translational temperature T_t. The indices at the rare gases mark the collisional system.
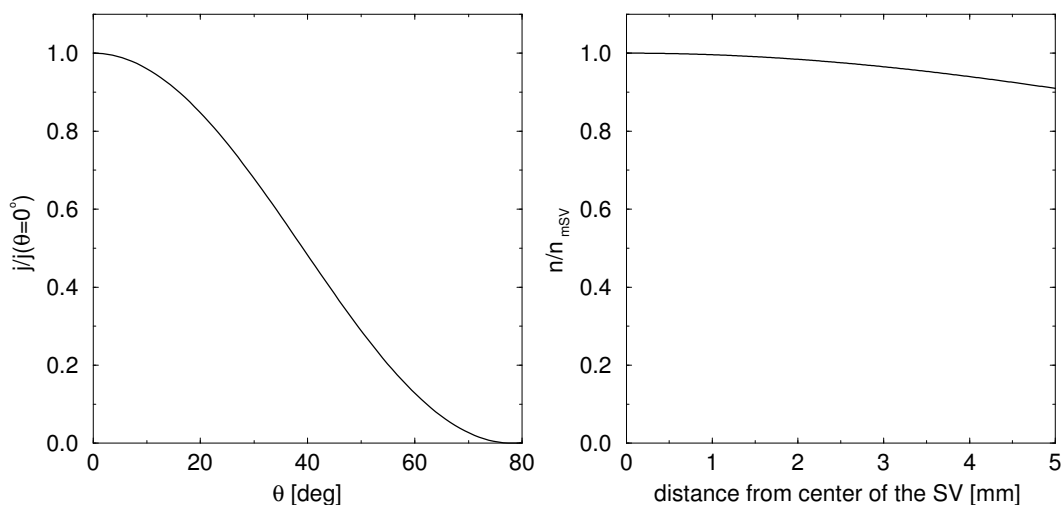
Figure 2.12: *Left: calculated angular distribution of the standardized rare gas particle current density j; right calculated rare gas distribution in the scattering volume SV.*

target	reservoir temperature	reservoir pressure	mean velocity	T_t
H_2	$(290 \pm 2.5)\,°K$	$(100 \pm 5)\,mbar$	$(2413 \pm 10)\,m/s$	$7(.5)°$
D_2	$(290 \pm 2.5)\,°K$	$(100 \pm 5)\,mbar$	$(1714 \pm 7)\,m/s$	$7(.4)°$

Table 2.9: Left: The used temperatures and pressures of the gas reservoir for different target molecules and the appropriate experimental accuracies. Right: Resulting calculated mean velocities with the corresponding error margins and the translational temperature T_t.

2.5.2 Molecular beams

In order to produce a molecular target beam with H_2 and D_2 the same source as for rare gases is used.

While atoms have just translational degrees of freedom, molecules have additional inner degrees of freedom (vibrational and rotational). Due to quantum mechanical effects the number of degrees of freedom in a gas ensemble may depend on the temperature [70]. Therefore the determination of the velocity distribution of molecular beams is more complex as for atomic beams, especially for H_2 and D_2. If all parameters of a special molecule are known with high accuracy the quitting surface model is applicable. This is typically not the case for molecules.

Measurements done for molecules in the context of [63] give an indication that for H_2 and D_2 the inner degrees of freedom do not contribute. Therefore it is assumed that the vibrational and rotational energies remain constant. Under this condition a quitting surface model treating the molecules as atoms is used for the applied experimental specifications (furthermore referred to as the "simplified model").
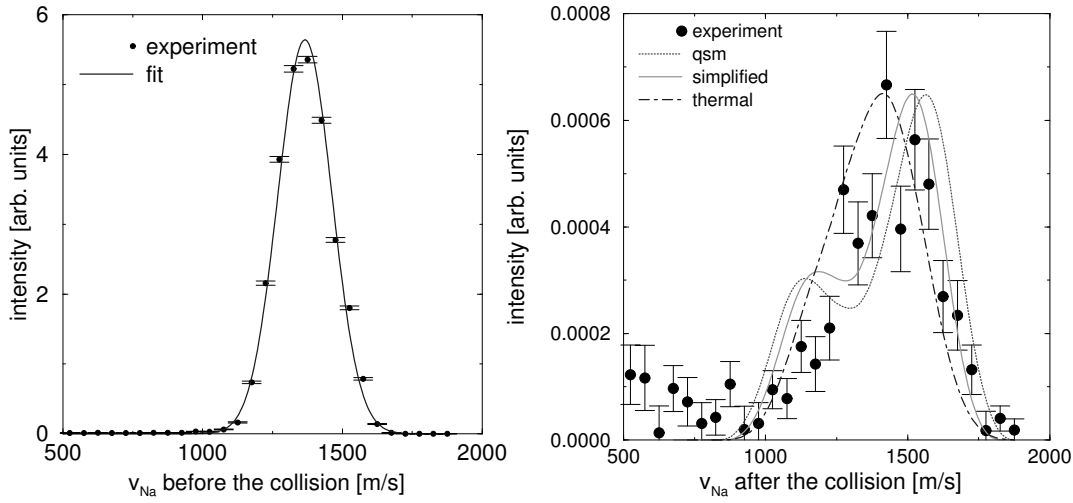
Figure 2.13: *Experimental test of the H_2 velocity. Left: Measured velocity distribution of the unscattered sodium (data points with error bars) and the corresponding Gaussian fit (line). Right: Experimental (data points with error bars) and calculated Na velocity distributions. The dotted line is the calculated distribution for the quitting surface model (qms) with a v_{mH_2} of 2900 m/s, the solid line for the simplified model with v_{mH_2} of 2400 m/s and the dashed dotted line for a thermal beam. Detuning: 120 cm^{-1}, θ_{lab} : 10.8°.*

In order to prove the described assumptions an experiment is arranged equivalent to the determination of the neon velocity (subsection 2.5.1). In figure 2.13 measured velocity distributions of sodium before and after the collision with H_2 molecules are shown. The three curves are calculated velocity distributions for collisions with a thermal model, the simplified model and the quitting surface model for the target gas beam. The noticeable shoulder is due to ambiguities in the collisional geometry of the NaH_2 system and not caused by the shape of the H_2 or Na velocity distributions.

The curve for the simplified model fits most satisfactory. Taking into account the error statistics of the experimental data this means that the simplified approach seems to be the most likely. An indirect determination of the H_2 velocity, like for Ne is not possible with reasonable error margins. The velocity values calculated with the simplified quitting surface model are quoted in table 2.9. The error margins of the calculated velocities are determined by the accuracies in the determination of the gas temperature and of the pressure. Including the experiences with atomic targets (2400 ± 100) m/s for H_2 and (1700 ± 70) m/s for D_2 are reasonable estimates for the molecular velocities and the accuracy in their determination.
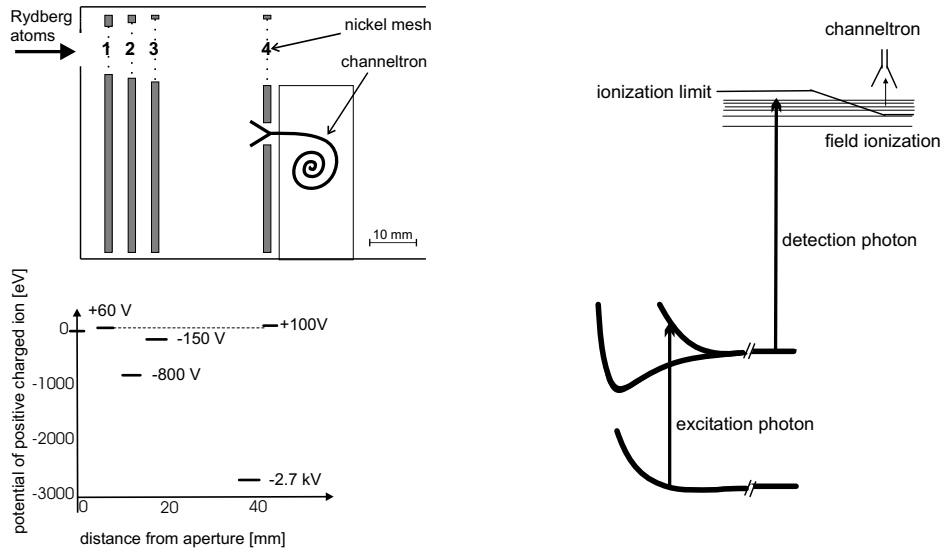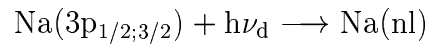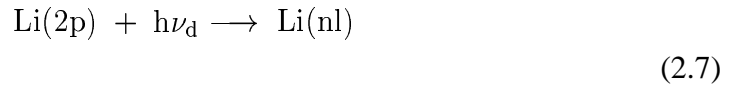
Figure 2.14: *Principle of detection. Left: The schematic design of the Rydberg detector (top) with the appropriate impressed electric potentials of the meshes (bottom). Right: The detection scheme demonstrated by the belonging potential energies, the collisional complex is excited by the first photon, then transfered into a Rydberg state, field ionized and detected in the channeltron.*

2.6 Differential detection

The alkali atoms are in the first excited p-state after the optical collision. The lifetimes of the excited Li(2p) and Na(3p) atoms are in the order of a few nanoseconds [74]. In the relevant velocity regime (400 - 3600 m/s) the particles would not be able to leave the scattering volume before decaying into their ground states. The detection laser photons transfer the excited alkali atoms in Rydberg states.

$$\mathrm{Li(2p)} \; + \; \mathrm{h}\nu_\mathrm{d} \longrightarrow \; \mathrm{Li(nl)}$$

$$\mathrm{Na(3p_{1/2;3/2})} + \mathrm{h}\nu_\mathrm{d} \longrightarrow \mathrm{Na(nl)}$$

(2.7)

The lifetimes of the Rydberg states are orders of magnitude longer than of the first excited p-states. The collisions between Rydberg atoms and the background gas particles are causing inelastic changes of the angular momentum quantum number l which prolong the lifetime of the Rydberg atoms [58, 50]. The Rydberg atoms reach the detector and are ionized by an electric field.

In figure 2.4 an overlap of the Na($3p_{1/2} \to 31d$) and the Na($3p_{3/2} \to 35s$) transitions and a rising of a 2-photon line (see equation 2.3) at 410.33 nm is observable. The signal amplitude of this process is orders of magnitude higher than the signal of optical collisions. The wavelength of the detection laser has to be chosen carefully. Only

detached lines with high signal intensity like for example the

$$\mathrm{Na(3p_{3/2})} + \mathrm{h}\nu_\mathrm{d} \longrightarrow \mathrm{Na(34d)}$$
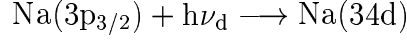
transistion are used as detection lines for the later on described experiments.

The design of the detector is shown in upper left part of figure 2.14. The Rydberg atoms pass an aperture ($\mathrm{Na}_{120cm^{-1}}$: 15 mm × 1.5 mm; $\mathrm{Na}_{-299.7cm^{-1}}$: 20 mm × 3.0 mm; Li: 30 mm × 3.0 mm) and a composition of nickel meshes with different electric potentials (lower left part of figure 2.14) in respect to the ground potential of the vacuum recipient . The first and the fourth mesh are on positive potentials (+60 V and +100 V) in order to repel positive ions which might be present in the recipient. The electric field between the first and the second mesh (170 KV/m) is strong enough to field ionize Rydberg atoms of quantum numbers higher than n=15 [75]. The ionization takes place close-by the first mesh. The ions produced in the ionization volume have to be guided onto the entrance of a channeltron [76], because the channeltron is not visible for the neutral projectile particles in order to avoid the deposition of alkali atoms. The entrance of the channeltron itself is on a high negative potential (-2.7 KV) to attract the ions and to repel electrons which might enter the detector. Around 70 % of the produced Rydberg atoms reach the detector and 70 % of those are detected by the channeltron [58, 50]. The resulting total efficiency of the detection scheme is 50 % of the arisen Rydberg atoms.

In order to determine the velocity of the scattered alkali atoms, the time of flight from the scattering volume to the ionization volume at the first mesh has to be measured. The distance is (70 ± 0.3) mm. The time zero point is in the moment when the detection laser illuminate the scattering volume and the Rydberg atoms are produced. It is determined by a photodiode in the detection laser. A multichannel analyser PC-Card [77] (MCD-2 card) measure the time difference t between the photodiode pulse and the amplified pulse orginated in the channeltron. t has to be corrected for all time delays orginated in running times of the electric pulses in the cables, processing times in the preamplifier, differences in processing times in the MCD-2 card and the travel time of light from the laser to the scattering volume. All delays sum up to 68 ns. The real time of flight t_r is

$$\mathrm{t_r} = \mathrm{t} - \mathrm{t_i} - 68\mathrm{ns}, \tag{2.8}$$

where t_i is the time of flight of the ions in the detector, which is different for Li (461 ns) and Na (840 ns). t_i is calculated with the software package SIMION [78] by simulating the pathways of ions inside the detector.The uncertainties in the time determination sum up to an uncertainty of ± 80 ns of t_r leading to ± 0.1 % accuracy in velocity determination for Na (1000 m/s) and ± 0.3 % for Li (2400 m/s). The inaccuracy in the path length causes additional 0.4 % for Li and Na. The total uncertainty of the scattered projectile velocity is ± 0.5 % for Na and ± 0.7 % for Li.

The detector is mounted on a swivel arm. The relative reproducibility of the swivel

experimental quantities	section	error margin
detuning	2.2	Li: ± 0.17 cm^{-1}
		Na: ± 0.15 cm^{-1}
polarization angle	2.2	$\pm 0.9°$
velocity distribution of the target beam before the collision	2.5	v_{mHe}:(1701$\pm$50) m/s
		v_{mNe}: (762$\pm$20) m/s
		v_{mH_2}: (2413$\pm$100) m/s
		v_{mD_2}: (1714$\pm$70) m/s
velocity distribution of the projectile beam before the collision	2.4	Δ v ± 6 %
dimension of the scattering volume: distance	2.2	± 0.1 mm
angle	2.6	$\pm 0.1°$
dimension of the aperture of the detector	2.6	± 0.1 mm
geometrical sizes and distances	2	± 0.3 mm
different time of flights of different projectile ions in the detector	2.6	Li: (461$\pm$80) ns
		Na. (840$\pm$80) ns
resolution of the velocity of the scattered atoms	2.6	Na: ± 0.5 %
		Li: ± 0.7 %
position of the detector	2.6	absolute: $\pm 0.3°$
		relative: $\pm 0.04°$
determination of the scattering angle	2.6	$\pm 0.3°$
angle between target and projectile beam	2.6	$\pm 0.3°$

Table 2.10: Relevant experimental quantities to determine the apparatus function and the appendant error margins.

arm position is better than 0.04°. The scattering angle is the angle between the forward direction of the projectile beam and the axis of the detector. The determination of the foward direction has an accuracy of 0.3° (section 2.4). An additional error of $\pm 0.1°$ is caused by the error margin of the position and size of the scattering volume (± 0.1 mm). The total uncertainty in the scattering angle is $\pm$ 0.3°.

The angle between the projectile and the target beam is measured for the experiments in chapter 3 because it depends on the beam sources and their mounting and can vary up to 2°. Using an extra 0.8 mm $\times$ 8 mm aperture the direction of the alkali beam is measured equivalent to the foward direction measurement 2.4. The direction of the target beam is determined by changing the Rydberg detector with an ionisation gauge keeping the extra aperture. The total uncertainty of the angle between the beam is mainly caused by the accuracy in the determination of the target beam direction and is about $\pm$ 0.3°. In table 2.10 the relevant experimental quantities to compare the theoretical with the experimental results and the appendant error margins are centralised.

2.7 Control of the experiments

The whole experiment is controlled automatically by a computer using programs written in LabView from National Instruments [79]. The computer is able to switch the target beam on or off by controlling the pulsed nozzle, to change the repetition rate and the number of laser shots, to conduct step motors in order to vary the detection angle by rotating the detector, to alter the wavelength of both lasers by tilting the gratings, to change the polarization plane of the lasers by turning each of the two Fresnel rhombs or to vary the elliptic polarization by turning one Fresnel rhomb and the $\lambda/4$ plate. The communication between the computer and the dye-lasers is done by a GPIB interface (National Instruments PCI-GPIB+). The other hardware is connected with the computer via a DaqBoard from IOTech [80].

In order to run the later described experiments it is necessary to create and use different control files for different applications. At the beginning the relevant physical parameters of each data point (like detector position, polarization, number of laser shots, etc.) are set. The events counted by the detector are distributed time resolved to the 4096 channels of a multichannel analyzer PC-Card (MCD-2 card)[77]. Each channel corresponds to a time interval of 125 ns. The computer reads out the channels after every data point and sorts the events into velocity classes (up to 28 with a width of 50 m/s - 200 m/s). Then the physical parameters of the next data point are adjusted. The measurement is stopped after a given number of data points or runs in a loop until it is stopped manually. During the measurement the experimental data is automatically transferred to another computer after a given number of data points. Further analysis allows an observation of the counting statistics and to evaluate the quality of the measurement. At data points with an expected low signal intensity a higher number of laser shots is programmed to have a nearly equal counting statistic over the whole range of the measurement. Typical loops are programmed in a way that when all data points with the appropriate settings are measured, the order of the data points is measured backwards again. The feasible slight linear decrease of the laser intensity and its effect to the signal intensity is averaged out by this kind of loop. Additionally the adjustment is always controlled and if necessary corrected during longtime measurements in order to measure in the optimal working range of a specific experiment.

2.8 Disturbing processes and corrections

2.8.1 Disturbing processes

The measured entire signal of the later on described experiments (chapter 3) is a composition of the real signal and background signal. Typical signal intensities of 0.01 - 0.2 counts per laser shot are to small to deal with high background signal. The signal intensity should, apart from saturation effects, depend linear from the intensities of the

excitation laser, the detection laser, the sodium beam and the target beam (equation 2). Observed nonlinearities are an indication for the following competing processes discribed in [58, 51]:

1. **Collisions with alkali dimers**

2. **Excitation with resonant light**

3. **Direct 2-photon detection**

4. **Detection during the collision**

5. **Hyper-Raman excitation**

6. **Alkali-alkali optical collisions**

The contributions to the background signal of most of the above mentioned processes can be and are reduced significantly (like processes 1. - 4.) by the right choice of the experimental parameters and modications in the experimental set-up. The resulting error margins are small compared to the statistical error of the entire signal. Due to the quadratic dependence of the background signal on the excitation laser intensity (process 5.) or the alkali particle density (process 6.) in the scattering volume the fraction of the background signal of the entire signal can be reduced decreasing the intensity of the laser (process 5.) or of the sodium (process 6.) beam. However, the signal intensity is decreased, too. Thus the reduction is limited. The optimal working conditions are always a compromise between moderate signal and a small background.
The background signal is minimized in a way that all remaining contributions to the entire signal sum up to less than 25 %. The entire signal then has to be corrected in respect to the underlying processes.

2.8.2   Methods of correction

In order to subtract the background signal caused by the remaining processes, all measurements are done with (S_g) and without target gas (S_{wg}). The background signal is dominated by the processes 5. and 6. which do not need target particles. A systematical error is introduced not taking into account the elastic scattering of the background signal with the target gas. For the alkali-alkali process the resulting error is small ($\pm$ 5% of the background signal caused by this process) because the angular distribution of the process is already broad [58]. For the hyper-Raman it has to be corrected. S_{wg} is in a small area around ($\pm 3°$) the forward direction dominated by the hyper-Raman (S_{hR}) and for bigger scattering angles by the alkali-alkali process (S_{aa}). S_{aa} can be interpolated for small scattering angles from the broad angular distribution of S_{wg}.
The distribution of hyper-Raman process can assumed to be like the distribution of the

direct 2-photon process. Thus the angular distribution of a 2-photon photon process is measured with and without target particles. The detected signal without gas in forward direction (S_{wg0}) subtracted by the interpolated value of S_{aa} in forward direction (S_{aa0}) is divided by the signal in forward direction of the 2-photon peak without gas ($2P_{wg0}$) and multiplied with the angular distribution of the 2-photon signal with gas ($2P_g$), the resulting distribution is the elastic scattered contribution of the hyper-raman process to the background signal:

$$S_{hR}(\theta) = \frac{S_{wg0} - S_{aa0}}{2P_{wg0}} \; 2P_g(\theta) \tag{2.9}$$

It has to keep in mind that $S_{hR}(\theta)$ is for all but small scattering angles in the order of less than 2 % of $S_g(\theta)$ for the here presented measurements.
The background corrected signal $S(\theta)$ is:

$$S(\theta) = S_g(\theta) - S_{aa}(\theta) - S_{hR}(\theta) \; . \tag{2.10}$$

The effect of angular momentum stabilization of the Rydberg atoms described in section 2.6, might cause a systematical error in this background correction procedure due to the fact that the background signal is stabilized by the target gas as described in [63]. In this work no significant stabilization effect is observed for the used target gases. As can be seen for the example in figure 2.9, the 2-photon signal in forward direction without gas is minimal higher than the 2-photon signal with gas. For scattering angles greater than 2° it is vice versa. This is the expected behavior due to elastic scattering of the alkali atoms with the target particles.

Chapter 3

Results and discussion

3.1   General introduction

In this chapter experimental and theoretical determined differential cross sections of the collisional pairs LiHe, LiNe, LiH_2, LiD_2 and NaNe for various detunings and polarizations of the excitation laser are presented in order to probe molecular potentials and to observe and to manipulate the collision processes.

The notation for all graphs is equivalent. Each graph of a figure belongs to a velocity class of the scattered alkali atoms. If the velocity is labeled, it is the medial velocity of the class. The circles represent the experimental data. Their error bars denote $\pm$ one standard deviation of the counting statistics. The background signal is subtracted as described in section 2.8.2. The presented theoretical determined cross sections are all convoluted with the corresponding apparatus function of the experiment (section 1.1.3). They are diagrammed as lines. Different line styles belong to different underlying potentials.

3.2   Probing of molecular potentials by measuring differential cross sections

3.2.1   LiNe and LiHe

The optical collisions of lithium with different atomic targets (He, Ne) are examined. The differential cross sections for a positive detuning of 241.7 cm^{-1} from the Li(2s - 2p) resonance and 24 velocity classes of the scattered lithium were measured and shown in figures 3.1 - 3.4. The width of the velocity classes is 75 m/s for LiNe and 100 m/s for LiHe. The polarization of the excitation laser is fixed. The detected state is the
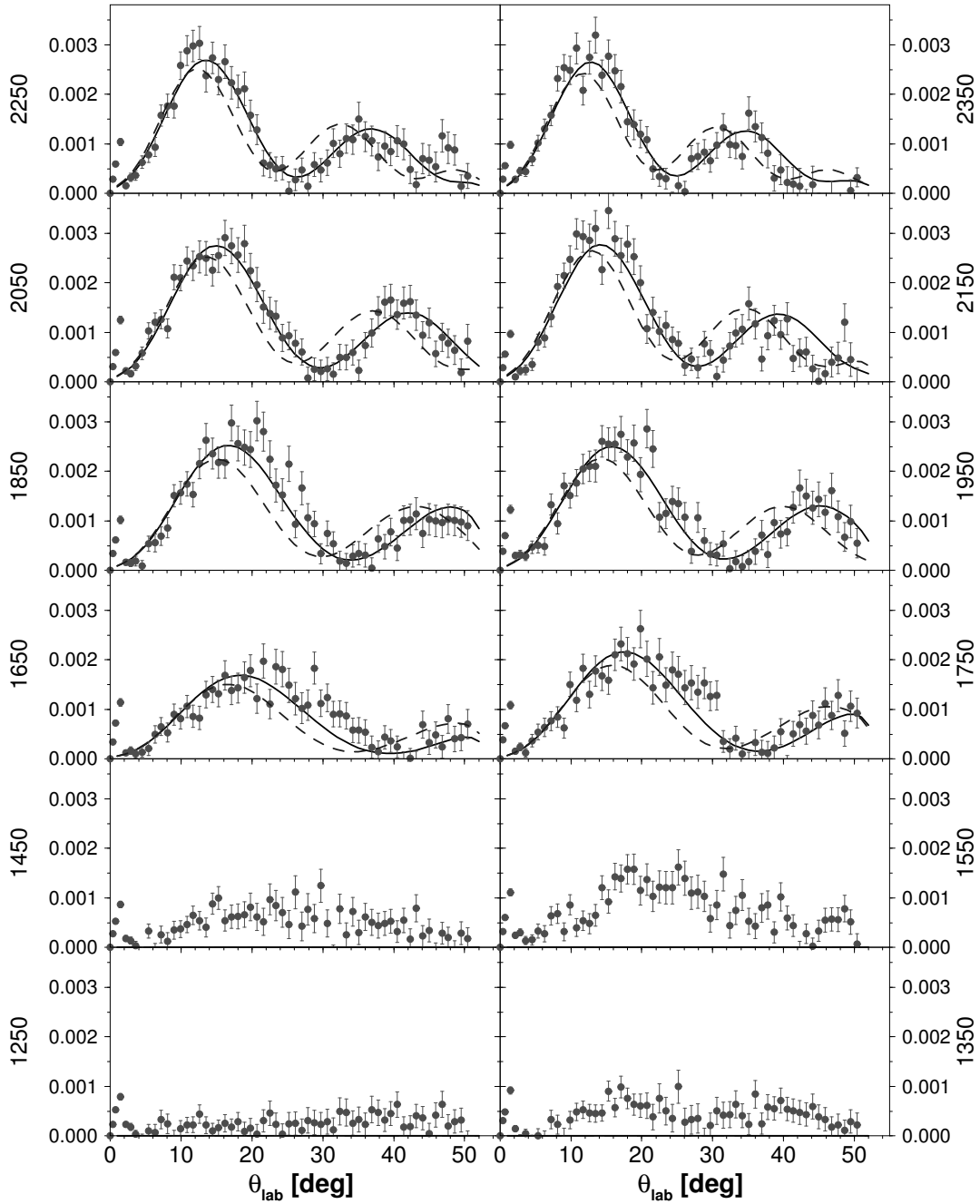
Figure 3.1: *Differential cross sections of LiHe as a function of the laboratory scattering angle θ multiplied by sin(θ) for different velocities. The vertical numbers at the left (left column) and right (right column) sides of the graphs indicate the appropriate velocity of the lithium after the collision in m/s. The detuning is 241.7 cm^{-1}. Circles: Experimental data. Curves: Theory calculated with underlying potentials from [18] (solid lines) and [19] (dashed lines).*
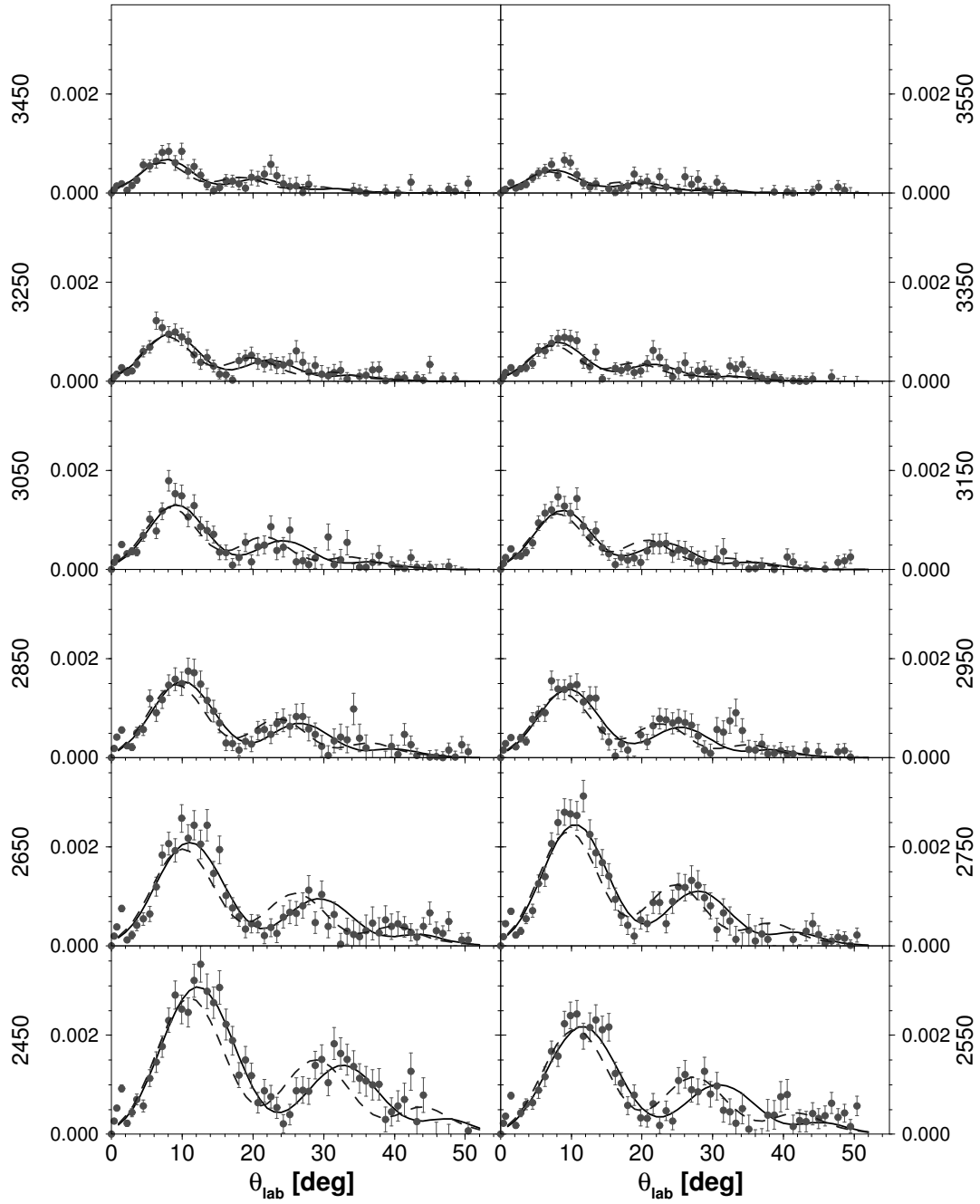
50

Figure 3.2: *Differential cross sections of LiHe as a function of the laboratory scattering angle θ multiplied by sin(θ) for different velocities. The vertical numbers at the left (left column) and right (right column) sides of the graphs indicate the appropriate velocity of the lithium after the collision in m/s. The detuning is 241.7 cm^{-1}. Circles: Experimental data. Curves: Theory calculated with underlying potentials from [18] (solid lines) and [19] (dashed lines).*
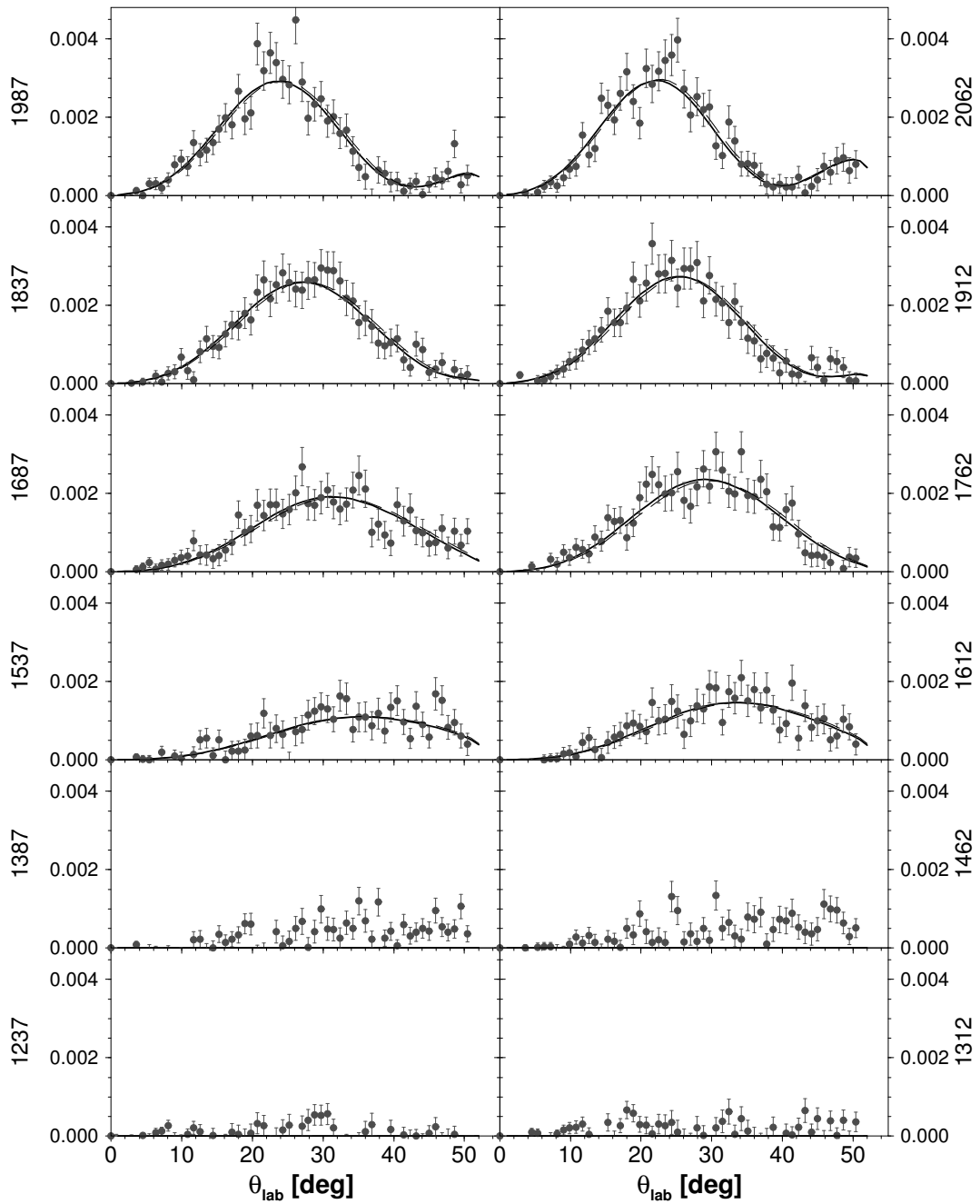
51

Figure 3.3: *Differential cross sections of LiNe as a function of the laboratory scattering angle θ multiplied by sin(θ) for different velocities The vertical numbers at the left (left column) and right (right column) sides of the graphs indicate the appropriate velocity of the lithium after the collision in m/s. The detuning is 241.7 cm^{-1}. Circles: Experimental data. Curves: Theory.*

Figure 3.4: *Differential cross sections of LiNe as a function of the laboratory scattering angle θ multiplied by sin(θ) for different velocities. The vertical numbers at the left (left column) and right (right column) sides of the graphs indicate the appropriate velocity of the lithium after the collision in m/s. The detuning is 241.7 cm^{-1}. Circles: Experimental data. Curves: Theory.*
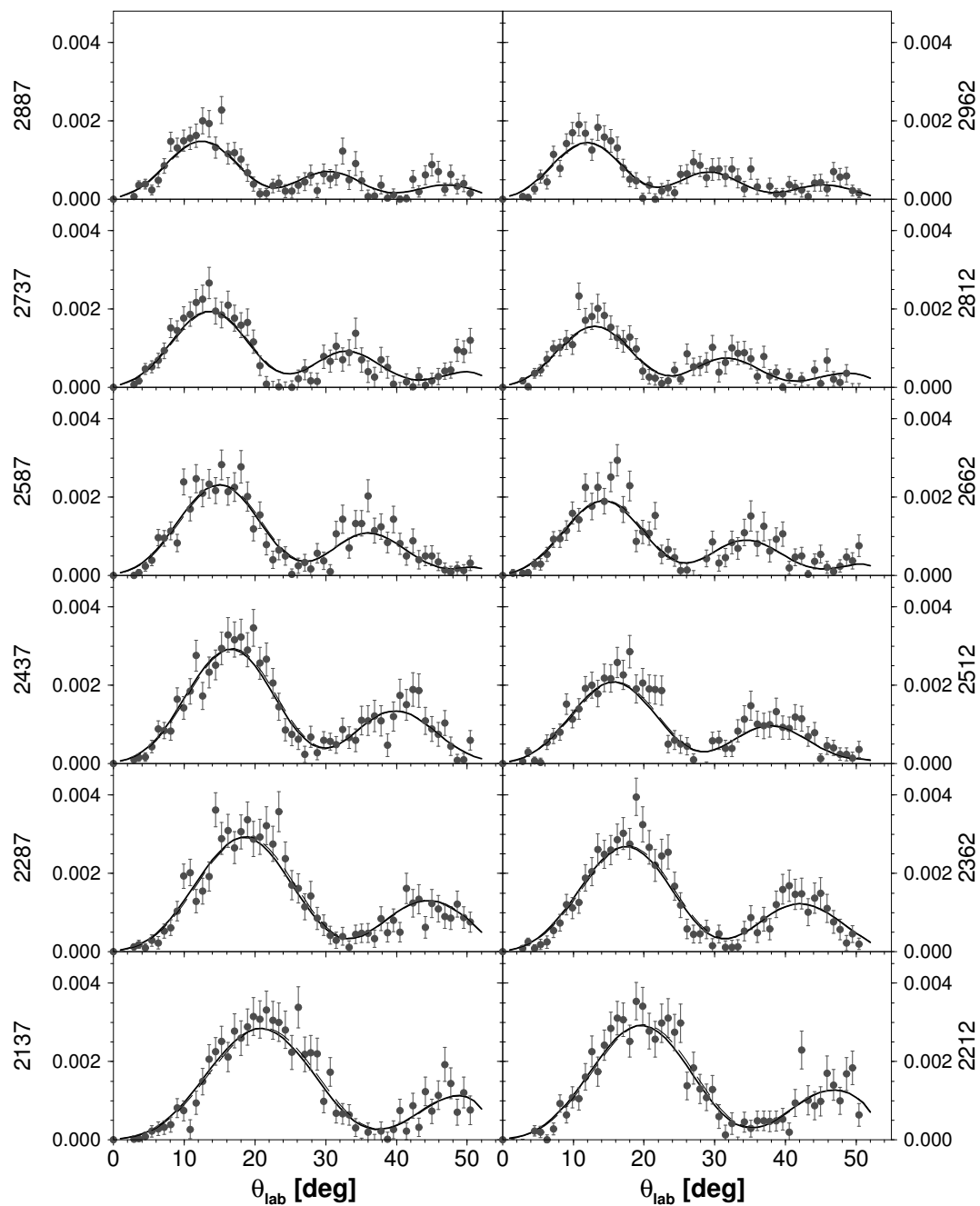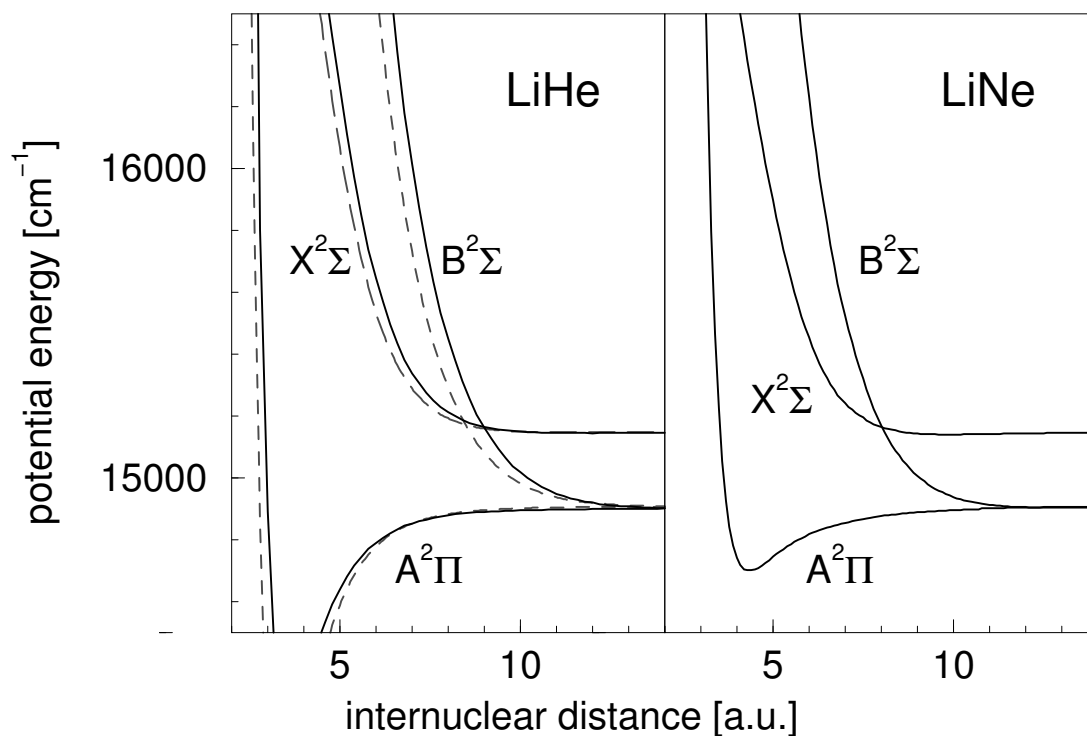
Figure 3.5: *The molecular potentials for the ground and first excited states of LiHe and LiNe. Left side LiHe: solid lines [18], dashed lines [19]; right side LiNe [20]. The excitation photon energy of 241.7 cm^{-1} is added to the X $^2\Sigma$-states.*

Li(2p)-state. The fine structure split between Li(2p$_{1/2}$) and Li(2p$_{3/2}$) is to small to be resolved.

The differential cross sections show interference structures. The number of oscillations per scattering angle decreases with decreasing velocity. For the high velocities of Li-He the signal disappears appart from noise due to the error statistics for big scattering angles, these angles are classical forbidden due to kinematic considerations.

In figure 3.5 calculated molecular potentials for LiHe by Staemmler et al. [18] (solid lines) and by Czuchaj [19] (dashed lines) (left graph) and for LiNe by Kerner [20] (right graph) are shown. The photon energy is added to the ground state potential for both collision pairs. The solid lines in figures 3.1 - 3.2 and 3.3 - 3.4 represent the theoretical determined cross sections based on the Staemmler and Kerner potentials. The theoretical results are for both collisional systems in very good agreement with the experimental data.

The oscillatory structures form a sensitive probe of the potential curves [13] in the range between the Condon radii (LiHe: 9 a.u., LiNe: 8 a.u.) and the inner turning points (5 - 6 a.u.) of the particles. In order to probe the accuracy of the underlying potentials trial corrections to the X $^2\Sigma$ and B $^2\Sigma$ potentials are done in a range from 4 to 10 a.u. Outside of this domain their shape is not modified. The corrections are constructed in

Corrections to the LiHe and LiNe potentials					
	X $^2\Sigma$	error	position	B $^2\Sigma$	error	position
LiHe	+5.8 cm^{-1}	$\pm$ 8 cm^{-1}	6.0 a.u.	-0.5 cm^{-1}	$\pm$ 14 cm^{-1}	7.0 a.u.
LiNe	-1.4 cm^{-1}	$\pm$ 4 cm^{-1}	6.0 a.u.	+3.0 cm^{-1}	$\pm$ 9 cm^{-1}	7.0 a.u.

Table 3.1: Maxima of the calculated correction function of the LiHe and LiHe potentials with the belonging errors and sampling point positions.

the form of Hermitian spline functions. The variation is done at given sampling points at 4, 6 and 10 a.u. for the X $^2\Sigma$ and 4, 7 and 10 a.u for the B $^2\Sigma$ potentials. The maxima are at 6 and 7 a.u. respectively. Only the amplitude of the correction functions is modified, their form is not varied. A least-squares-procedure [13] is used to find the best agreement between the experimental and the theoretical cross sections. The cross sections of 20 different velocities classes are used for the fits of LiHe and LiNe. This leads to the in table 3.1 quoted corrections to the potential curves. The errors estimation includes the experimental uncertainties (table 2.10) and the statistical error of the fit. The calculated variations of the potentials and the corresponding differential cross section are not shown in the figures 3.5 and 3.1 - 3.4 because the small deviations would be hardly visible.

The sensitivities for the X $^2\Sigma$ and B $^2\Sigma$ curves are comparable. Due to the fact that the underlying experimental data sets are for only one detuning, the corrections are given in a fixed form. This is in contrast to [13] where a large data set for the collision pair KAr with different detunings is much more sensitive to the detailed form of the potential curves and allow to improve the given calculated potentials. The results for LiHe and LiNe show that the presented experimental data still confirm an accuracy in the order of 10 cm^{-1} of the calculated potentials. However, this does not mean that there are no existing other potentials out of the described accuracy range.

The dashed lines in figures 3.1 and 3.2 are cross sections calculated with an older underlying LiHe potential by Czuchaj [19] the accordance is slightly worse. The positions of the 2. maxima deviate up to 4° from the experimental ones. One would expect a bigger variation in the cross section because the variation in the potential curves rises up to 500 cm^{-1} for the B $^2\Sigma$ curve and up to 200 cm^{-1} for the X $^2\Sigma$ potential curve in the relevant internuclear distance range. The described method is more sensitive to the difference between the relevant potential curves and their shape than to the potentials itself. The relevant potential curves for LiHe have nearly the same shape, they proceed almost parallel. The sensitivity rises also with the number of oscillations per scattering angle, which is small for the used detuning. These arguments might be an explanation for the small aberrations in the differential cross sections and show up the borders of the described method.
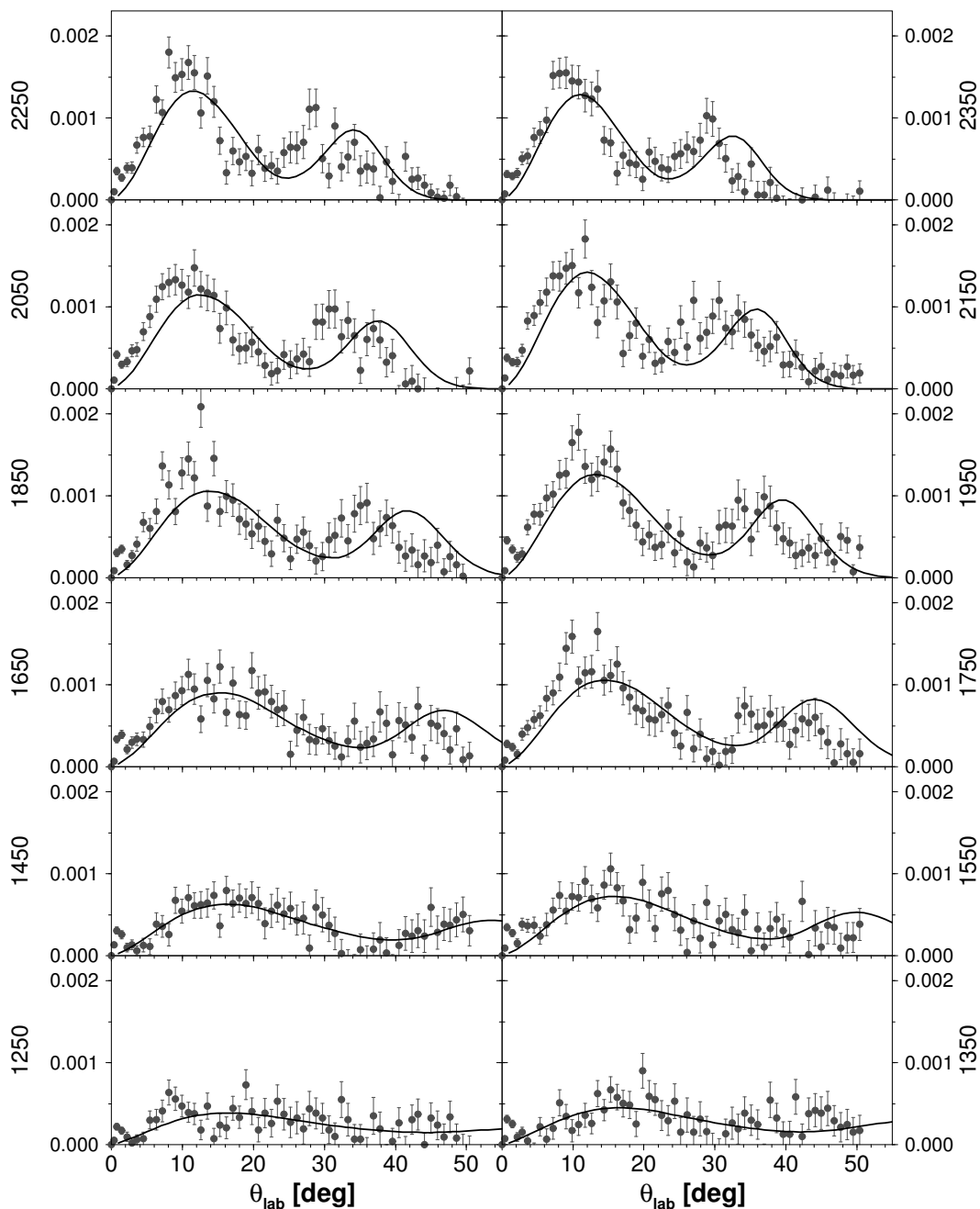
3.2.2 LiH$_2$ and LiD$_2$

Figure 3.6: *Differential cross sections of LiH$_2$ as a function of the laboratory scattering angle θ multiplied by sin(θ) for different velocities. The vertical numbers at the left (left column) and right (right column) sides of the graphs indicate the appropriate velocity of the lithium after the collision in m/s. The detuning is 241.7 cm^{-1}. Circles: Experimental data. Curves: Theory.*

Figure 3.7: *Differential cross sections of LiH$_2$ as a function of the laboratory scattering angle θ multiplied by sin(θ) for different velocities. The vertical numbers at the left (left column) and right (right column) sides of the graphs indicate the appropriate velocity of the lithium after the collision in m/s. The detuning is 241.7 cm^{-1}. Circles: Experimental data. Curves: Theory.*

57
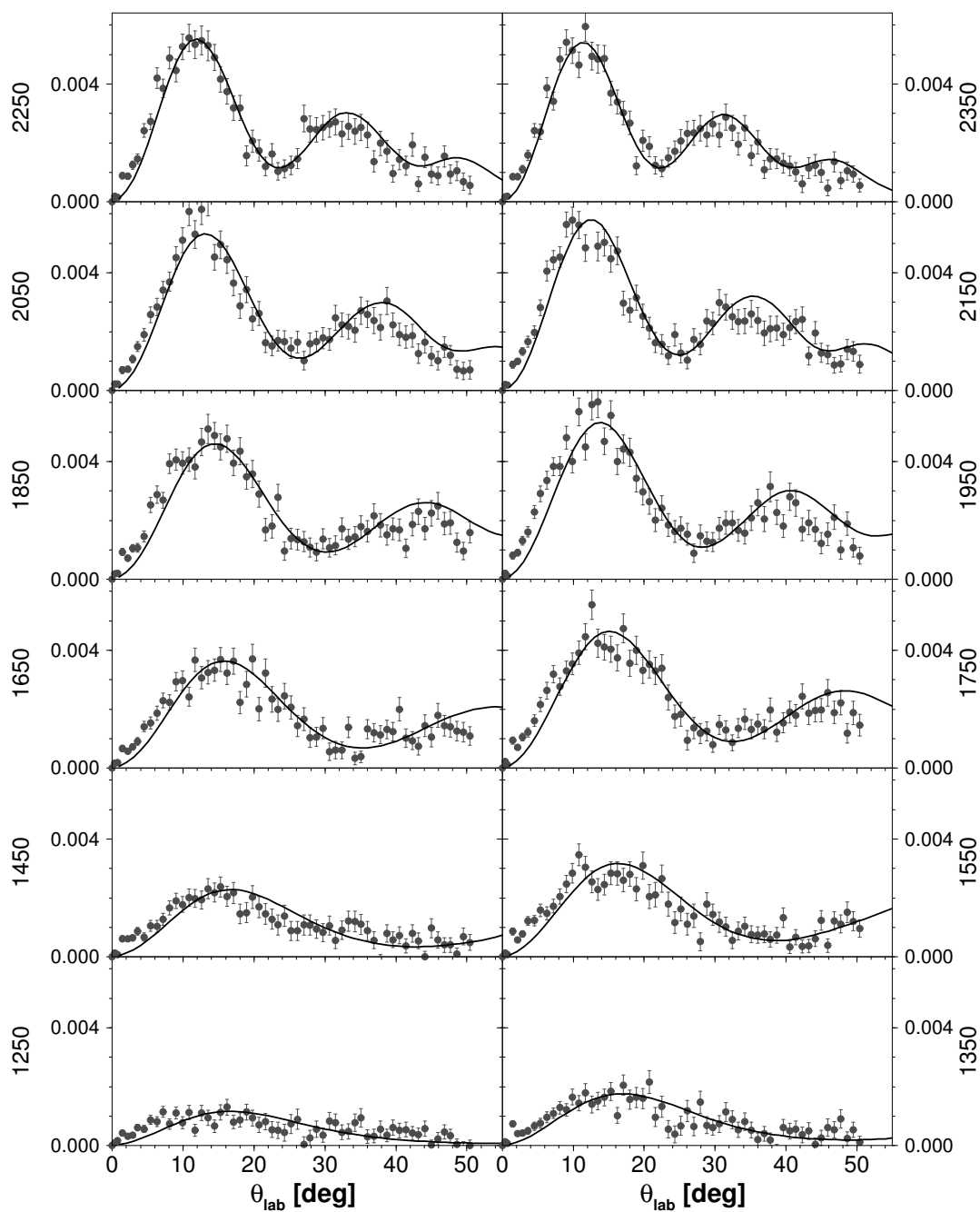
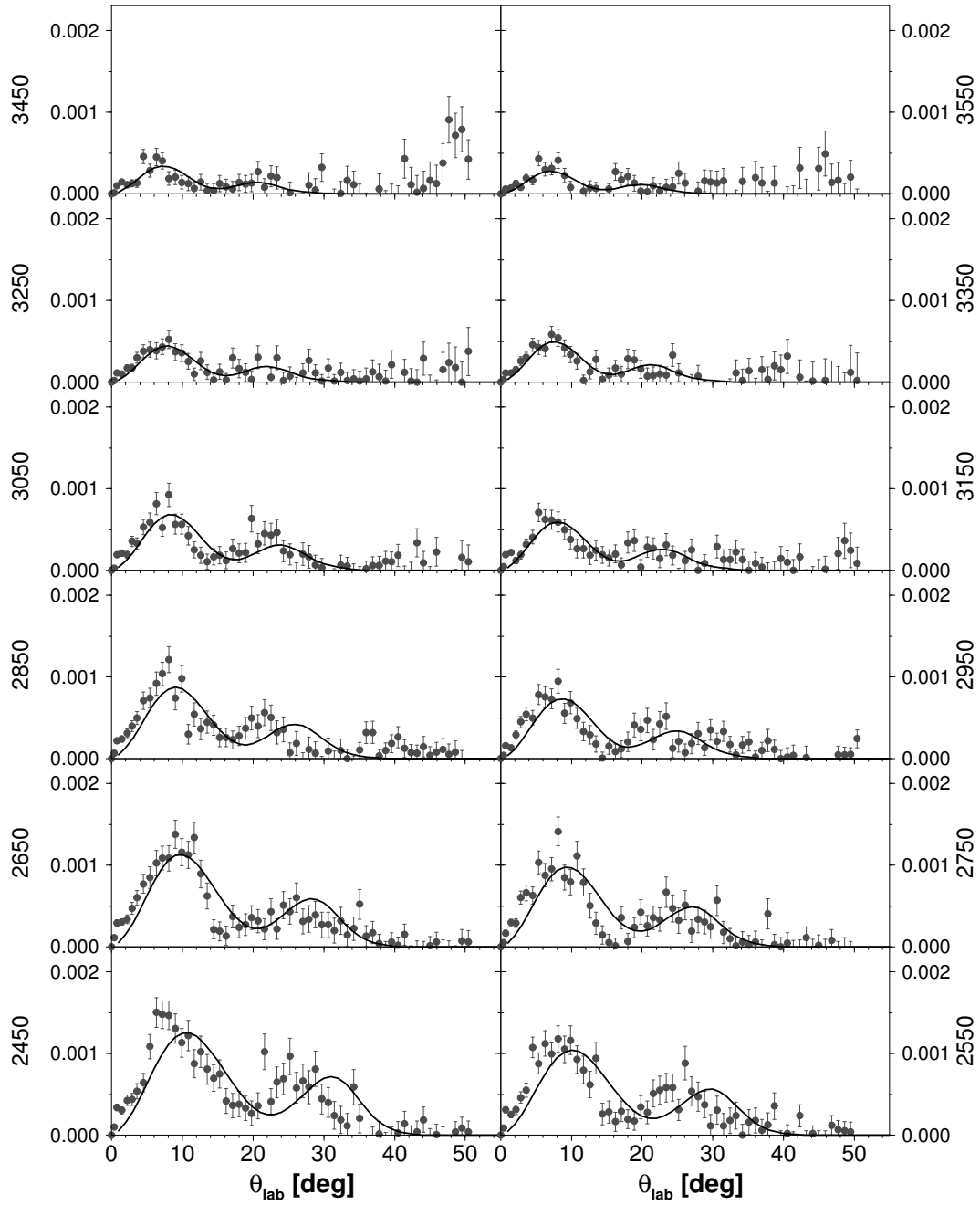Figure 3.8: *Differential cross sections of LiD$_2$ as a function of the laboratory scattering angle θ multiplied by sin(θ) for different velocities. The vertical numbers at the left (left column) and right (right column) sides of the graphs indicate the appropriate velocity of the lithium after the collision in m/s. The detuning is 241.7 cm^{-1}. Circles: Experimental data. Curves: Theory.*

Figure 3.9: *Differential cross sections of LiD$_2$ as a function of the laboratory scattering angle θ multiplied by sin(θ) for different velocities. The vertical numbers at the left (left column) and right (right column) sides of the graphs indicate the appropriate velocity of the lithium after the collision in m/s. The detuning is 241.7 cm^{-1}. Circles: Experimental data. Curves: Theory.*

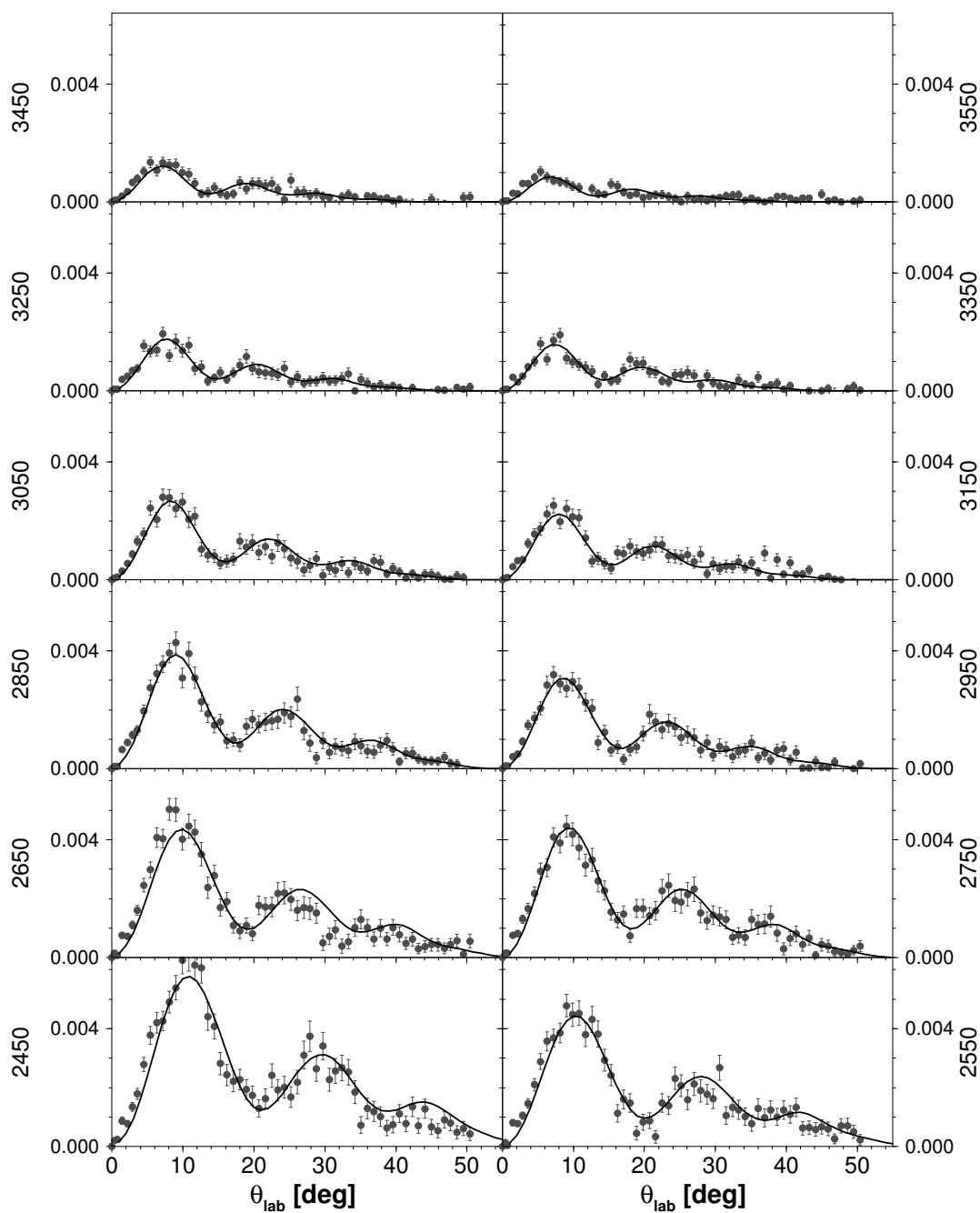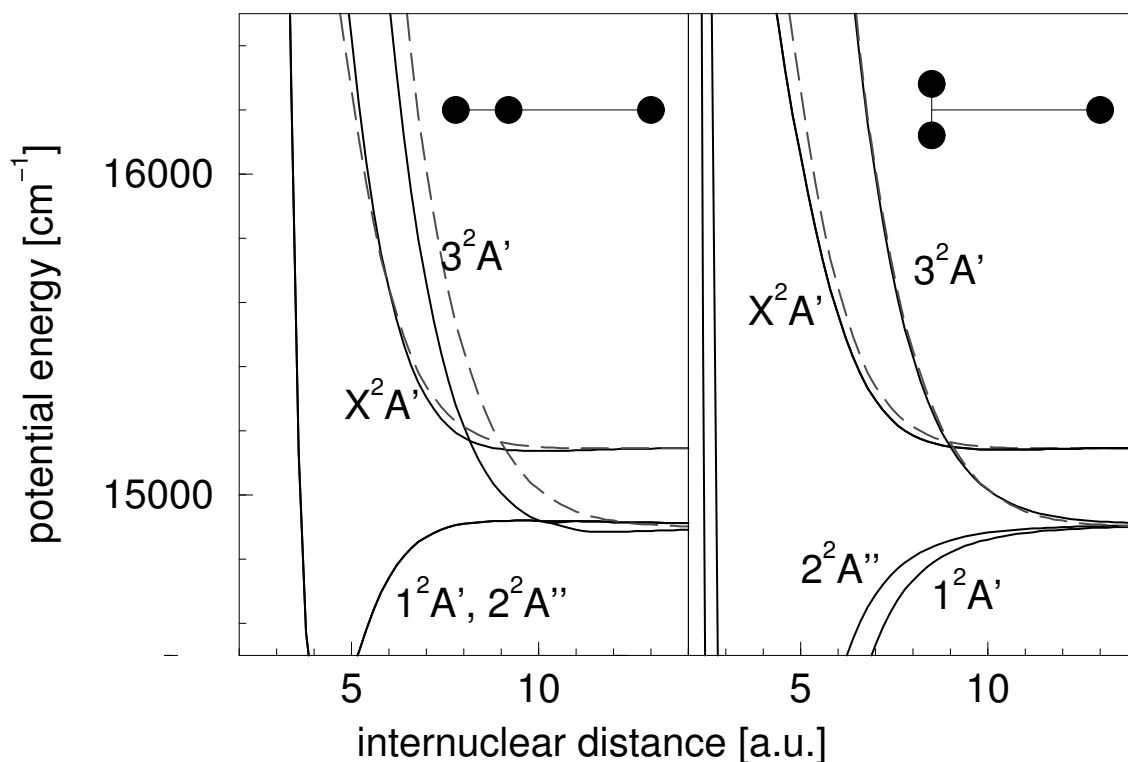Figure 3.10: *The molecular potentials for the ground and first excited states of LiH$_2$ (LiD$_2$) [40]. The excitation photon energy of 241.7 cm^{-1} is added to the 3 ^{2}A'-states. The left graph refers to the collinear and the right to the T-shaped geometry as indicated with the icons. The dashed lines correspond to the B $^2\Sigma$ and the shifted X $^2\Sigma$ potential curves of LiHe [18] as labeled in figure 3.5.*

The experimental conditions for LiH$_2$ and LiD$_2$ are the same as described for LiHe in subsection 3.2.1.

The experimental determined cross sections for both collision pairs are presented in figures 3.6 - 3.9. The shapes of the experimental determined cross sections are quite astonishing. They show clear oscillatory structures. This is a well-known feature for atomic targets (section 1 and e.g. [46]). For molecular targets like N$_2$, O$_2$, C$_2$, CO and CO$_2$ the observed differential cross sections are usually simply decreasing to higher scattering angles (see [63]).

In figure 3.10 calculated LiH$_2$ [40] potentials (solid lines) are shown. In order to calculate the LiH$_2$ surfaces the H atoms are kept at their equilibrium distance. The figure shows cuts for $\alpha = 0°$ (collinear geometry) and 90° (T-shaped geometry), where α is the angle between the H$_2$ axis and the direction of the connecting line between the center of the H$_2$ molecule and the Li atom. The surfaces apply for LiD$_2$, too. The dashed lines represent the LiHe potential curves calculated by Staemmler [18]. The photon energy is added to the ground state potential for all collision pairs.
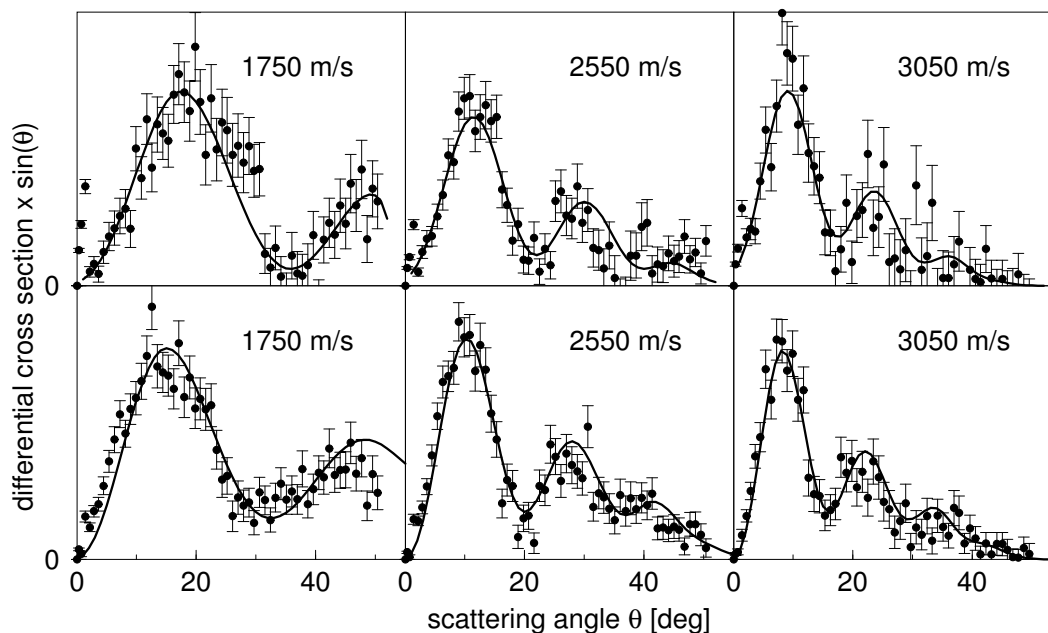
Figure 3.11: *Li detuning: 241.7 cm^{-1} : rows: Differential cross sections of LiHe (top row) and LiD$_2$ (bottom row) as a function of the laboratory scattering angle θ multiplied by sin(θ). The columns refer to different Li velocities after the collision as indicated in the graphs. The detuning is 241.7 cm^{-1}. Circles: Experimental results, the error bars indicate one standard deviation. Lines: Theoretical results calculated with the potentials shown in the figures 3.5, 3.10.*

The cross sections for the LiH$_2$ and LiD$_2$ collision pairs are calculated by a rotational sudden approach (e.g. [45]). The distance between lithium atom and the H$_2$ molecule and the D$_2$ molecule respectively varies during the collision, but the angle α is kept fixed, suppressing the angular variation of the potential surface due to the molecular rotation. The interference pattern of the cross sections is governed by the phase difference, which primarily depends on the shape of the potentials inside the Condon radius. Even for an overestimated rotational temperature of 100 K the variation of α during the crucial part of the collision is only 20°. This variation is determined by classical trajectory calculations described in [81]. The amount of the variation of α is small enough to be negligible for a first approximation. The cross sections are calculated for seven angles α (0°, 15°, 30° , 45°, 60° , 75°, 90°). The oscillatory structures vary considerably with the value of α. The number of oscillations per scattering angle rises to higher values of α. Geometrical reasons lead to the fact that angles near $\alpha = 90°$ (T-shaped geometry) are more likely than smaller angles especially near $\alpha = 0°$ (collinear geometry), so the final cross section is built as an average over α, with a geometric weight factor sin(α). Due to the weight factor the resulting positions of the maxima of this average cross section are very close to the ones of the T-shaped geometry. The calculated cross sections of figures 3.6 - 3.9 are in good agreement with

the experimental data. The experiences with atomic collision pairs allow to estimate necessary corrections of the shape of the calculated potentials in the order of 50 cm^{-}1. It attracts attention that the interference maxima of the LiD$_2$ cross sections are at nearly the same scattering angles as those of LiHe, even the shape of the oscillation structures is very alike (figure 3.11). As the experimental conditions are comparable, the target masses are identical and the target velocities are similar, this gives a hint for a corresponding similarity of the centre-of-mass cross sections and so of the underlying interaction potentials. The dashed lines in figure 3.10 represent the X $^2\Sigma$ and the B $^2\Sigma$ potential curves of LiHe [18]. The LiHe ground state potential is very close to the LiH$_2$ (LiD$_2$) ground state potential. This holds over the whole internuclear distances which are probed here. The B $^2\Sigma$ and the 3 ^{2}A$'$ potential curves are for the T-shape geometry nearly identical and for the collinear geometry the form is alike, too. This confirms the expected affinity of the relvant LiHe and LiH$_2$ potentials.

3.2.3 NaNe

The optical collision pair NaNe is well analyzed for positive detuning [12, 51]. In this work NaNe is investigated for the first time with a negative detuned excitation laser. The detuning is - 299.7 cm^{-1} in respect to the Na(3s - 3p$_{1/2}$) resonance. The detection transition is: Na(3p$_{3/2}$) $\rightarrow$ Na(34d). Cross sections for 5 velocity classes and 6 different polarizations of the excitation laser were measured and are shown in figure 3.12. The columns correspond to the different velocity classes. The width of the velocity classes is 200 m/s. The medial velocity is labeled at the left side of the columns. The rows represent the polarizations with respect to the sodium beam direction as labeled on bottom of the rows. The error bars denote $\pm$ one standard deviation of the counting statistics. The wide variety of different interference structures will be discussed qualitatively in the next section 3.3.1.

The solid lines represent the theoretical cross sections. They rely on quantum chemical determined potentials [20], which are diagrammed as solid lines in figure 3.13. The dashed lines are cross sections based on the spectroscopically determined A$^2\Pi$ potential from [21] which is shown as dashed line in figure 3.13. The agreement between experimental and quantum chemical cross sections is excellent for all velocities and polarizations. The cross section relying on spectroscopical data seriously disagree with the experiment.

The accuracy of the quantum chemical potential seems to be very good. The spectroscopical determined potentials are wrong. In order to decide if the different depths of the quantum chemical and spectroscopic A$^2\Pi$ minima or the discrepancy in the repulsive A$^2\Pi$ branches have caused the disagreement with the experiment, the effect of trial modifications (section 3.2.1) to the quantum chemical potentials is investigated. The agreement between experimental and calculated cross sections is still good if modifications in the order of 30 cm^{-1} are added to the X$^2\Sigma$ potential curve. An analogue
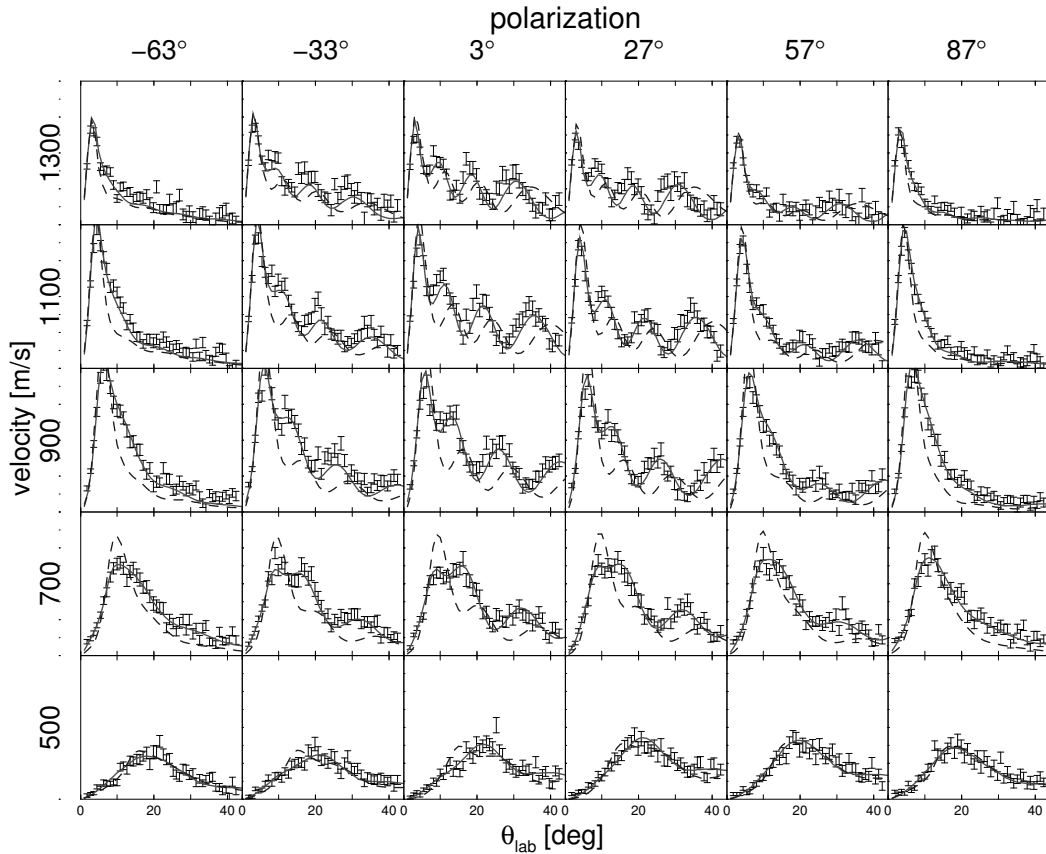
Figure 3.12: *NaNe detuning: -299.7 cm^{-1} : Differential cross sections of NaNe as a function of the laboratory scattering angle θ multiplied by sin(θ). The columns belong to different polarization directions of the excitation laser with respect to the Na beam direction (left column to right column: -63°, -33°, -3°, +27°, +57°, +87°). The rows belong to different velocities of the sodium after the collision (top to bottom: 1300 m/s, 1100 m/s, 900 m/s, 700 m/s, 500 m/s). The detuning is -299.7 cm^{-1}. Circles: experimental data. Solid lines: theory with the potentials from [20]. Dashed lines: theory with the spectroscopical determined A$^2\Pi$ potentials from [21].*

modification of the repulsive branch of the A$^2\Pi$ curve has no destinct influence either. If the A$^2\Pi$ potential is modificated 30 cm^{-1} near the minimum the resulting cross sections show a significant disagreement to the experimental ones, similar to the cross sections calculated on the base of the spectroscopical determined potentials.

This leads to the conclusion that the scattering data is particulary sensitive to the attractive part of the A$^2\Pi$ curve, and that the spectroscopic data certainly underrate the depth of the minimum. In difference to the in subsection 3.2.1 and [13] described applications where the cross section data is found to be equally sensitive to the repulsive ground and excited state potential curves, it seems that for the used experimental conditions the sensitivity to the attractive A$^2\Pi$ curve is much higher than to the repulsive X$^2\Sigma$ curve.
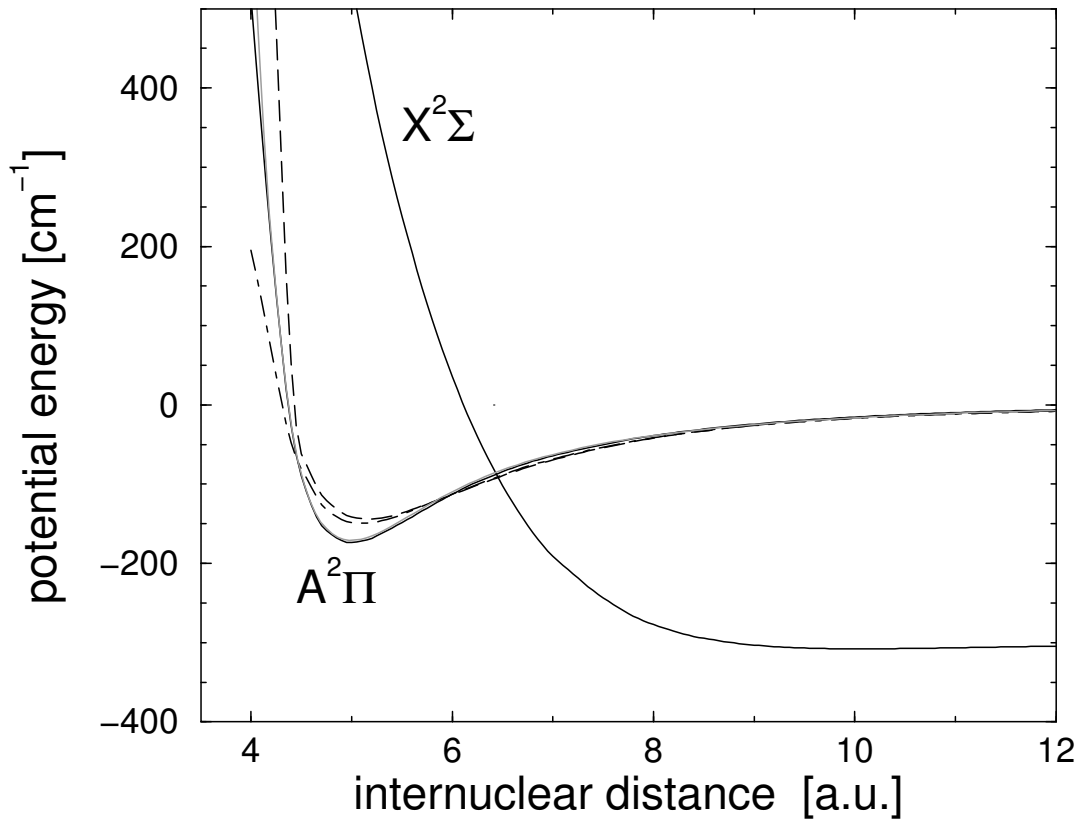
Figure 3.13: *The NaNe potentials. Solid lines: quantum chemical $X^2\Sigma$ and $A^2\Pi$ potentials [20]. Dashed and dot-dashed: spectroscopic $A^2\Pi$ potentials according to [21, 82]. The energy of the excitation photon of -299.7 cm^{-1} is added to the ground state curve.*

3.3 Observation and manipulation of atomic collisions by laser polarization

3.3.1 Observation

Former applications [83] have shown the possibility to extract all the classical geometrical information of the collision from the experimental data, because it is stored in the interference structure. This is comparable to optical holography, where an image is reconstructed from an interference pattern. The described application was done for positive detuning and two Condon vectors. The presented measurements for NaNe should

Figure 3.14: *NaNe detuning: -299.7 cm^{-1}, the Na velocity after the collision is 1100 m/s. Left column: Differential cross sections for varying linear polarizations as a function of the laboratory scattering angle θ multiplied by sin(θ). Right column: Condon vectors and classical trajectories for the laboratory scattering angle of 16 °. The size of the diagram is 16 × 16 a.u.. The dashed lines represent the polarization direction used in the experiment. The numbers are the angles between the polarization and the Na beam direction.*

Figure 3.15: *NaNe detuning: -299.7 cm^{-1} the Na velocity after the collision is 700 m/s. Left column: Differential cross sections for varying linear polarizations as a function of the laboratory scattering angle θ multiplied by sin(θ). Right column: Condon vectors and classical trajectories for the laboratory scattering angle of 16 °. The size of the diagram is 20 × 20 a.u.. The dashed lines represent the polarization direction used in the experiment. The numbers are the angles between the polarization and the Na beam direction.*

be used to determine the collisonal geometry of optical collisions with negative detuning. However, the appearance of up to four Condon vectors makes the analysis more complicated and demands further development of the fitting procedure described in [83].

The experimental and theoretical data of NaNe described in section 3.2.3 is now used to understand the collision geometry and effects of the variation of the polarization of the excitation laser qualitatively.

In figure 3.12 can be seen that the oscillatory structure in the differential cross sections seriously depend on the polarization of the excitation laser, for some polarizations the oscillations even vanish. There is also an evolution from high regularity to reduced regularity of the oscillatory structure from higher to lower velocity.

To better explain these effects the graphs for two velocity classes (700 m/s, 1100 m/s) are enlarged and diagrammed in the left columns of the figures 3.14 and 3.15. The right columns illustrate the classical trajectories for the relative motion with the Condon vectors and the polarization (dashed line) calculated for a laboratory scattering angle of 16 degree. The illustration is analog to figure 1.10.

As explained in section 1.2.2 the oscillatory structure in the differential cross section undergoes a strong variation with varying polarization. In the present case of a Σ - Π the transition dipole moment $\mathbf{d}$ is orthogonal to the Condon vectors $\mathbf{r}_i$ (section 1.1.1). For 1100 m/s the maximum signal with the highest contrast appears at -3° where $\mathbf{E}$ is nearly orthogonal to both of the Condon vectors. The contrast is getting smaller until the oscillatory structure vanishes for the polarization of -63° and 87°. In these cases $\mathbf{E}$ is nearly parallel to one of the Condon vectors. With further turning of the polarization the contrast is rising until it reaches its maximum again.

Strongly attractive trajectories occur at low velocities (section 1.2.1) as can be seen in the graphs for 700 m/s. Now four trajectories contribute to the signal leading to a lower regularity in the interference structure. The distance between the maxima and the contrast varies within the data for one polarization. Even for four Condon vectors the oscillatory structure vanishes for a polarization of 87°. One explanation might be that the relative weights of the repulsive trajectories are in this case higher than the weights of the attractive trajectories and so the dominant contributions to the signal are nearly switched-off. Also it has to be taken into account that some of the resulting oscillations have a very small distance from maximum to maximum and are not resolved under the conditions of the experiment [46].

3.3.2 Coherent control

The in section 1.2.2 described possibility to have complete control over the interference pattern of an optical collision should be demonstrated. It is planned to observe an continuous shift of an interference pattern by the right choice of the control parameter δ (equations 1.21 and 1.22). For this task differential cross sections of the NaNe
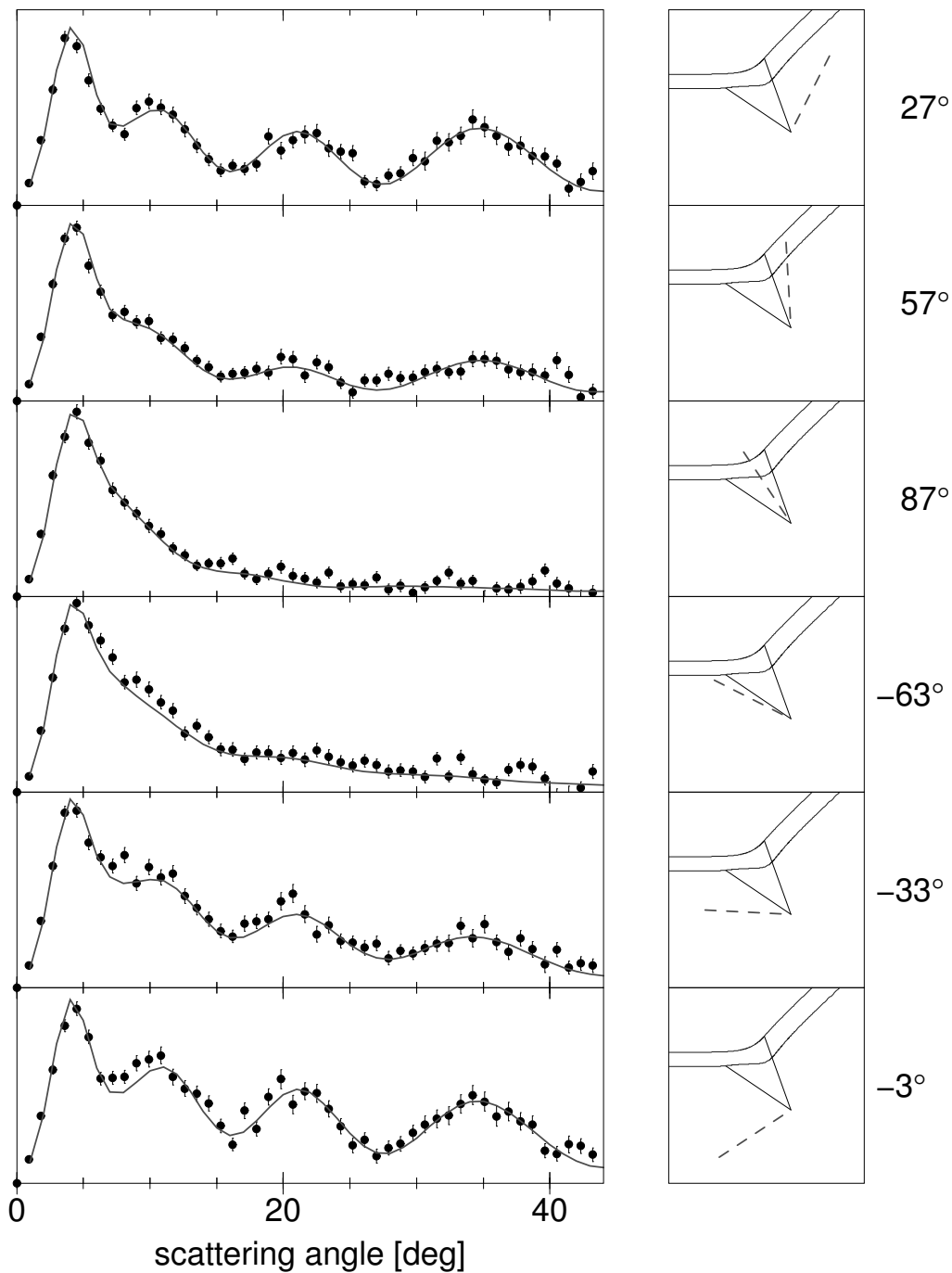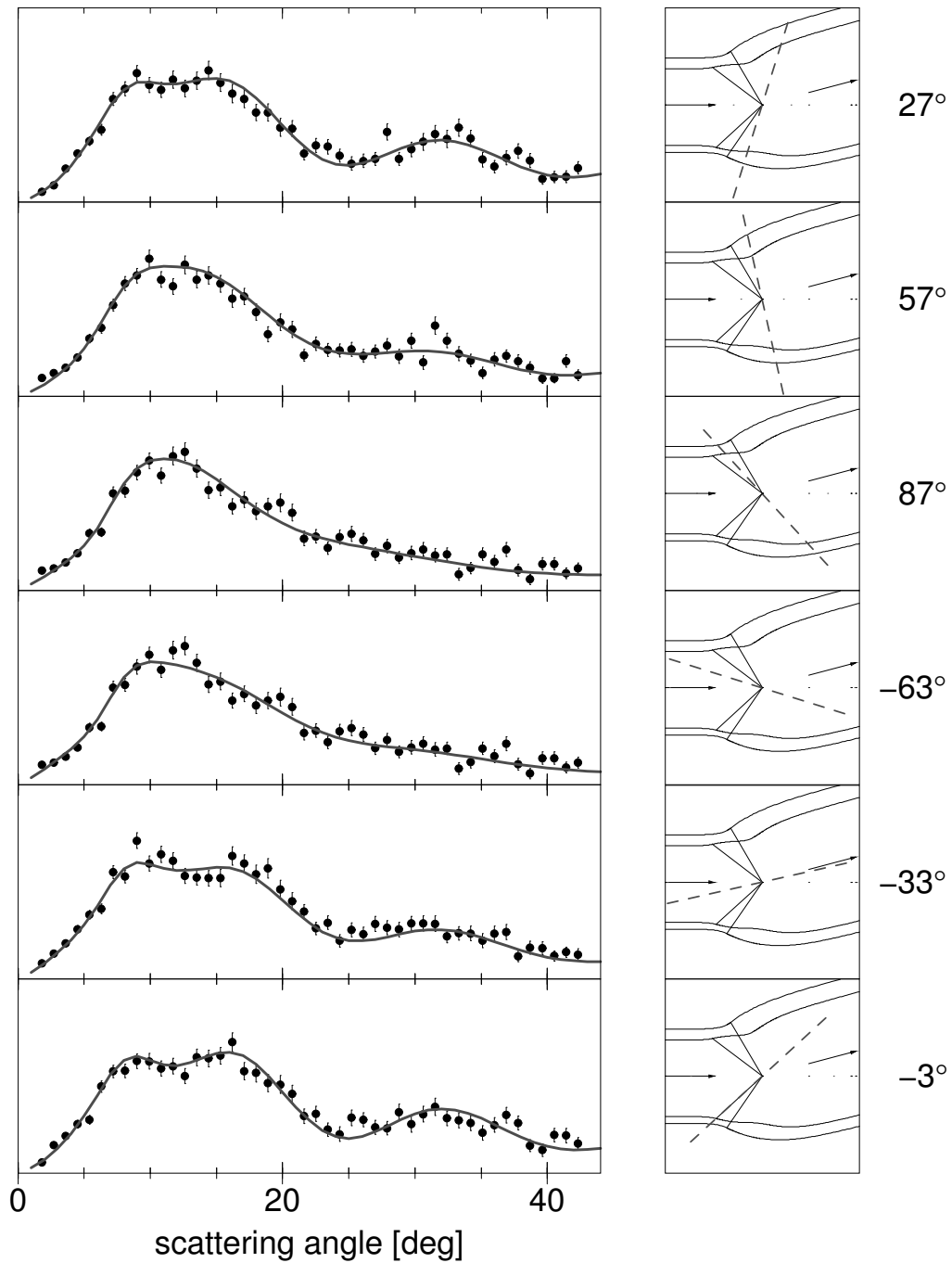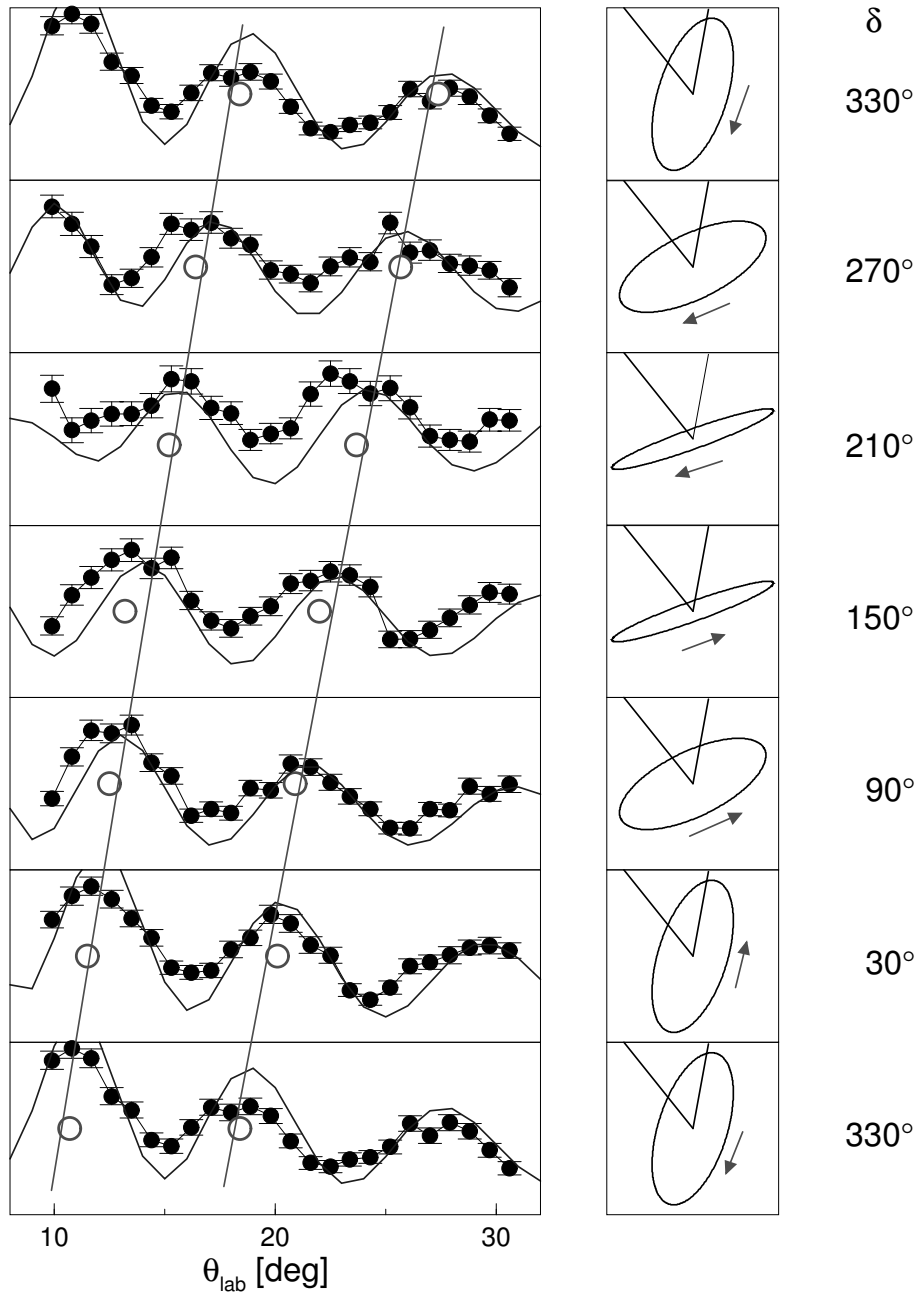
Figure 3.16: *NaNe: detuning: 120 cm^{-1}; the Na velocity after the collision is 1225 m/s. Left column: differential cross sections as a function of the laboratory scattering angle θ multiplied by sin(θ). The vertical scales of the graphs are different. Filled circles: experimental results, the error bars indicate one standard deviation. Curves: theoretical results calculated with the potentials shown in figure 3.13. The large hollow circles are the positions of the maxima. The straight lines crossing the graphs are a help to guide the eye. Right column: The elliptic polarization, the Condon vectors and the resulting value of the control parameter δ.*

system are examined. The detuning is 120 cm^{-1} in respect to the Na(3s - 3p$_{1/2}$) resonance. The detection transition is: Na(3p$_{3/2}$) $\rightarrow$ Na(34d). Cross sections were measured for scattering angles between 9.9° and 30.6°, 6 different control parameters δ (30°, 90°, 150°, 210°, 270°, 330°) and for 3 velocity classes (1075 m/s, 1225 m/s, 1375 m/s). The width of the velocity classes is 150 m/s. The control parameters are calculated for a sodium velocity after the collision of 1225 m/s and a laboratory scattering angle of 21.6° (reference conditions). The appropriate elliptical polarizations valid strictly speaking just for this scattering angle and velocity, however, the error made by this approximation is small. All relevant calculations regarding this approximation and possible sources of error are described in [55].

In the left row of figure 3.16 the differential cross sections for 1225 m/s are presented. The vertical scales are different in order to emphasize the continuous shift of the interference pattern. The top graph is repeated at the bottom. The positions of the experimental maxima are marked by hollow circles. The straight lines are for guiding the eye. The columns correspond to the different control parameters δ, their values are labeled to the right. The right row shows the appropriate elliptical polarizations of the excitation laser in respect to the Condon vectors for a scattering angle of 21.6 °. Looking along the straight lines which connect the graphs it is easily seen that the whole interference pattern is continuously shifted to higher scattering angles for a rising control parameter. For example in the graphs of $\delta = 150°$ and $\delta = 330°$ the angular positions of the maxima and minima have changed due to the phase difference $\Delta\delta$ of 180°. The solid lines in the graphs represent the theoretical cross sections. The agreement between calculated and experimental data is good, especially the positions of the theoretical and experimental determined interference maxima fit very good.

In figure 3.17 the graphs for all three velocity classes are shown. The rows correspond to the different velocity classes and the columns represent the different elliptical polarizations as introduced in figure 3.16. The corresponding control parameters δ are labeled to the right of each column. The solid lines represent the theoretical cross sections. All graphs have the same scale. The experimental cross sections for the other velocity classes (1075 m/s and 1375 m/s) show a shifting of the interference pattern, too. The agreement between calculated and experimental data is good. In figure 3.17 the quantitative agreement between experimental and theoretical data is very good for $\delta = 150°$, 210° and 270° and good for 90°. The contrast in the theoretical determined cross sections for $\delta = 30°$ and 330° is larger than the contrast of the experimental data. This might come from some broadening mechanisms not fully taken into account in the convolution scheme [55]. The qualitative agreement is for all measurements very good.

Figure 3.18 illustrates the positions of the maxima of the experimental (filled circles) and theoretical (diamonds) differential cross sections of figure 3.17 as function of the control parameter δ. The three graphs belong to the velocity classes as labeled at their top. The angular position of the interference maxima clearly move linearly with the control parameter for all velocities. The linear fits are the dashed lines. For the reference velocity (1225 m/s) the deviations from linearity are in the order of $\pm 0.3°$. The
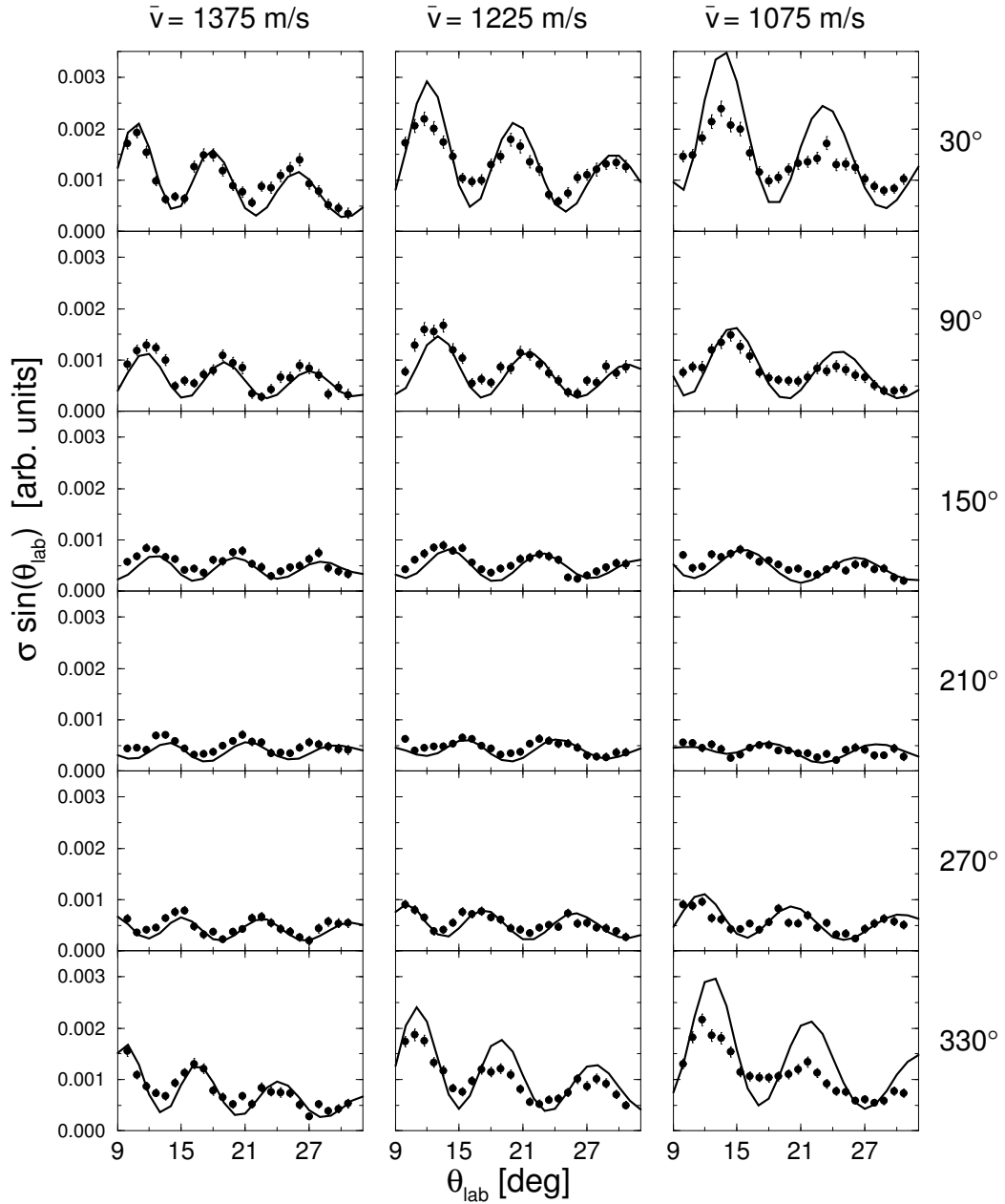
Figure 3.17: *NaNe detuning: 120 cm^{-1} : Differential cross sections of NaNe as a function of the laboratory scattering angle θ multiplied by sin(θ). The detuning is 120 cm^{-1}. The columns belong to different Na velocities after the collision as labeled at the top and the rows to different elliptical polarizations of the excitation laser. The numbers to the right indicate the appropriate control parameter δ. Circles: experimental results, the error bars indicate one standard deviation. Lines: theoretical results, calculated with the potentials by [20].*
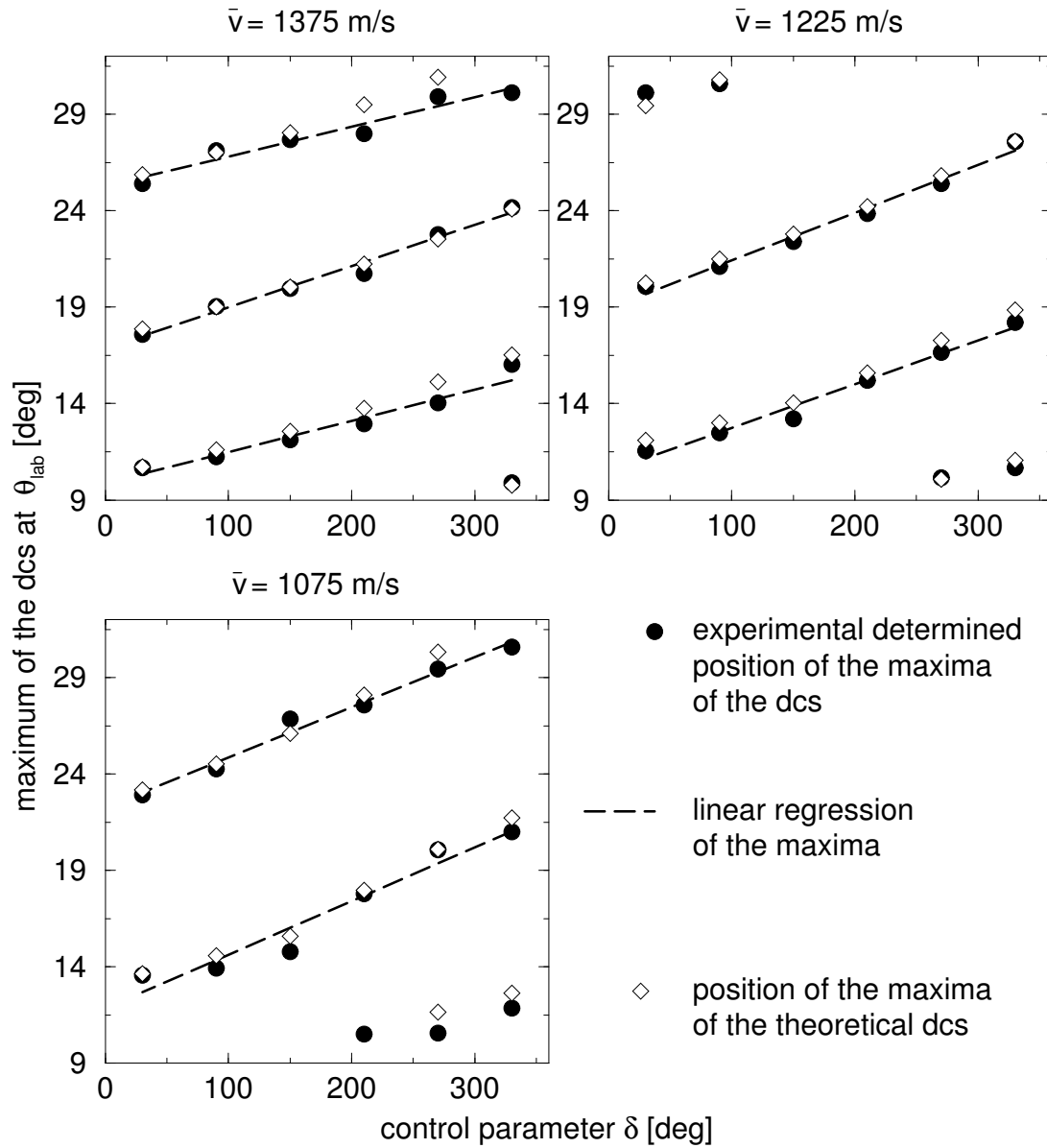
Figure 3.18: Positions of the maxima of the differential cross sections from figure 3.17 (circles: experimental determined; diamonds: theory) as a function of the control parameter δ. The different graphs belong to different Na velocities after the collision (1375 m/s, 1225 m/s and 1075 m/s). The dashed lines are linear fits to the experimental positions of the maxima

theoretical determined positions of the maxima typically deviate less than $0.5°$ from the experimental determined ones. For the other velocities the deviations are slightly bigger which might caused by the error in the determination of the control parameter. The by the choice of the control parameter planned linear shift of the interference fringes is impressively performed. The described experiment demonstrate the total control of an atom-atom collision. The control is complete because any desired angular position and contrast of the interference pattern can be adjusted. However, the finite resolution of the experimental apperatus limits the possible values of the contrast.

Summary

The optical excitation of alkali-atom and alkali-molecule collision pairs was investigated in a crossed beam experiment with differential detection. The exciting light was used to study and to manipulate the collision event.

Collisional systems with Li as projectile atom were examined for the first time with this method. The accuracies of the repulsive parts of the ab initio calculated LiHe and LiNe X $^2\Sigma$ and B $^2\Sigma$ potentials were probed investigating the interference structure of the optical collision cross sections. The experimental and theoretical differential cross sections are in very good agreement for the LiHe and LiNe systems. The uncertainties of the repulsive parts of the calculated X $^2\Sigma$ and B $^2\Sigma$ potentials are estimated of the order of 10 cm^{-1}. The present analysis probes the overall behavior of the potential curves. In order to get a better insight in the details of their form an analysis of a set of differential cross sections for different detunings is desirable.

The differential cross sections of the LiH$_2$ and LiD$_2$ systems also show, quite surprisingly, an oscillatory structure. The agreement between experimental and theoretical data is good. This legitimates the theoretical description of the collision by a rotational sudden method, where the alignment of the target molecule is frozen during the collision. Taken into account the experiences with atomic systems the good agreement also points to an accordant accuracy of the two repulsive $^2A'$ potentials like for the LiHe and LiNe systems. Corrections in the order of 50 cm^{-1} seem to be a reasonable estimate.

The attractive part of the NaNe A $^2\Pi$ potential was investigated. The very good agreement between the experimental and theoretical cross sections calculated with recent quantum chemical potentials indicates a high accuracy of the underlying potentials. Previous spectroscopical data are found to underestimate the depth of the well of the A $^2\Pi$ potential.

The interference pattern of the differential cross section of the NaNe system for negative detuning show a strong dependency on the polarization of the exciting light. The oscillatory structure even vanish for some linear polarizations. The extraction of the geometric information of the collision, like Condon vectors and the relative weight of the corresponding trajectories is not managed, yet.

The control of an atom-atom collision is demonstrated for the NaNe system. By the right choice of the elliptical polarization, interference maxima of differential cross sections can be shifted to any angular position. Within the borders of a finite experimental resolution the contrast of the interference pattern can be given any value between 0 and 1. The exploitation of the polarization of the excitation laser light appears as a simple, powerful tool for the control of collisional processes.

Bibliography

[1] A. JABLONSKI: *General theory of pressure broadening of spectral lines.* Phys. Rev., 68(3-4):78–93, Aug 1945.

[2] R. E. M. HEDGES, D. L. DRUMMOND, and A. GALLAGHER: *Extreme-wing line broadening and Cs-inert-gas potentials.* Phys. Rev. A, 6(4):1519–1544, Oct 1972.

[3] K. BURNETT: *Collisional redistribution of radiation.* Phys. Rep., 118(6):339–401, 1985.

[4] W. BEHMENBURG, A. MAKONNEN, A. KAISER, F. REBENTROST, V. STAEMMLER, M. JUNGEN, G. PEACH, A. DEVDARIANI, S. TSERKOVNY, A. ZAGREBIN, and E. CZUCHAJ: *Optical transistions in excited alkali + rare-gas collision molecules and related interatomic potentials: Li* + He.* J. Phys. B: At. Mol. Opt. Phys., 29:3891, 1996.

[5] G. LINDENBLATT, H. WENZ, and W. BEHMENBURG: *Study of excitation transfer Li(3D → 3P) occuring in optical collisions with rare gas atoms experimentally.* Euro. Phys. J. D, 13:329, 2001.

[6] M. D. HARVEY: *Laser spectroscopy of the $3d^2\Delta \leftarrow 2p^2\Pi$ transition in molecular LiHe.* Phy. Rev. Lett., 48:1100–1103, 1982.

[7] M. D. HARVEY, F. T. DELAHANTY, L. L. VAHALA, and G. E. COPELAND: *Experimental fine-structure branching ratios for Na-rare-gas optical collisions.* Phy. Rev. A., 34:2758, 1986.

[8] J. GROSSER, D. GUNDELFINGER, A. MAETZING, and W. BEHMENBURG: *Laser-assisted collisions: Investigation of the optical collision process Na(3s)+Kr+hν to Na(3p)+Kr in a crossed beam experiment.* J. Phys. B: At. Mol. Opt. Phys., 27(14):367–373, 1994.

[9] J GROSSER, D HOHMEIER, and S KLOSE: *Differential cross sections for radiation assisted collisions between atoms.* J. Phys. B: At. Mol. Opt. Phys., 29:299–306, 1996.

[10] J. GROSSER, O. HOFFMANN, C. RAKETE, and F. REBENTROST: *Direct observation of the geometry of atom-atom and atom-molecule collisions*. J. Phys. Chem. A, 101:7627, 1997.

[11] J. GROSSER, O. HOFFMANN, and F. SCHULZE WISCHELER: *Direct observation of nondiabatic transistions in Na-rare-gas differential optical collisions*. J. Chem. Phys., 111(7):2853, 1999.

[12] J. GROSSER, O. HOFFMANN, and F. REBENTROST: *Accurate probing of the repulsive $X^2\Sigma$ and the $B^2\Sigma$ potentials of nane and naar by differential optical collision experiments*. J. Phys. B: At. Mol. Opt. Phys., 33:L577–L583, 2000.

[13] C. FIGL, J. GROSSER, O. HOFFMANN, and F. REBENTROST: *Repulsive KAr potentials from differential optical collisions*. J. Phys. B: At. Mol. Opt. Phys., 37:3369, 2004.

[14] C. FIGL, J. GROSSER, O. HOFFMANN, and F. REBENTROST: *Observation of asymptotically forbidden transitions in CaAr optical collisions*. Chem. Phys. Letters, 380:196, 2003.

[15] E. G. G. STUECKELBERG: *Theorie der unelastischen Stöße zwischen Atomen*. Helv. Phys. Acta, 5:369, 1932.

[16] R. BRUEHL, J. KAPETANAKIS, and D. ZIMMERMANN: *Determination of the Na-Kr interaction potential in the $X\Sigma$ and $A\Pi$ state by laser spectroscopy*. J. Chem. Phys., 94(9):5865–5874, 1991.

[17] C. J. LEE, M. D.HAVEY, and R. P.MEYER: *Laser spectroscopy of molecular LiHe: The $3d\,^2p\;^2\Pi$ transition*. Phys. Rev. A, 43(1):77–87, Jan 1991.

[18] T. GRYCUK, W. BEHMENBURG, and V. STAEMMLER: *Quantum calculation of the excitation spectra of Li^*He probing interaction potentials and dipole moments*. J. Phys. B: At. Mol. Opt. Phys., 34:245, 2001.

[19] E. CZUCHAJ: *private communication*.

[20] C. KERNER: *Definition von Rumpf-Polarisations-Potentialen für Edelgase über die Berechnung von Elektronenstreuphasen und Anwendung auf Alkali-Edelgas-Wechselwirkungspotentiale*. Doktorarbeit, Universität Kaiserslautern, Fachbereich Chemie, 1995.

[21] R. A. GOTTSCHO, R. AHMAD-BITAR, W. P. LAPATOVITCH, I. RENHORN, and D. E. PRITCHARD: *Global analysis of the NaNe excimer band systems: A molecule between hund's cases*. J. Chem. Phys., 75(6):2546–2559, 1981.

[22] P. BRUNER and M. SHAPIRO: *Control of unimolecular reactions using coherent light*. Chem. Phys. Lett, 126(6):541–546, 1986.

[23] S. A. RICE and M.ZHAO: *Optical Control of Molecular Dynamics*. Wiley, New York, 1999.

[24] R. S. JUDSON and H. RABITZ: *Teaching lasers to control molecules*. Phys. Rev. Lett., 68(10):1500–1503, 1992.

[25] T. BRIXNER and G. GERBER: *Quantum control of gas-phase and liquid-phase femtochemistry*. Chem. Phys. Chem., 4(5):418–438, 2003.

[26] D. ZEIDLER, D. PROCH, M. MOTZKUS, and T. HORNUNG: *Adaptive compression of tunable pulses from a non-collinear-type OPA to below 16 fs by feedback-controlled pulse shaping*. Appl. Phys. B: Lasers and Optics, 70(Supplement 1):125 – 131, 2000.

[27] C. WAN, M. GUPTA, J. S. BASKIN, Z. H. KIM, and A. H. ZEWAIL: *Caging phenomena in reactions: Femtosecond observation of coherent, collisional confinement*. J. Chem. Phys., 106(10):4353–4356, 1997.

[28] A. SANOV, S. NANDI, and W. C. LINEBERGER: *Transient solvent dynamics and incoherent control of photodissociation pathways in i2 cluster ions*. J. Chem. Phys., 108,(13):5155–5158, 1998.

[29] S. C. ZILIO, L. MARCASSA, S. MUNIZ, R. HOROWICZ, V. BAGNATO, R. NAPOLITANO, J. WEINER, and P. S. JULIENNE: *Polarization dependence of optical suppression in photoassociative ionization collisions in a sodium magneto-optic trap*. Phys. Rev. Lett., 76(12):2033–2036, 1996.

[30] S. R. MUNIZ, L. G. MARCASSA, R. NAPOLITANO, G. D. TELLES, J. WEINER, S. C. ZILIO, and V. S. BAGNATO: *Optical suppression of hyperfine-changing collisions in a sample of ultracold sodium atoms*. Phys. Rev. A, 55(6):4407–4411, 1997.

[31] P. BRUMER, K. BERGMANN, and M. SHAPIRO: *Identical collision partners in the coherent control of bimolecular reactions*. J. Chem. Phys., 113(6):2053–2055, 2000.

[32] M. D. HAVEY, D. V. KUPRIYANOV, and I. M. SOKOLOV: *Two-photon coherent control of atomic collisions by light with entangled polarization*. Phys. Rev. Lett., 84:3823–3826, 2000.

[33] D. V. KUPRIYANOV, I. M. SOKOLOV, and A. V. SLAVGORODSKII: *Polarization-sensitive coherent control of atomic collisions with nonclassical light*. Phys. Rev. A, 65(6):063412, 2002.

[34] J. GROSSER, O. HOFFMANN, and F. REBENTROST: *Collision photography: Imaging of ultrafast atomic processes*. Europhys. Lett., 58:209, 2002.

[35] T. Brixner, N. H. Damrauer, G. Krampert, P. Niklaus, and G. Gerber: *Adaptive shaping of femtosecond polarization profiles*. J. Opt. Soc. Am. B: Optical Physics, 20(5):878–881, 2003.

[36] J. Grosser, O. Hoffmann, C. Rakete, and F. Rebentrost: *Direct observation of the geometry of atom-atom and atom-molecule collisions*. J. Phys. Chem. A, 101:7627, 1997.

[37] B. H. Bransden and C. J. Joachain: *Physics of Atoms and Molecules*. Longmann Scientific & Technical, 1983.

[38] F. Schwabl: *Quantenmechanik*. Springer Verlag, Deutschland, 1990.

[39] R. Fink and V. Staemmler: *A multi-configuration reference CEPA method based on pair natural orbitals*. Theoret. Chim. Acta, 87(1-2):129–145, 1993.

[40] M. Jungen *private communication*.

[41] (ed.), A. D. Brandauk: *Molecules in Laser Fields*. Marcal Dekker, Inc., New York, 1994.

[42] C. Cohen-Tannoudji, J. Dupont Roc. and G. Grynberg: *Atom-Photon Interactions*. John Wiley & Sons, Inc, New York, 1992.

[43] N. Allard and J. Kielkopf: *Effect of collisions on atomic spectral lines*. Rev. Mod. Phys. A, 54:1103, 1982.

[44] E. E. Nikitin and Ya. Umanskii: *Theory of Slow Electronic Collisions*. Springer Verlag, Berlin, 1984.

[45] R. Schinke: *Photodissociation Dynamics*. Cambridge University Press, Cambridge, 1993.

[46] F. Rebentrost, S. Klose, and J. Grosser: *Quantum and semiclassical dynamics of differential optical collisions*. Eur. Phys, J. D, 1:277, 1998.

[47] M. S. Child: *Molecular Collision Theory*. Academic Press, New York, 1974.

[48] J. Grosser, O. Hoffmann, S. Klose, and F. Rebentrost: *Optical excitation of collision pairs in crossed beams: Determination of the NaKr $B^2\Sigma$ potential*. Europhys. Lett., 39:147, 1997. Das C-Potential ist von R. Düren, unveröffentlicht.

[49] C. Figl: *Optical collisions in crossed beams and Bose-Einstein condensation in a microtrap*. PhD thesis, Universität Hannover, Institut für Atom- und Molekülphysik, 2004.

[50] S. KLOSE: *Messung differentieller Wirkungsquerschnitte laserunterstützter Stoß-prozesse*. Doktorarbeit, Universität Hannover, Institut für Atom- und Molekülphysik, 1996.

[51] O. HOFFMANN: *Direkte Beobachtung von atomaren und molekularen Stoßpaa-ren*. Doktorarbeit, Universität Hannover, Institut für Atom- und Molekülphysik, 1999.

[52] Radiant Dyes Laser Accesories GmbH *homepage*. http://www.radiant-dyes.com.

[53] LAMBDA PHYSIK GMBH, Göttingen: *Dye Laser FL 3002, Instruction Manual*, 1986.

[54] LAMBDA PHYSIK GMBH, Göttingen: *Excimer Laser System EMG 201 MSC*.

[55] T. SCHMIDT: *Manipulation von Stoßprozessen mit elliptisch polarisiertem Licht*. Diplomarbeit, Universität Hannover, Institut für Atom- und Molekülphysik, Hannover, 2003.

[56] A. A. RADZIG and B. M. SMIRNOV: *Reference Data on Atoms, Molecules and Ions*. Springer, Berlin, 1985.

[57] S. BASHKIN and J. O. STONER JR.: *Atomic Energy Levels and Grotrian Dia-grams*. Noth-Holland Publishing Company, Amsterdam, 1975.

[58] A. MÄTZING: *Eine Methode zur Untersuchung von Stoßprozessen*. Doktorarbeit, Universität Hannover, Institut für Atom- und Molekülphysik, 1994.

[59] C. RAKETE: *Optische Anregung von Stoßpaaren in gekreuzten Teilchenstrahlen*. Diplomarbeit, Universität Hannover, Hannover, Oktober 1997.

[60] O. KNACKE, O. KUBASCHEWSKI, and H. HESSELMANN: *Thermochemical Properties of Inorganic Substances*. Springer Verlag, Berlin, 1991.

[61] A. N. NESMEYANOV: *Vapor Pressure of the Chemical Elements*. Elsevier Pub-lishing Company, New York, 1963.

[62] N. B. VARGAFTIK: *Handbook of physical properties of liquids and gases*. Springer Berlin, 2 edition, 1975.

[63] R. GOLDSTEIN: *Untersuchungvon Stoßprozessen mittels Laseranregung: Opti-sche Stöße mit molekularen Targets und optische Stöße mit Femtosekunden-laserpulsen*. Doktorarbeit, Universität Hannover, Institut für Atom- und Molekülphysik, 2004.

[64] H. PAULI: *Other low-energy beam sources*. In *Atomic and Molecular Beam Methods (ed. G. Scoles)*, chapter 2. Oxford University Press, 1988.

[65] O. HOFFMANN: *Realisierung und Analyse eines gepulsten Molekularstrahles aus einer Kapillare*. Diplomarbeit, Universität Hannover, Hannover, April 1995.

[66] M. WUTZ, H. ADAM und W. WALCHER: *Theorie und Praxis der Vakuumtechnik*. Vieweg, Braunschweig, 3 Auflage, 1986.

[67] D. R. OLANDER, R. H. JONES, and W. J. SIEKHAUS: *Molecular beam sources fabricated from multichannel arrays. IV. speed distribution in the centerline beam*. J. of Applied Phys., 41(11):4388–4391, 1970.

[68] D. HOHMEIER: *Untersuchung der photoneninduzierten Stoanregung in gekreuzten Atomstrahlen mit differentiellen Nachweis*. Diplomarbeit, Universität Hannover, Hannover, 1995.

[69] O. WEHRHAHN: *Untersuchung optischer Stöße in gekreuzten Atomstrahlen*. Diplomarbeit, Universität Hannover, Hannover, 1995.

[70] D. R. MILLER: *Free jet sources*. In *Atomic and Molecular Beam Methods (ed. G. Scoles)*, chapter 2. Oxford University Press, 1988.

[71] H. C. W. BEIJERINCK and N. F. VERSTER: *Absolute intensities and perpendicular temperatures of supersonic beams of polyatomic gases*. Physica B+C, 111(2-3):327–352, 1981.

[72] M.J. VERHEIJEN, H.C.W. BEIJERINCK, W.A. RENES, and N.F. VERSTER: *A quantitative description of skimmer interaction in supersonic secondary beams: Calibration of absolute intensities*. Chem. Phys., 85(1):63–71, 1984.

[73] H. C. W. BEIJERINCK, R. J. F. VAN GERWEN, E. R. T. KERSTEL, J. F. M. MARTENS, E. J. W. VAN VLIEMBERGEN, M. R. TH. SMITS, and G. H. KAASHOEK: *Campargue-type supersonic beam sources: Absolute intensities, skimmer transmission and scaling laws for mono-atomic gases He, Ne and Ar*. Chem. Phys., 96(1):153–173, 1985.

[74] U. VOLZ and H. SCHMORANZER: *Precision lifetime measurements on alkali atoms and on helium by beam-gas-laser spectroscopy*. Physica Scripta, T65:48–56, 1996.

[75] D. A. GUNDELFINGER: *Entwicklung von Detektoren für den differentiellen Nachweis von optischen Stößen und für die Bestimmung absoluter Atomstrahl dichten*. Diplomarbeit, Universität Hannover, 1993.

[76] DR. SJUTS OPTOTECHNIK GMBH, Katlenburg Lindau: *Elektronenvervielfacher-Kanäle Serie KBL*.

[77] FAST COMTEC COMMUNICATION TECHNOLOGY GMBH, Oberhaching: *MCD-2 Dual Input Multiscaler/Multichannel Analyzer, User Manual*, 1996.

[78] NATIONAL ENGINEERING LABORATORY EG&G IDAHO INC., Idaho Falls: *Simion, Electrostatic Lens Analysis And Design Program*, 1988.

[79] NATIONAL INSTRUMENTS, Austin, Texas: *LabVIEW User Manual*, 2000.

[80] IOTECH, INC., Cleveland: *DaqBoard/2000 16-Bit: Programmer's Manual, Producing Custom Software for Data Acquistitation Systems, p/n 1008-0901 Rev. 2.0*.

[81] R. GOLDSTEIN, C. FIGL, J. GROSSER, O. HOFFMANN, and F. REBENTROST: *Nonadiabatic transitions in the exit channel of atom-molecule collisions: fine structure branching in Na + N_2*. J. Chem. Phys., 121(22):11068, 2004.

[82] J. H. GOBLE and J. S. WINNA: *Analytic potential functions for weakly bound molecules: The X and A states of NaAr and the A state of NaNe*. J. Chem. Phys., 70(5):2051–2057, 1979.

[83] J. GROSSER, O. HOFFMANN, and F. REBENTROST: *Collision photography: Imaging of ultrafast atomic processes*. Europhys. Lett., 58:209, 2002.

Thank you

I would like to thank Achim Großer for the chance to do my research in his group and for his great patience in the completion time of my thesis .

I am indebted to all other current and former members of my working group like Cristina Figl, Ralf Goldstein, Thomas Schmidt, Dirk Wößner, Peter Wilhelms and especially Olaf Hoffmann for a lot of fertile discussions about physics, the help to run the experiments and the great time we spent together.

I thank the members of our workshop: Stefan Bertram, Jochen Claus, Hartmut Lehmann, Philipp Schauzu and in particular Manfred Marquardt for fast and competent execution of all the small and big requests which were necessary to run and improve the experiment.

Thanks to Helmut Glanz and Jochen Paul for the assistance in all questions related to electronics and computers and Sabine Rehmert for doing all the administrative work.

I thank Frank Rebentrost for the great co-operation and all the help related to the quantum mechanical calculations, also Martin Jungen for the calculation of the LiH_2 potential surfaces.

I would like to thank Alain Aspect, Chris Westbrock, Philippe Bouyer, Denis Boiron and all members of the group in Paris who gave me the opportunity to join their group and open the door to the interesting topic of Bose-Einstein condensation.

I thank Eberhardt Tiemann for organizing this great European Graduate College and all the members and staff of the Graduate College in Hannover, Paris and Glasgow, who gave me the wonderful alternative to get insights in a lot of interesting fields of physical research.

Thanks a lot to my beloved parents Christa and Dieter Grimpe for their selfless aid during the whole time of my thesis.

Last but not least I would like to really thank all my friends and members of my family, who shared the good and the hard times of my thesis with me, them who were there when I needed diversion, consolation, an observant listener, advice or just their presence. Love to you all!

Curriculum Vitae

Personal data:

Name:	André Grimpe
Date of birth:	27th of September 1968
Place of birth	Stolzenau
Family status	unmarried

School education:

Sept. 1975 - July 1981	elementary school
Aug. 1981 - June 1988	Hindenburgschule Nienburg; final examination: Abitur

Military services:

Oct. 1988 - Dec. 1989	Panzerpionierkompanie 320 Dörverden

University education:

Oct. 1989 - Aug. 1997	Diploma studies in physics at the University of Hannover; degree: Physik Diplom
since April 2000	Ph.D. student at the University of Hannover
since Jan. 2001	Colleague of the European Graduate College "Interference and Quantum Application"

Research positions and scholarships:

Jan. 2001 - Dec.2003   scholarship holder from the European
                                    Graduate College "Interference and
                                    Quantum Application"
Jan. 2004 - June 2004   Scientic assistant at the University
                                    of Hannover

Professional experience:

Dec. 1997 - May 1998   employee at Üstra Reisen Hannover
Nov. 1998 - Dec. 2000   self-employed: consumer promotion (IT)

List of Publications

1. T. Schmidt, C. Figl, A. Grimpe, J. Grosser, O. Hoffmann and F. Rebentrost:
   Control of Atomic Collisions by Laser Polarization
   Phys. Rev. Lett. **92** (2004) 033201-3

2. A. Grimpe, C. Figl, J. Grosser, O. Hoffmann, F. Rebentrost:
   Oscillatory differential cross sections for Li + He, Ne, H_2 and D_2 optical collisions
   J. Phys. B: At. Mol. Opt. Phys. **38** (2005) 135-140

3. A. Grimpe, J. Grosser, O. Hoffmann, F. Rebentrost:
   Laser excitation of NaNe collision pairs probing the A $^2\Pi$ potential
   J. Chem. Phys. **122** (2005) 071103 (1-3)

4. O. Hoffmann, A. Grimpe:
   Collision photography: Imaging of atom-atom collisions
   Khimicheskaya Fizika **23 (2)**, (2004) 29

5. C. Figl, A. Grimpe, R. Goldstein, J. Grosser, O. Hoffmann, F. Rebentrost, D. Wößner, M. Jungen, M. Lehner:
   Direct observation of atom-molecule collisions by optical excitation Russ. J. Phys. Chem., **Vol. 76, Suppl. 1**, 90 (2002)